Title

An Investigation of the Relationship Between Battery Aging and Fuel Economy for Heavy-Duty Alternative-Powertrain Vehicles

Author

Mallon, Kevin Ryan

Publication Date

2022

Peer reviewed|Thesis/dissertation

An Investigation of the Relationship Between Battery Aging and Fuel Economy for Heavy-Duty Alternative-Powertrain Vehicles

By

KEVIN RYAN MALLON

DISSERTATION

Submitted in partial satisfaction of the requirements for the degree of

DOCTOR OF PHILOSOPHY

in

Mechanical And Aerospace Engineering

in the

OFFICE OF GRADUATE STUDIES

of the

UNIVERSITY OF CALIFORNIA

DAVIS

Approved:

Francis Assadian, Chair

Shima Nazari

Xinfan Lin

Committee in Charge

2022

To Paula

I couldn't have done this without your love and support.

Contents

An Investigation of the Relationship Between Battery Aging and Fuel Economy for Heavy-Duty Alternative-Powertrain Vehicles

Abstract

Heavy-duty electric and hybrid electric vehicles are potential means to reduce the emissions of the transportation sector. However, the lithium batteries needed to power these vehicles can be cost and weight prohibitive, and battery degradation adds to the lifetime cost of these vehicles. Buses in particular are considered throughout this work—their frequent stopping and starting makes them prime candidates for electrification or hybridization, yet that same stopping and starting can be a source of significant battery wear. This work explores methods to improve battery lifespan and improve the overall economic feasibility of heavy-duty alternative powertrain vehicles.

Four studies are carried out to this effect; simulation is used in all cases due to the slow rate of battery degradation and the expense associated with destructive testing. First, an electric bus is fitted with an on-board photovoltaic system. A full model for on-board photovoltaics is developed and it is shown that the power provided by the modules reduce the battery discharge depth to a sufficient degree to improve battery lifespan. Bus rooftop photovoltaics are shown to have a positive return on investment.

Next, aging-aware control of a hybrid energy storage system is considered. Hybrid energy storage pairs an ultracapacitor with the conventional lithium battery to reduce large current spike and improve battery aging. A new energy management strategy that incorporates ultracapacitor aging is shown to be a more effective means of control than existing literature.

The third and fourth studies concern robust energy management. The third considers the robustness of aging-aware energy management to aging model variations and methods of improving the robustness of aging-aware strategies are proposed. The fourth study introduces a new energy management concept that incorporates elements of minimax dynamic programming. This new strategy is first shown to improve robustness of a series hybrid bus to driving condition uncertainty, then second it is shown to improve the performance of aging-aware control of an electric vehicle with hybrid energy storage.

Acknowledgments

I would like to express my gratitude to my advisor, Prof. Francis Assadian. This dissertation would not have been possible without his advice, encouragement, and mentorship. He has been supportive and caring at every stage of my Ph.D., and this dissertation wouldn't have been possible without his guidance and insight.

I have also been fortunate to have Prof. Xinfan Lin and Prof. Shima Nazari on my dissertation committee; their review and suggestions have been greatly appreciated. I would also like to thank Prof. Zhaodan Kong and Prof. Ronald Hess for serving on my Qualifying Examination committee.

I would also like to thank my family and friends for their support along the way. To my parents and siblings, thank you for your ever-present support. To Paula, thank you for being with me every step of the way. I love you so much, and couldn't have done this without you.

CHAPTER 1

Introduction

1.1. Background

The internal combustion engine is a major contributor to greenhouse gas emissions and hydrocarbon pollution across the globe. Motor vehicles account for a major portion of pollutants such as carbon monoxide, nitrogen oxide, and volatile organic compounds [**1**]. Furthermore, heavy-duty (HD) motor vehicles such as trucks and buses are responsible for 25% of all U.S. transportation-related greenhouse gas emissions [**2**]. Alternative powertrain vehicles (APVs), such as electric vehicles (EVs) and hybrid-electric vehicles (HEVs), are potential technological solutions to reduce transportation-sector emissions and fuel consumption. However, heavy-duty APVs (HD-APVs) require large amounts of battery stored energy, which can be cost and weight prohibitive [**3**]. Degradation of the battery further adds to the lifetime cost of an APV, and battery degradation rate has been shown to be inversely correlated with fuel economy (albeit in non-HD vehicles) [**4**, **5**]. Technologies that improve battery lifespan and fuel economy will reduce this lifetime cost and hasten the adoption of sustainable transportation.

1.2. Project Scope

The aim of this dissertation is to analyze the relationship between fuel economy and battery aging in HD-APVs and to investigate ways to the reduce trade-off between the two. Buses in particular are considered throughout this work—their frequent stopping and starting makes them prime candidates for electrification or hybridization, yet that same stopping and starting can be a source of significant battery wear. This research applies a systems-level approach: It focuses on how the powertrain subsystems interact and what new subsystems can be added to the powertrain to increase efficiency while decreasing the battery degradation.

This research can be broken into two subject areas: powertrain control systems with aging dynamics, and integration of new components to the powertrain to reduce battery aging. New powertrain components includes ultracapacitor (UC) energy storage and on-board photovoltaic

(OBPV) systems. The contribution of this dissertation is a refined understanding of the relationship between battery degradation and fuel economy in HD-APVs.

This approach to the battery aging and fuel economy trade-off can be illustrated with the following example: Consider some hypothetical hybrid or electric vehicle. For this vehicle, there must be some trade-off between fuel consumption battery degradation. The first step of analyzing the vehicle is to find the Pareto frontier of this trade-off—what is the best battery lifespan that can be achieved for a given rate of fuel consumption, and vice versa? This frontier is illustrated in Figure 1.1(a), and can be found using methods of global optimal control. Next, individual controllers of varying designs can be evaluated to assess what types of controllers best approach the Pareto frontier. Figure 1.1(b) shows the fuel/aging trade-off of some potential controller designs. Then, new components can be considered for the vehicle powertrain. As shown in Figure 1.1(c), the next topic of study is how control of these new components shifts the optimal frontier. Finally, Figure 1.1(d) shows the final step, studying how control of the new components can improve fuel/aging trade-off for the different types of causal controllers.

1.3. Dissertation Structure

This chapter, Chapter 1, consists of the project background, a review the relevant literature, and an outline of the research objectives. Chapters 2 and 3 review common aspects of modeling and control used by the studies presented later in this work. Chapter 2 describes the modeling techniques, including the vehicle modeling, energy storage modeling, and aging mechanism modeling, while Chapter 3 describes the dynamic programming control method. Chapter 4 investigates on-board photovolataics and its impact on battery lifespan. Chapter 5 moves to control of hybrid energy storage systems, and demonstrates the advantage of including ultracapacitor aging mechanisms in aging-aware control. Chapter 6 studies the robustness of aging-aware energy management to variations in aging behavior. Chapter 7 investigates a new method of robust control and applies it to aging-aware energy management. Finally, Chapter 8 concludes the work.

1.4. State-of-the-Art

This section first provides some necessary background on alternative powertrains and on battery health modeling. It then discusses related work and current gaps in the literature regarding

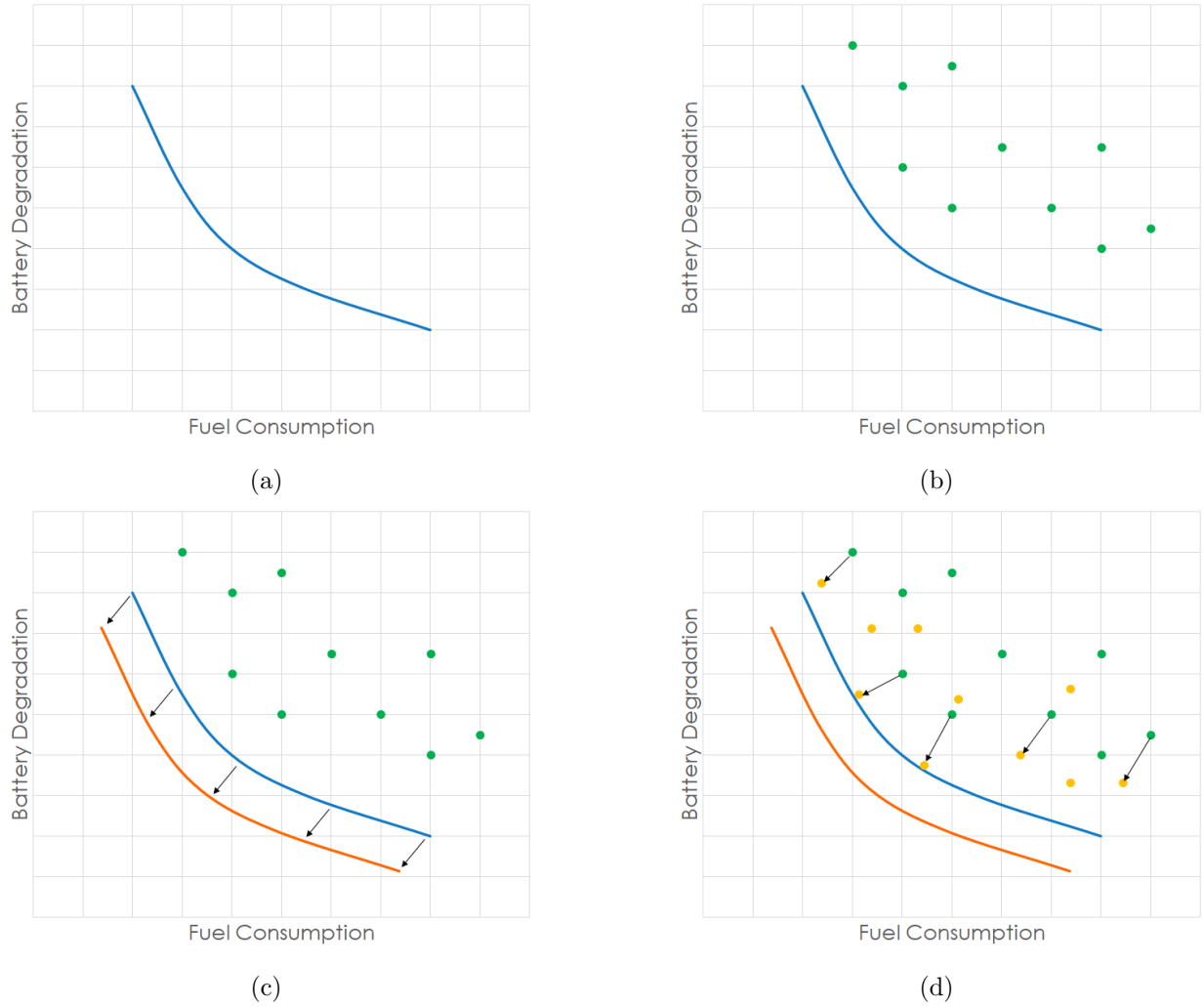

FIGURE 1.1. (a) Find the (noncausal) optimal frontier for battery aging/fuel economy trade-off. (b) Find which (causal) controllers best approach the optimal frontier. (c) Show how new components can shift the optimal frontier. (d) Show how new components can improve the performance for realizable controllers.

aging-aware powertrain control systems, OBPV, and UC energy storage. Additional review of the literature as it relates to the particular studies in this work is given in those relevant chapters.

1.4.1. Powertrain Topologies. Alternative-powertrain vehicles come in four main varieties: the EV, the series HEV, the parallel HEV, and the series-parallel HEV [**6**]. The EV is the simplest of these powertrain topologies and consists of an electric traction motor (or motors) which draws energy from on-board batteries as shown in Figure 1.2(a). In a series HEV (SHEV), the tractive force is provided by the electric motor the same way as in an EV. However, a combustion engine and generator are combined to supply additional electric power to the traction motor and battery.

There is no mechanical connection between the engine and the ground. This configuration is shown in Figure 1.2(b). The parallel HEV, on the other hand, uses the engine for traction so that the engine and motor simultaneously propel the vehicle, as shown in Figure 1.2(c). The series-parallel configuration combines the series and parallel configurations with a planetary gear set, so that the engine can provide traction as well as power a generator, as shown in Figure 1.2(d).

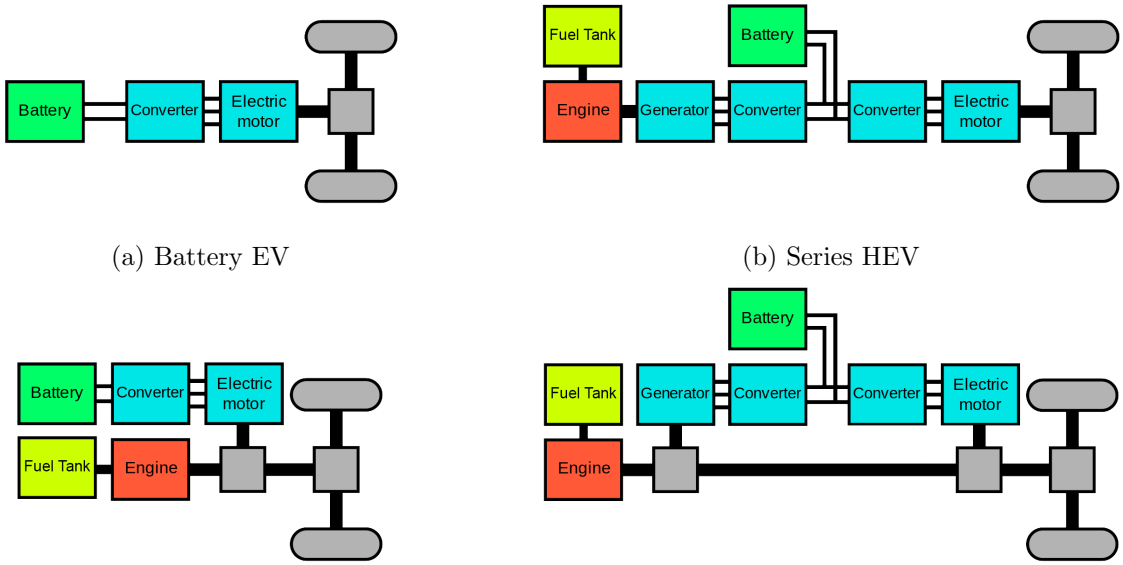

(a) Battery EV

(b) Series HEV

(c) Parallel HEV

(d) Series-Parallel HEV

FIGURE 1.2. Powertrain configurations.

An additional classification for HEVs is whether they are "plug-in" hybrids. Compared to ordinary HEVs, the plug-in hybrid has a larger battery pack and can be charged from the grid, so that it can drive long distances with battery power only. Plug-in hybrids generally operate in two modes: charge depleting mode, where the vehicle behaves like an EV, and charge-sustaining mode, where the vehicle operates like an ordinary HEV and maintains the battery charge.

This dissertation limits its scope to only the powertrain topologies most common for HD-APV vehicles: EVs, SHEVs, and series plug-in HEVs (SPHEV) [**7**, **8**].

1.4.2. Battery Aging. Aging of batteries is primarily caused by the formation of the Solid Electrolyte Interface (SEI) layer—substrates in the chemical reaction pathways—and the formation of cracks in the electrode materials from repeated stress cycles [**9**]. These aging mechanisms are accelerated by high charge and discharge rates, extreme battery temperatures, and deep depths of discharge [**10**]. Aging of the battery causes capacity fade (a decrease in the charge storage capacity)

and power fade (a decrease in the battery efficiency). However, models of the cell chemistry that include the thermal and stress/strain relationships used to describe SEI layer growth and aging are computationally intensive and are ill-suited for the type of control-system analysis considered in this research [**9**, **11**, **12**, **13**, **14**].

Research of battery aging in APVs instead tends to utilize empirical models [**5**, **15**, **16**, **17**, **18**, **19**, **20**]. Using empirical aging models for vehicle battery degradation analysis provides a good trade-off between precision and complexity. These empirical models do not consider the physical or chemical processes of the battery degradation but instead approximate the battery's health by fitting experimental data to aging factors like charge throughput, calendar life, and number of charge/discharge cycles.

For instance, references [**15**, **16**, **21**, **22**] develop aging models that relates charge throughput to degradation, with temperature and current magnitude as additional stress factors. References [**23**] and [**24**] include depth of discharge as an additional stress factor, while [**24**] also distinguishes the impact of charging and discharging currents on battery degradation. References [**25**] and [**26**] expand the model presented in [**21**] to include the effect of SOC on battery degradation during storage conditions. The aging models for hybrid vehicle applications in [**19**] and [**20**] consider number of charge/discharge cycles and calendar life and use temperature, depth of discharge, and average state of charge as aging stress factors. Other models in the literature such as [**11**, **27**, **28**] use simple cycle counting to measure the state-of-health.

This dissertation uses existing empirical models of battery degradation, presented in further depth in Section 2.3.1. It also focuses only on lithium ion batteries, given their prevalence in both production vehicles and published aging models.

1.4.3. Energy Management Systems. One of the main issues in the development of APVs is how to control the flow of power from the engine, battery, or other energy storage components to meet the driver's power demand. The energy management system (EMS) provides the supervisory control that governs how the driver's power demand is met and seeks to provide the requested power in the most efficient manner possible. Classical (linear, time-invariant) control systems do not handle system constraints well, so in the field of vehicle EMS it is more common to use non-classical control methods ranging from rule-based heuristics to fuzzy-logic-based control to

non-classical optimal control approaches [**29**, **30**, **31**]. This research focuses on robust and optimal controllers.

This research primarily focuses on dynamic programming (DP) approaches to optimal control, namely deterministic dynamic programming (DDP) and stochastic dynamic programming (SDP). DDP is used for assessing the optimal performance over given operating conditions [**29**]. DDP uses precise knowledge of future driver behavior and for that reason can be used to find the true optimal control over a specific trajectory [**32**]. For that same reason it is also non-causal and non-implementable as an EMS. However, it is generally useful to compare a realizable EMS to the DDP optimal solution to assess how well that control system compares to the true optimal performance [**33**]. SDP is likewise an optimal approach and determines the control policy by minimizing the *expected* future costs of a cost function over the range of possible future power requests [**34**, **35**]. Considering expected future costs rather than exactly known future costs makes the SDP approach causal and implementable compared to DDP. Minimax dynamic programming (MDP) is also considered as a robust approach to energy management. MDP determines the control policy that minimizes a cost function for worst-case future power requests [**32**, **36**]. In some literature this approach is referred to as robust model predictive control. In that context, MDP minimizes the cost of a worst-case future trajectory, in contrast to stochastic model predictive control that optimizes against an expected trajectory [**37**, **38**].

The equivalent consumption minimization strategy (ECMS) is another optimal control strategy that minimizes variables such as fuel consumption, emissions, or stored energy usage over a certain route, and is also used for to benchmark the performance of energy management strategies [**39**]. This research follows the method developed in [**40**] using an equivalence factor tuned for a given drive cycle, although other implementations of ECMS, such as ECMS utilizing Pontryagin's Minimization Principle to obtain a global optimum [**6**] or the adaptive ECMS discussed in [**41**], are not considered. Additionally, the general concept of ECMS—jointly minimizing different types of consumption, such as energy and battery life—is used in EMS design.

This research integrates battery aging dynamics into these EMSs to form controllers that regulate battery degradation. The existing literature on EMSs that actively regulate battery aging is limited. In Reference [**4**], the authors developed an SDP-based EMS for a parallel-HEV passenger vehicle that accounted for battery wear by mapping operating conditions to substrate growth, and

associating substrate growth with battery state-of-health. Their control system was implemented using look-up tables. The authors also analyzed how reducing battery aging increased the fuel consumption. However, this research does not appear to properly handle the effect of large charge and discharge currents on aging: although it modeled the aging rate as increasing with large charging currents, large discharging currents were incorrectly modeled as decreasing the aging rate (in conflict with experimental results in, for instance, references [**24**] and [**42**]). In References [**5**] and [**43**], the authors developed a deterministic EMS for a parallel-HEV passenger vehicle that regulates battery degradation using a "severity factor" map: the control policy penalizes battery usage by an amount related to the severity of the operating conditions (in terms of temperature and current magnitude). The authors of [**5**] also showed an inverse correlation between the battery aging and fuel consumption. However, the proposed EMS was non-causal and therefore unimplementable.

Based on a review of the literature, the following gaps in knowledge exist:

- What control strategies best reduce the battery aging/fuel economy trade-off?
- What is the cost/benefit of the reduced aging?
- How does robustification of the EMS affect the battery aging/fuel economy trade-off?

1.4.4. On-Board Photovoltaics. A possible method to reduce battery wear and decrease vehicle fuel consumption is to supplement the energy storage system with photovoltaic (PV) modules, as shown in Figure 1.3, so that additional power can be generated while the vehicle is on the road. The power generated from OBPV would reduce the charge-throughput of the battery and may limit aging stress factors such as depth of discharge and current magnitude. Flexible PV panels allow for vehicle integration without aerodynamic losses or major infrastructural costs [**44**]. Contemporary research for OBPV can generally be broken into two groups: Integrated PV for consumer vehicles and integrated PV for commercial vehicles.

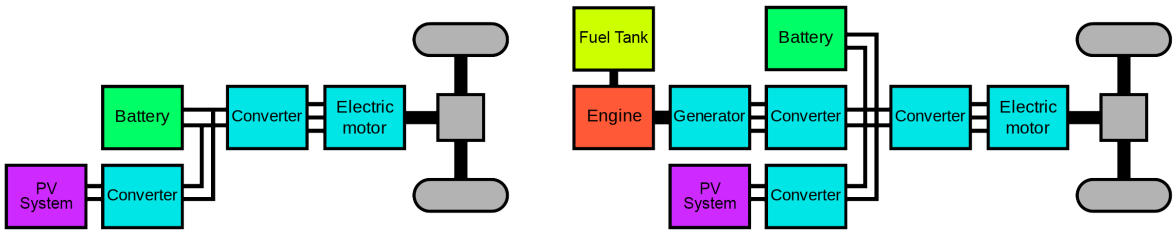

(a) (b)

FIGURE 1.3. Integrared PV for **(a)** an EV; **(b)** an SHEV.

As consumer vehicles are often parked throughout the day, much of the literature regarding consumer vehicles, such as references [**45**, **46**, **47**], focuses on analyzing and maximizing collected solar energy for parked vehicles. Other literature more generally considers the impact of OBPV on fuel consumption and vehicle emissions in an attempt to determine when PV modules would be efficient and inexpensive enough for widespread on-board use [**48**, **49**]. However, the results found from literature regarding passenger vehicles cannot be extrapolated to HD vehicles.

Commercial vehicles are generally operated constantly throughout the day so analysis of OBPV on commerical vehicles tends to focus on powering vehicle components and on the long-term benefits of OBPV. For instance, PV modules have been integrated into health emergency vehicles in order to power medical equipment while the engine is not running and to help guarantee a charge when the vehicle must be started [**50**]. In another application, OBPV was shown to provide enough energy to power the refrigeration unit on a delivery vehicle [**51**]. Meanwhile, [**44**] examines the energy collected from roof-mounted PV modules on a diesel-powered bus operating in Poland, noting that such a system "does not require extensive modification to the vehicle electrical system." Experimental results indicated that the solar energy, used to power auxiliary electrical loads, would quickly provide a positive return on investment. Reference [**52**] evaluates the economic feasibility and environmental impact of OBPV for diesel-powered trucks and buses, showing that OBPV could substantially reduce the carbon footprint of HD vehicles with a payback time of only two to four years.

However, the listed literature only considers combustion-engine vehicles. There is generally a lack of research regarding the impact of OBPV for non-conventional HD vehicles. Additionally, there does not appear to be any research (besides the author's own) that considers the relationship between OBPV and battery degradation. This presents the following gaps in knowledge:

- How does OBPV affect the aging of the battery?
- How does OBPV affect the fuel economy of HD-APVs?
- What is the cost/benefit of OBPV on HD-APVs?

1.4.5. Hybrid Energy Storage Systems. Lithium batteries have a high energy density but low power density, meaning that although they store large amounts of energy, that energy cannot be accessed quickly. Additionally, high currents to and from the battery are a stress factor for battery degradation. A potential solution to these problems is to integrate UCs into the energy

storage system, as shown in Figure 1.4. UCs store energy in the electric field of an electrochemical double layer and have a high power density but low energy, allowing them to serve as complements to battery energy storage [**6**]. By integrating UCs into the powertrain, it becomes possible to meet the vehicle power requirements with a smaller battery and reduces battery degradation by restricting large currents going to or from the battery [**6**,**33**]. Aging of UCs is primarily dependent on time, temperature, cell voltage, and current magnitude [**53**, **54**, **55**]. The converter shown in Figure 1.4 allows power going to or from the UC to be actively controlled, which in turn allows for better utilization of the UC [**56**, **57**].

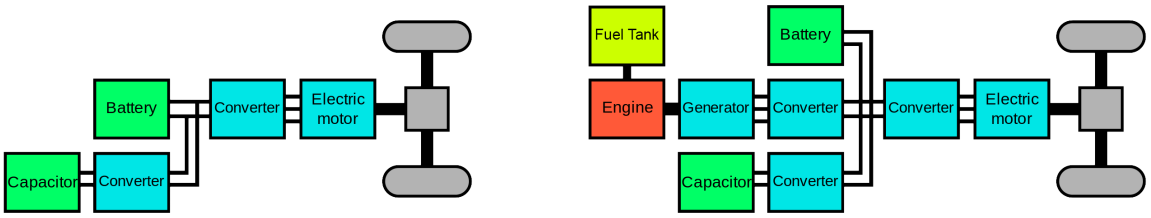

(a) (b)

FIGURE 1.4. Integrated UC for **(a)** an EV; **(b)** an SHEV.

Some related work includes reference [**58**], in which the authors develop an optimal control policy to govern UC behavior and demonstrate clear aging improvements over a passive (uncontrolled) system. References [**59**] and [**60**] carried out a parametric study on battery degradation versus UC size in EVs, using a rule-based control system to govern power allocation. Reference [**61**] developed a control strategy integrating UCs with lead-acid batteries in a HEV for battery life extension, and found that a 50% increase in battery cycle life would be needed for the UC to be cost-effective. Reference [**62**] experimentally demonstrated a decrease in battery power fade and temperature rise in lithium-ion batteries due to UCs on an EV load profile.

The state-of-the art is to directly incorporate a battery aging model into the vehicle's energy management strategy, so that battery aging can be controlled directly, rather than indirectly by limiting aging factors like large currents and temperatures. [**63**], for instance, uses Dynamic Programming to develop an aging-aware optimal controller that jointly minimizes the equivalent cost of battery degradation and electrical energy losses in an electric bus. [**64**] demonstrates an application of Q-learning to both identify and control battery aging behavior in an electric car's HESS. references [**65**, **66**, **67**] demonstrate an optimal control strategy to directly minimize battery aging

in a HESS for a plug-in HEV using an Equivalent Consumption Minimization Strategy (ECMS), where battery aging is modeled using a throughput-based aging model. On the other hand, [**68**] incorporates a cycle-counting based aging model to optimally size the HESS for a plug-in HEV, finding the HESS should be sized so that UCs supply approximately 80% of power in order to maximize the economic benefit of the HESS.

This research is interested in optimal control of the UC to reduce battery aging and maximize overall value of the energy storage system, in particular the effects of ultracapacitor aging. Although the impacts on aging are well researched and some work does exist on optimal aging-aware control, the following gaps in knowledge still exist:

- How are battery aging, ultracapacitor aging, and fuel economy jointly impacted by aging-aware control?
- What control strategies best minimize the trade-off between fuel economy and aging in a system with integrated UCs?
- What is the cost/benefit of integrating UCs into the powertrain?

CHAPTER 2

Vehicle and Component Modeling Methodologies

This chapter develops a complete model for an electric and series hybrid electric bus, optionally with a hybrid energy storage system. The vehicle dynamics are presented first, followed by powertrain components, then lithium ion battery and ultracapacitor dynamics, and finally discusses aging modeling for both lithium ion batteries and ultracapacitors. This chapter covers modeling shared across multiple aspects of this research. Modeling unique to a particular study—such as on-board photovoltaics modeling or ultracapacitor aging—are reserved for the relevant chapter.

2.1. Vehicle Modeling

2.1.1. Vehicle Dynamics. The goal of the vehicle dynamics model is to capture the primary forces on the vehicle while maintaining model simplicity. To that end, a backwards-facing quasi-static vehicle model is used to simulate the vehicle dynamics [**69**]. A backwards-facing model assumes that the driver accurately follows a specified velocity profile, allowing the acceleration to be approximated from the known velocity profile and eliminating the need for a driver model. This in turn allows the time-history of the electrical load placed on the powertrain to be calculated in advance.

This vehicle model, illustrated in Figure 2.1, considers inertial forces, aerodynamic drag, and rolling resistance. A flat road profile is assumed in this research, so gravitational forces are excluded.

The drag force is given by

$$F_{drag} = \frac{1}{2}\rho A_f C_D (v_v)^2 \tag{2.1}$$

where ρ is the air density, A_f is the frontal area, C_D is the drag coefficient, and v_v is the vehicle velocity. Rolling resistance is given by

$$F_{roll} = M_v g C_R \tag{2.2}$$

where M_v is the vehicle's total mass, g is acceleration due to gravity, an C_R is the rolling resistance coefficient. In a backwards-facing model, the inertial force is determined from the vehicle

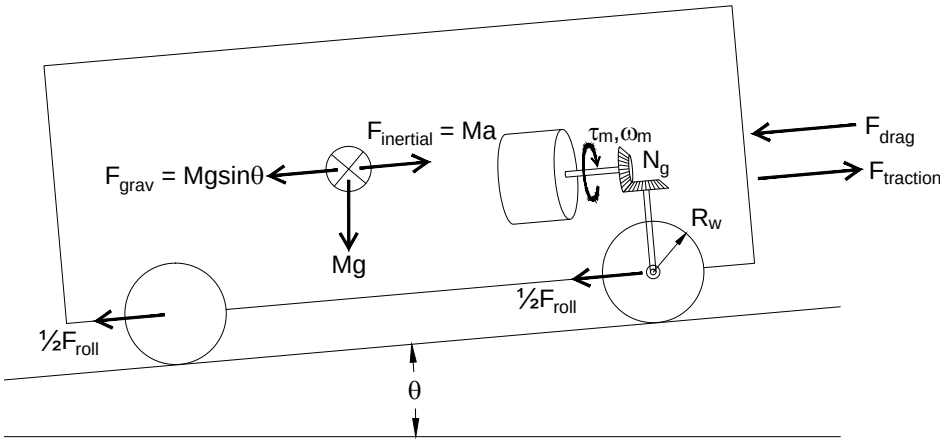

FIGURE 2.1. Bus vehicle model. θ is assumed to be 0.

acceleration and the vehicle mass as

$$F_{inertial} = M_{eq}\frac{dv_v}{dt}. \tag{2.3}$$

M_{eq} is the mass of the bus plus the equivalent mass due to the rotational inertia of the motor and wheels

$$M_{eq} = M_v + 4J_w\left(\frac{1}{R_w}\right)^2 + J_m\left(\frac{N_{fd}N_{gb}}{R_w}\right)^2, \tag{2.4}$$

where J_w is the rotational inertia of one wheel, J_m is the rotational inertia of the motor, R_w is the wheel radius, N_{fd} is the final drive ratio, and N_{gb} is the gearbox ratio. These terms are related to the powertrain model discussed in Subsection 2.1.2 and are dependent on the vehicle configuration. The acceleration term in (2.3) is approximated from a given velocity profile according to

$$\frac{dv_v}{dt}(t) \approx \frac{v_v(t+\Delta t) - v_v(t-\Delta t)}{2\Delta t}. \tag{2.5}$$

The inertial, drag, and rolling resistance forces sum together to give the traction force on the bus.

$$F_{traction} = F_{inertial} + F_{drag} + F_{roll} \tag{2.6}$$

The vehicle's wheel speed is defined as

$$\omega_{wh} = v_v/R_w. \tag{2.7}$$

Parameter values for the vehicle model can be found in Table 2.1. The bus is assumed to be fully loaded and at its maximum allowable weight. Vehicle parameters are estimated from existing literature on bus simulation [**70**, **71**, **72**].

TABLE 2.1. Vehicle model physical parameters.

Parameter	**Variable**	**Value**
Vehicle Mass	M_v	18,181 kg
Frontal Area	A_f	8.02 m^2
Drag Coefficient	C_D	0.55
Roll Resistance Coefficient	C_R	0.008
Wheel Inertia	J_w	20.52 kg-m^2
Motor Inertia	J_m	0.277 kg-m^2
Wheel Radius	R_w	0.48 m
Final Drive Ratio	N_{fd}	5.1
Gearbox Ratio	N_{gb}	5
Transmission Efficiency	η_{trans}	96%

2.1.2. Powertrain Model. This section describes the modeling of the vehicle powertrain, including the transmission and electric motor, illustrated in Figure 2.2. The model for a SHEV with UC is given and can be simplified to other topologies, such as an SHEV without UC or an EV with hybrid energy storage. The battery and ultracapacitor dynamic models are left to Section 2.2.

2.1.2.1. *Transmission.* The vehicle speed and traction force are transformed into motor torque and motor speed. Assuming a constant transmission efficiency of η_{trans}, represented as torque losses, the motor torque is given by

$$\tau_m = \begin{cases} \left(\frac{R_w}{N_{fd}N_{gb}}F_{traction}\right)/\eta_{trans}, & F_{traction} \geq 0 \\ \left(\frac{R_w}{N_{fd}N_{gb}}F_{traction}\right)\cdot\eta_{trans}, & F_{traction} < 0 \end{cases} \tag{2.8}$$

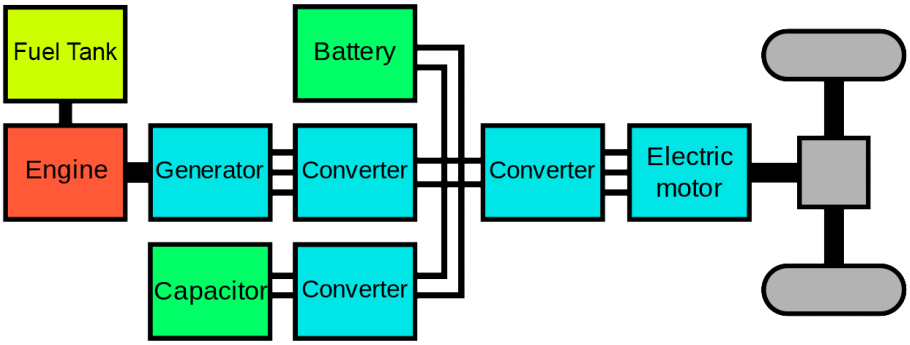

FIGURE 2.2. Series HEV powertrain model with UC.

and the motor speed is given by

$$\omega_m = \frac{N_{fd} N_{gb}}{R_w} v_v \tag{2.9}$$

Note that the vehicle uses a fixed gear ratio, that is, N_{gb} is constant. Then, the mechanical power needed to drive the vehicle P_{mech} can be expressed in terms of the motor torque and angular velocity.

$$P_{mech} = \tau_m \cdot \omega_m \tag{2.10}$$

Here, positive P_{mech} indicates acceleration. Parameter values for transmission can be found in Table 2.1.

2.1.2.2. *Motor and Power Electronics.* The electrical power demand of the motor, P_{dem}, is calculated from P_{mech} and an efficiency parameter η_{motor}, $0 < \eta_{motor} < 1$. η_{motor} is variable as a function of τ_m and ω_m and is determined from a static efficiency map.

$$P_{dem} = \begin{cases} P_{mech}/\eta_{motor} & \tau_m \geq 0 \\ P_{mech} \cdot \eta_{motor} & \tau_m < 0 \end{cases} \tag{2.11}$$

The efficiency map is obtained from the National Renewable Energy Laboratory's Advanced Vehicle Simulator (ADVISOR) data library [**73**], and scaled to the appropriate size using the scaling method in [**6**]. It includes both the motor efficiency and the efficiency of the power electronics. The modeled vehicle utilizes a 250kW AC induction motor.

Depending on the powertrain topology, the power demand for the electric motor may be provided by battery power P_{batt}, generator power P_{gen} (if the vehicle is a series-hybrid), or ultracapacitor power P_{uc} (if the vehicle has hybrid energy storage). As part of the quasi-static simulation, it

is assumed that the power demand is always met.

$$P_{dem} = P_{batt} + P_{gen} + P_{uc} \tag{2.12}$$

P_{dem} is set by the drive cycle and P_{gen} and P_{uc} are treated as a controlled variable. Therefore, P_{batt} is fixed and dependent on P_{dem}, P_{gen}, and P_{uc}. Therefore, (2.12) can be rewritten as

$$P_{batt} = P_{dem} - P_{gen} - P_{uc} \tag{2.13}$$

If the vehicle in question is a battery electric vehicle (BEV) without hybrid energy storage, then Equation (2.13) reduces to

$$P_{batt} = P_{dem} \tag{2.14}$$

If the BEV *does* have hybrid energy storage, then Equation (2.13) reduces to

$$P_{batt} = P_{dem} - P_{uc} \tag{2.15}$$

Finally, if the vehicle in question is a series hybrid without hybrid energy storage, then Equation (2.13) reduces to

$$P_{batt} = P_{dem} - P_{gen} \tag{2.16}$$

2.1.2.3. *Engine-Generator Model.* The parts of this work considering a SHEV use a 200kW generator and 180kW diesel engine, sized based on [**74**] with a 6:1 fixed gear ratio between them, as depicted in Figure 2.3. Given this engine size, the full generator power cannot be utilized. However, this engine size ensures the optimal operating regions of the engine and generator overlap to ensure efficient operation of the combined system. Efficiency maps for both the heavy-duty diesel engine and generator are obtained from ADVISOR's data library [**73**], and scaled to the appropriate size using the scaling method in [**6**]. The generator map includes the efficiency of the converter.

Because of the curse of dimensionality, it is desirable to use as few state variables and control variables as possible in the formulation of the engine and generator model. Following the work shown in [**37**] for a series hybrid vehicle, static maps for engine and generator efficiency are used to simplify the modeling. Additionally, the model only considers the power into and out of each element, rather than track the torques and speeds. The model simplification is shown in Figure 2.3.

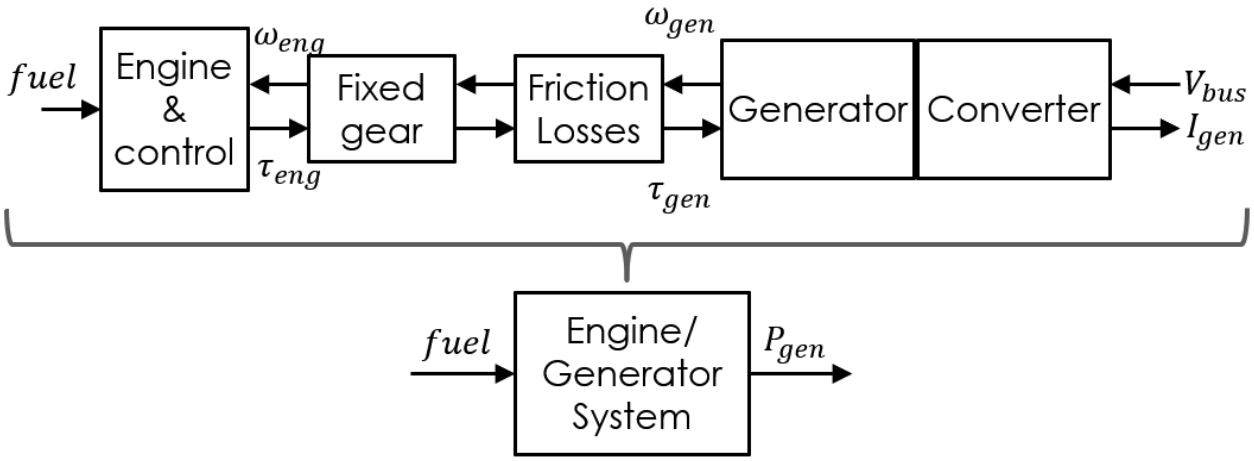

FIGURE 2.3. Engine/Generataor block diagram and simplification.

First, the generated electrical power P_{gen} is considered to be related to the mechanical power by an efficiency factor η_{gen}.

$$P_{gen} = \eta_{gen} \cdot P_{gen,mech} \tag{2.17}$$

As shown in Figure 2.3, the generator is powered by a combustion engine subject to friction and gearbox losses represented by η_{gb}. Then,

$$P_{gen} = \eta_{gen} \cdot \eta_{gb} \cdot P_{eng} \tag{2.18}$$

The combustion takes place with an efficiency of η_{eng}. Therefore,

$$P_{gen} = \eta_{gen} \cdot \eta_{gb} \cdot \eta_{eng} \cdot P_{fuel} \tag{2.19}$$

where P_{fuel} is the amount of power stored in fuel, which is in turn equal to the mass flow rate of fuel times the energy density of the fuel.

Like η_{motor} in (2.11), η_{gen} and η_{eng} are dependent on the operating torque and speed of the generator and engine, respectively (η_{gb} is assumed to be a constant 99%). To keep the model simple and to avoid the need to track the torque and speed of the engine and generator, the converter and engine controller indicated in Figure 2.3 are assumed to control the generator and engine so as to follow an optimal efficiency curve (OEC) [**75**]. In other words, it is assumed that for a given output electrical power P_{gen}, the engine and generator operate at the torque and speed with the highest efficiency from fuel to electrical power. The OEC is found through a direct search of all points on the efficiency maps for the engine and generator. The OEC for this model is shown in Figures 2.4

and 2.5. Notably, the peak efficiency occurs at

$$P^*_{gen} = 85kW. \tag{2.20}$$

Finally, below a certain threshold power P_{sd}, the engine-generator system is considered off; no power is produced and no fuel is consumed. Instead, generator power $0 > P_{gen} > P_{sd}$ corresponds to when the engine is starting up and being brought to a minimum allowable speed by the generator, or when the engine is shutting down after use. The $0 > P_{gen} > P_{sd}$ region is denoted as the "startup region" in Figures 2.4 and 2.5.

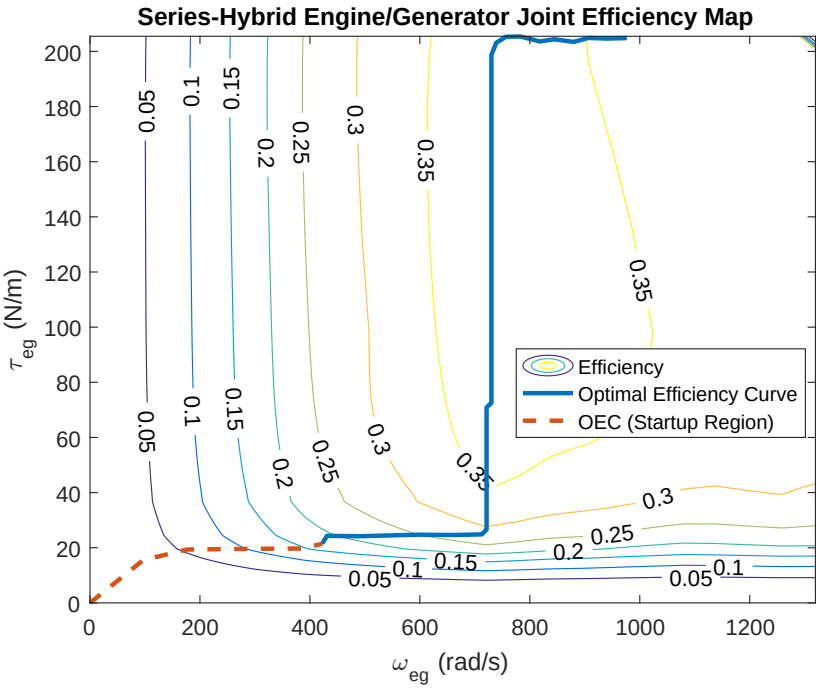

FIGURE 2.4. Efficiency map and optimal efficiency curve. The red line indicates the region where the generator is starting the engine.

2.2. Energy Storage System Dynamics

2.2.1. Battery. The vehicle's lithium-ion battery cells for simulation are modeled with the 2nd-order equivalent circuit shown in Figure 2.6, where V_{ocv} is the battery cell open-circuit voltage, R_s is the series resistance, and R_{pi} and C_{pi} are the parallel resistances and capacitances, respectively. All five of these parameters are variable with the battery's state of charge SOC_b and temperature, per the model provided in [**76**], although temperature dynamics are not considered in this work.

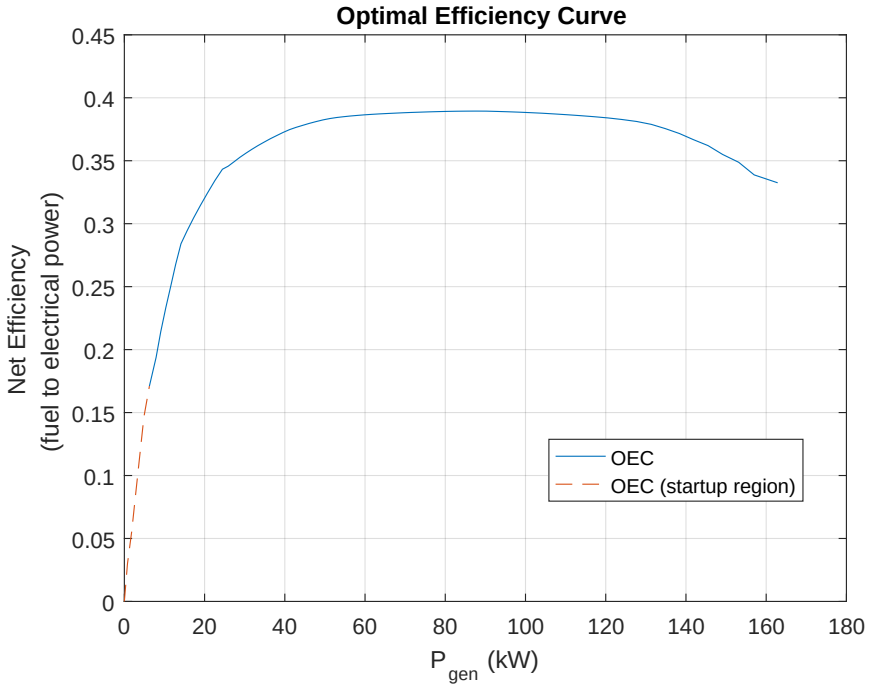

FIGURE 2.5. Optimal efficiency versus P_{gen}.

The state of charge is a normalized measure of battery charge where $SOC_b = 100\%$ is fully charged and $SOC_b = 0\%$ is fully discharged. V_T is the battery cell terminal voltage. Nominal parameter values are given in Table 2.2.

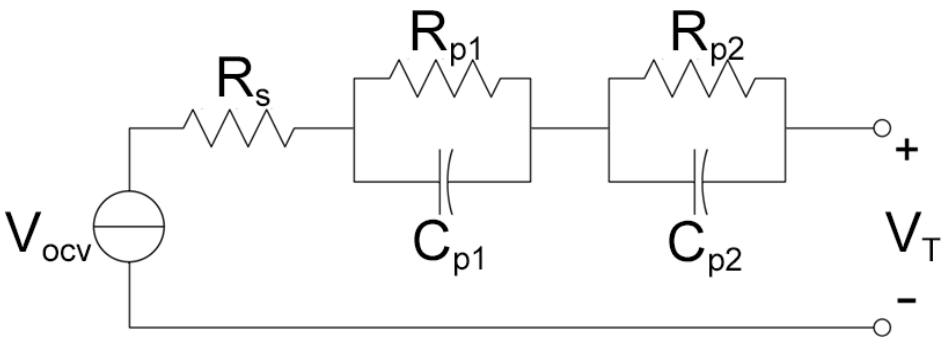

FIGURE 2.6. Battery pack equivalent circuit, full model.

TABLE 2.2. Battery model parameters.

Parameter	Variable	Value
Battery Cells Series	N_{ser}	variable
Battery Series sets in Parallel	N_{par}	variable
Total Charge Capacity	Q_{batt}	3.3Ah
Nominal Open Circuit Voltage	V_{ocv}	2.3v
Nominal Equivalent Resistance	R_s	8.8 mΩ

The dynamics for this model are given by

$$\dot{q}_{p1} = I_{batt} - \frac{q_{p1}}{R_{p1}C_{p1}} \tag{2.21}$$

$$\dot{q}_{p2} = I_{batt} - \frac{q_{p2}}{R_{p2}C_{p2}} \tag{2.22}$$

where I_{batt} is the battery current, positive when discharging, and the q_{pi} terms are the charges in the capacitance elements. The terminal voltage is given by

$$V_T = V_{ocv} - R_s I_{batt} - \frac{q_{p1}}{C_{p1}} - \frac{q_{p2}}{C_{p2}} \tag{2.23}$$

For energy management applications, it is generally more convenient to deal with power flow rather than voltage and current. The next few steps show how to transform the problem to treat power as an input rather than current. Letting $P_{batt,cell}$ be the power going to or from the battery cell,

$$P_{batt,cell} = I_{batt} V_T \tag{2.24}$$

Then, solving this for the current and substituting it into Equation 2.23 and solving yields

$$V_T^2 = \left(V_{ocv} - \frac{q_{p1}}{C_{p1}} - \frac{q_{p2}}{C_{p2}} \right) V_T - P_{batt,cell} R_s \tag{2.25}$$

$$V_T = \frac{1}{2} \left(V_{ocv} - \frac{q_{p1}}{C_{p1}} - \frac{q_{p2}}{C_{p1}} + \sqrt{\left(V_{ocv} - \frac{q_{p1}}{C_{p1}} - \frac{q_{p2}}{C_{p2}} \right)^2 - 4 P_{batt,cell} R_s} \right) \tag{2.26}$$

For a given power coming from or going to the battery, the terminal voltage can be computed from Equation 2.26, and this result can be substituted into Equation 2.24 to obtain the charging

or discharging current. Finally, the SOC is tracked using Coulomb counting.

$$\frac{d}{dt}SOC_b = -\frac{I_{batt}}{Q_{batt}} \tag{2.27}$$

where Q_{batt} is the battery cell's capacity in Coulombs, and where I_{batt} again is positive when discharging.

Like state of charge is a normalized measure of charge, the C-rate is a normalized measure of current that is commonly used in battery aging models. The C-rate is defined as

$$C\text{-}rate = \frac{I_{batt}}{Q_{batt,Ah}} \tag{2.28}$$

where $Q_{batt,Ah}$ is the battery capacity in units of Amphere-hours (Ah). So for example, a C-Rate of 1C means the battery would fully charge or discharge in one hour, a C-rate of two means it would fully charge or discharge in half an hour, and a C-rate of 1/2 means it would fully charge or discharge in two hours.

However, the model given above is not necessarily appropriate for control development. Control-oriented modeling requires minimal states to avoid curse-of-dimensionality problems. So, this 2nd-order model is reduced to the simple quasi-static model shown in Figure 2.7.

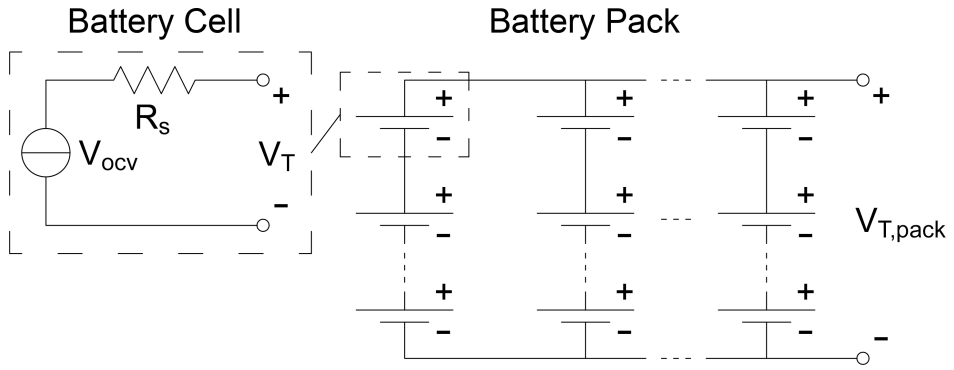

FIGURE 2.7. Reduced-order battery model and battery pack equivalent circuit.

Without the capacitance elements, Equations (2.26) reduces to

$$V_T = \frac{1}{2}\left(V_{ocv} + \sqrt{V_{ocv}^2 - 4 \cdot P_{batt,cell} \cdot R_{eq}}\right) \tag{2.29}$$

The battery current can once again by found by substituting the terminal voltage into Equation (2.24) and solving.

Next, individual cells are combined in series, and then sets of cells in series are combined in parallel, as shown in Figure 2.7. The overall power to or from the battery pack is given by

$$P_{batt} = N_{ser} N_{par} P_{batt,cell} \tag{2.30}$$

while the battery pack equivalent resistance $R_{s,pack}$, open-circuit voltage $V_{ocv,pack}$, and current $I_{batt,pack}$ are given by

$$I_{batt,pack} = N_{par} \cdot I_{batt} \tag{2.31}$$

$$R_{s,pack} = R_s \cdot \frac{N_{ser}}{N_{par}} \tag{2.32}$$

$$V_{ocv,pack} = N_{ser} \cdot V_{ocv} \tag{2.33}$$

Although the number of cells used in the battery pack may be variable between experiments, in general the number of cells in series is chosen to ensure that the battery pack OCV is in line with the requirements of [**77**], while the number of parallel sets is chosen so that the bus can meet the specific requirements like range or power thresholds [**74**, **77**].

2.2.2. Ultracapacitor. The ultracapacitor modules for vehicle simulation are modeled as a 4th-order ladder circuit depicted in Figure 2.8.

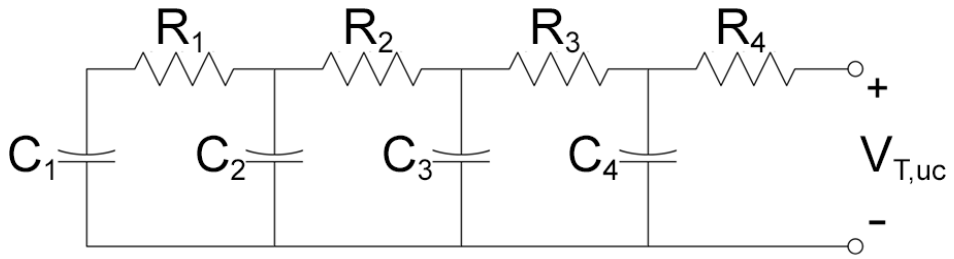

FIGURE 2.8. Ultracapacitor pack equivalent circuit.

where $V_{T,uc}$ is the terminal voltage, the R_is are the capacitor resistances, and the C_is are the capacitances. This research uses 100F ultracapacitor modules, a common size in the existing literature [**63**, **78**, **79**, **80**]. Reference [**81**] develops an experimentally-validated 100F UC model,

with dynamics

$$\dot{q}_1 = \frac{1}{R_1}\left(\frac{q_2}{C_2} - \frac{q_1}{C_1}\right) \tag{2.34}$$

$$\dot{q}_2 = \frac{1}{R_2}\left(\frac{q_3}{C_3} - \frac{q_2}{C_2}\right) - \frac{1}{R_1}\left(\frac{q_2}{C_2} - \frac{q_1}{C_1}\right) \tag{2.35}$$

$$\dot{q}_3 = \frac{1}{R_3}\left(\frac{q_4}{C_4} - \frac{q_3}{C_3}\right) - \frac{1}{R_2}\left(\frac{q_3}{C_3} - \frac{q_2}{C_2}\right) \tag{2.36}$$

$$\dot{q}_4 = \frac{1}{R_4}\left(-I_{uc} - \frac{q_4}{C_4}\right) - \frac{1}{R_3}\left(\frac{q_4}{C_4} - \frac{q_3}{C_3}\right) \tag{2.37}$$

where each q_i is the charge in the charge in the i-th capacitor element and where I_{uc} is positive when discharging. Like with the battery, it is desirable to directly set the capacitor power.

$$P_{uc} = I_{uc} V_{T,uc} \tag{2.38}$$

Then from Equation (2.38) and terminal voltage definition

$$V_{T,uc} = \frac{q_4}{C_4} - R_4 I_{uc} \tag{2.39}$$

again where I_{uc} is positive when discharging, we obtain

$$V_{T,uc}^2 - \frac{q_4}{C_4} V_{T,uc} + R_4 P_{uc} = 0 \tag{2.40}$$

$$V_{T,uc} = \frac{1}{2}\left(\frac{q_4}{C_4} + \sqrt{\frac{q_4^2}{C_4^2} - 4 P_{uc} R_4}\right) \tag{2.41}$$

and the current can be obtained from Equations (2.38) and (2.41). The parameters for this model are given in Table 2.3.

TABLE 2.3. Ultracapacitor full model parameters.

Variable	**Value**	**Variable**	**Value**
C_1	31.7 F	R_1	29.6 $m\Omega$
C_2	53.2 F	R_2	4.94 $m\Omega$
C_3	18.9 F	R_3	1.47 $m\Omega$
C_4	2.08 F	R_4	8.32 $m\Omega$

For control-development, the above model is reduced to the first-order equivalent circuit shown in Figure 2.9, where

$$R_{uc} = R_1 + R_2 + R_3 + R_4 \tag{2.42}$$

$$C_{uc} = C_1 + C_2 + C_3 + C_4 \tag{2.43}$$

The ultracapacitor pack, similar to the battery pack, consists of ultracapacitors arranged in N_{pc} modules in a parallel set and N_{sc} sets in series. The parameters for this reduced-order model are given in Table 2.4. The number of modules is variable so that the effectiveness and cost-benefit of the HESS can be considered across a range of designs.

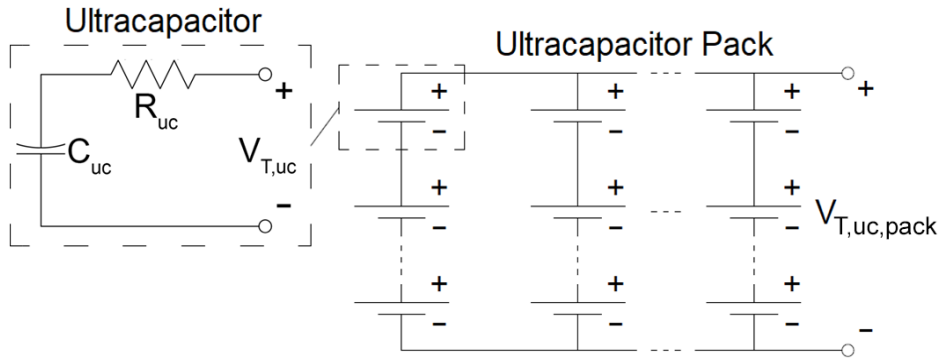

FIGURE 2.9. Ultracapacitor pack equivalent circuit.

TABLE 2.4. Ultracapacitor reduced-order model parameters.

Parameter	**Variable**	**Value**
UC modules in Series	N_{sc}	variable
UC Series sets in Parallel	N_{pc}	variable
Resistance	R_{uc}	44.3mΩ
Capacitance	C_{uc}	105.9F

Adapting Equations (2.38)–(2.41) to the reduced-order model gives

$$V_{T,uc} = \frac{q_{uc}}{C_{uc}} - I_{uc}R_{uc} \tag{2.44}$$

$$V_{T,uc}^2 = \frac{q_{uc}}{C_{uc}} \cdot V_{T,uc} - P_{uc}R_{uc} \tag{2.45}$$

$$V_{T,uc} = \frac{1}{2}\left(\frac{q_{uc}^2}{C_{uc}^2} + \sqrt{\frac{q_{uc}}{C_{uc}} - 4P_{uc}R_{uc}}\right) \tag{2.46}$$

$V_{T,uc}$ can then be substituted back into Equation (2.38) to obtain the ultracapacitor current. Then, the state equation for the capacitor is

$$\dot{q}_{uc} = -I_{uc} \tag{2.47}$$

The UC pack is connected to the DC bus through a converter, as shown in Figure 2.2. The converter allows the UC pack to operate independently of the DC bus voltage. The ultracapacitor power is indicated by P_{uc}, where P_{uc} is positive while discharging and negative while charging. Then, the total UC pack has power $P_{uc,pack}$ given by

$$P_{uc,pack} = N_{pc} N_{sc} P_{uc} \tag{2.48}$$

Then for the complete ultracapacitor pack,

$$I_{uc,pack} = I_{uc} \cdot N_{pc} \tag{2.49}$$

$$V_{T,uc,pack} = V_{T,uc} \cdot N_{sc} \tag{2.50}$$

$$R_{uc,pack} = R_{uc} \cdot \frac{N_{sc}}{N_{pc}} \tag{2.51}$$

where $I_{uc,pack}$ is the total current going to or from the UC pack, $V_{T,uc,pack}$ is the terminal voltage of the overall UC pack, and $R_{uc,pack}$ is the equivalent series resistance of the entire pack.

Finally, the UC pack's DC-DC converter is assumed to have an efficiency of $\eta_{conv} = 95\%$ [**63**]. So, the power coming from or going to the UC at the DC bus $P_{uc,bus}$ is given by

$$P_{uc,bus} = \begin{cases} P_{uc,pack} \cdot \eta_{conv} & P_{uc,pack} \geq 0 \\ P_{uc,pack} / \eta_{conv} & P_{uc,pack} < 0 \end{cases} \tag{2.52}$$

and the losses from the converter are given by

$$P_{uc,conv\text{-}loss} = |P_{uc,pack} - P_{uc,bus}| \tag{2.53}$$

2.3. Energy Storage System Aging

2.3.1. Battery Aging: Cycle Counting Method. This research considers two methods of modeling battery aging; the first is a cycle-life aging model developed in Reference [**24**]. A simpler version of cycle counting is used for aging analysis in works such as [**19**, **27**, **82**]; Reference [**24**] extends the method to handle more variable operating conditions and include additional aging

factors such as current and temperature. This section begins by explaining the basic method, which considers only depth of discharge, and from that develops it into the model in Reference [**24**] and further into an aging model that can be used in dynamic control of the energy storage systems.

First, we consider a simple aging model that determines the cycle life CL of a battery as a function of the depth of discharge DoD of each cycle.

$$CL = f(DoD) \tag{2.54}$$

The functional relationship between cycle life and depth of discharge is logarithmic in nature, and a curve fit to experimental data between measured discharge depth and cycle life is used model the relationship. Reference [**82**] for instance fits data to the form

$$CL = \beta_0 \times DOD^{-\beta_1} \times \exp\left(\beta_2(1 - DOD)\right) \tag{2.55}$$

where the β_i terms are fitted parameters, while Reference [**24**] fits data to the form

$$CL = a_1 e^{a_2 \cdot DoD} + a_3 e^{a_4 \cdot DoD} \tag{2.56}$$

where the a_i terms are curve fit parameters.

Reference [**24**] then extends the function in Equation (2.54) to model the cycle life of a battery as a function of depth of discharge DoD, charging current I_c, discharging current I_d, and temperature T.

$$CL = f(DoD, I_c, I_d, T) \tag{2.57}$$

This model starts as a simple curve fit of cycle life to depth-of-discharge per Equation 2.56 at a reference point of $I_c = 1C$, $I_d = 1C$, $T = 25°C$. This baseline cycle life is denoted CL_{DoD}. The cycle life is then obtained by modifying CL_{DoD} based on the actual operating I_c, I_d, and T.

$$CL = CL_{DoD} \cdot A_{I_d} \cdot A_{I_c} \cdot A_T \tag{2.58}$$

where

$$CL_{DoD} = a_1 e^{a_2 \cdot DoD} + a_3 e^{a_4 \cdot DoD} \tag{2.59}$$

$$A_{I_d} = \frac{a_5 e^{a_6 \cdot I_d} + a_7 e^{a_8 \cdot I_d}}{a_5 e^{a_6} + a_7 e^{a_8}} \tag{2.60}$$

$$A_{I_c} = \frac{a_9 e^{a_{10} \cdot I_c} + a_{11} e^{a_{12} \cdot I_c}}{a_9 e^{a_{10}} + a_{11} e^{a_{12}}} \tag{2.61}$$

$$A_T = \frac{a_{13} T^3 + a_{14} T^2 + a_{15} T + a_{16}}{25^3 a_{13} + 25^2 a_{14} + 25 a_{15} + a_{16}} \tag{2.62}$$

where the a_i terms are again curve fit parameters. The a_5–a_8 parameters are found from a curve fit of cycle life to varying I_d for $I_c = 1C$, $T = 25°$, and $DoD = 100\%$. The a_9–a_{12} parameters are found from a curve fit of cycle life to varying I_c for $I_d = 1C$, $T = 25°$, and $DoD = 100\%$. The a_{13}–a_{16} parameters are found from a curve fit of cycle life to varying T for $I_d = 1C$, $I_c = 1C$, and $DoD = 100\%$.

The cycle life model in [**24**] assumes uniform charge and discharge cycles over the life of the battery. To handle the non-uniform cycles of vehicle operation, we can apply the Palmgren-Miner (PM) rule, a method originally developed for analyzing material fatigue life that has been shown to effectively approximate the battery health over non-uniform charge and discharge cycles [**11**, **82**]. Under the assumptions of this method, each charge and discharge cycle damages the battery an amount equal to the inverse of the cycle life at that cycle's operating conditions. In other words, if we assume a cycle k with depth of discharge DoD_k, charge current magnitude $I_{c,k}$, discharge current magnitude $I_{d,k}$, and temperature T_k, then the cycle life for these operating conditions is CL_k. Under the PM rule, this cycle damages the battery by an amount D_k given by

$$D_k = \frac{1}{CL_k} \tag{2.63}$$

The PM rule assumes that damage accumulates linearly for each charge and discharge cycle. So, the damage from each individual cycle can be summed to find the total damage. The total damage D_{tot} through the k-th cycle is therefore

$$D_{tot}(k) = \sum_{i=1}^{k} D_i \tag{2.64}$$

where each D_i represents the damage from a single cycle with operating conditions DoD_i, $I_{c,i}$, $I_{d,i}$, and T_i. In this way, the damage of individual cycles with unique operating conditions are summed to get a total measure of battery health.

The rainflow-counting method [**83**] is used to transform the irregular charge-discharge patterns of vehicle operation, such as from regenerative braking, into an equivalent set of independent

charge-discharge cycles. For example, consider the SOC profile shown in Figure 2.10: Three smaller cycles of $DoD = 20\%$ are contained within a larger $DoD = 100\%$ cycle. The rainflow-counting algorithm identifies the start and end of these smaller cycles, and the Palmgren-Miner rule is used to evaluate their individual contributions to the overall battery aging. Full descriptions of rainflow-counting algorithms can be found in [**83**,**84**,**85**,**86**], and applications of rainflow-counting to battery degradation problems can be found, for example, in [**86**, **87**, **88**, **89**, **90**].

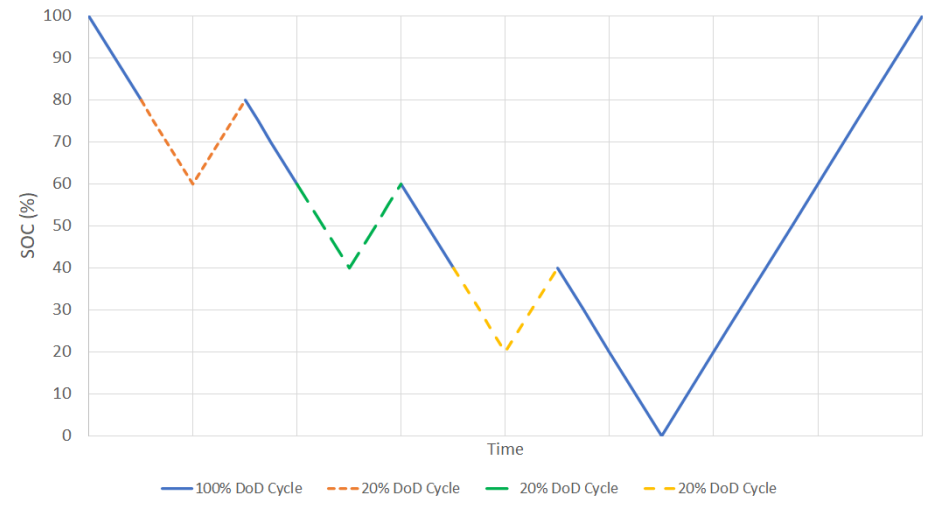

FIGURE 2.10. Example irregular SOC trajectory. Rainflow-counting identifies the individual cycles within the larger trajectory.

Note that [**24**] (and therefore applications of [**24**] in this research) does not consider the effect of where the charge-discharge cycle is centered. Other works, such as [**19**], do account for this affect.

Zero total damage indicates that the battery is at its beginning of life (BOL), while total damage of one indicates the battery's end of life (EOL). Battery end-of-life corresponds to 20% capacity fade, so the capacity fade CF can be put in terms of the damage as

$$CF(k) = 0.2 \cdot D_{tot}(k) \tag{2.65}$$

The above method requires full knowledge of the charge and discharge time histories, which is not practical for use in energy management; the EMS must act at a much faster rate than the pace at which these cycles develop. It is possible, however, that the EMS could determine how a control decision might cause the damage from the current cycle to lessen or grow. For instance,

imagine a battery operating at conditions of DoD_j, $I_{c,j}$, $I_{d,j}$, T_j. Then, let the energy management system make some decision that produces new operating conditions of DoD_k, $I_{c,k}$, $I_{d,k}$, T_k. Using Equations (2.57) through (2.63), the change in damage ΔD due to the EMS's decision can be computed as

$$\Delta D = D_k - D_j = \frac{1}{f(DoD_k, I_{c,k}, I_{d,k}, T_k)} - \frac{1}{f(DoD_j, I_{c,j}, I_{d,j}, T_j)} \tag{2.66}$$

The rainflow-counting method from [**86**], for instance, could be applied to track discharge depth in real time. Then, an energy management strategy could incorporate Equation (2.66) for a measure of potential battery damage. In this way the strategy would try to minimize the change in damage from the control decision made at each time step. Note that when controlling aging in this manner, the EMS can only be aware of the DoD up until the current point in time and can only assess damage relative to the current DoD, while the "true" aging depends on the size of the completed cycle. Despite this discrepancy, this method still proves an effective way to control battery aging, as will be shown in later chapters.

The resistance growth model in Reference [**24**] can be treated in an identical manner to Equations (2.57)–(2.66). The capacity fade and resistance growth models both use rainflow counting as in [**91**] to determine the aging from the irregular cycling operations experienced while a vehicle is in operation. For simplicity, it is assumed that the battery operates at a constant internal temperature of 35°C.

2.3.2. Battery Aging: Power Law Model. The second aging model in this research is the power law aging model presented in Reference [**21**]. This model has been used for aging control in, for example, references [**4**, **5**, **63**]. Reference [**21**] developed a lithium-ion battery empirical aging model for normalized battery capacity loss Q_{loss}, based on an Arrhenius equation. The model uses experimental data to relate battery degradation to charge throughput in ampere-hours Ah, normalized current I_b, and temperature T.

$$Q_{loss} = A(I_b) \exp\left(\frac{-E_a + B|I_b|}{RT}\right) Ah^z \tag{2.67}$$

E_a, B, and z are fitted parameters, while $A(I_b)$ is a fitted function of normalized current. R is the ideal gas constant. Note that Equation (2.67) only considers the absolute value of I_b and that charge throughput is the integral of the absolute value of the current. So, this model is only

concerned with the *magnitude* of current; discharging the battery and charging it (such as from regenerative braking) are handled identically.

Here, Q_{loss} is a normalized measure of capacity fade: $Q_{loss} = 0$ indicates BOL and $Q_{loss} = 1$ indicates complete capacity fade, such that the battery can no longer hold any charge at all. Then, $Q_{loss} = 0.2$ indicates a 20% decrease in the storage capacity that corresponds to the standard definition for battery EOL [**27**]. This model treats current and temperature as static values. So, Equation (2.67) can be differentiated to form a dynamic aging model as follows:

$$\frac{dQ_{loss}}{dt} = A(I_b) \exp\left(\frac{-E_a + B|I_b|}{RT}\right) z(Ah)^{z-1} \frac{dAh}{dt} \tag{2.68}$$

Finally, in order to express the aging in the same units as the cycle-counting method, Q_{loss} is converted to a damage term, where total damage of $D_{tot} = 1$ corresponds to battery EOL at $Q_{loss} = 0.2$.

$$D_{tot} = \frac{Q_{loss}}{0.2} \tag{2.69}$$

Then, the change in damage ΔD over a given time-step Δt is

$$\Delta D = \frac{1}{0.2} \times \frac{dQ_{loss}}{dt} \times \Delta t \tag{2.70}$$

This change-in-damage term can be used in an energy management system in an identical manner to the change in damage derived from cycle-counting, given in Equation (2.66).

However, using Equations (2.68)–(2.70) for control requires recording the total ampere throughput over the entire life of the battery. Literature that uses this aging model for control conventionally neglects the throughput component and instead uses a "severity factor" that represents the relative aging of the battery with respect to nominal operating conditions [**5**, **67**, **92**, **93**], and in effect treats battery damage as accumulating linearly, similar to the cycle-counting model. The severity factor is defined as follows. First, the total ampere-hour throughput at battery end-of-life is found by solving Equation 2.67 for Ah and defined in terms of the operating current I_b and temperature T.

$$Ah_{EoL}(I_b, T) = \left(\frac{20\%}{A(I_b)} \exp\left(\frac{-E_a + B|I_b|}{RT}\right)\right)^{1/z} \tag{2.71}$$

Then, the severity factor σ as a function of current and temperature is defined as the ratio of the end-of-life throughput at a nominal current I_{nom} and temperature T_{nom}, typically 1C and 25°

respectively, to the end-of-life throughput at a given current and temperature.

$$\sigma(I_b, T) = \frac{Ah_{EoL}(I_{nom}, T_{nom})}{Ah_{EoL}(I_b, T)} \tag{2.72}$$

So, if operating conditions are harsher than the nominal conditions, the end-of-life throughput will be smaller, and thus the severity of those conditions is higher. Controllers using this method typically minimize the *effective* throughput Ah_{eff}, where the effective throughput rate is defined as

$$\frac{dAh_{eff}}{dt} = \sigma(I_b, T)\frac{dAh}{dt} \tag{2.73}$$

This can be read as: the change in throughput $\frac{dAh}{dt}$ at the current operating conditions I_b and T are equivalent to a change in throughput $\frac{dAh_{eff}}{dt}$ at nominal operating conditions I_{nom} and T_{nom}. As mentioned earlier, this is essentially a linear accumulation of damage.

$$\frac{dAh_{eff}}{dt} = \sigma(I_b, T)\frac{dAh}{dt} \tag{2.74}$$

$$\frac{dAh_{eff}}{dt} = \frac{Ah_{EoL}(I_{nom}, T_{nom})}{Ah_{EoL}(I_b, T)}\frac{dAh}{dt} \tag{2.75}$$

$$\frac{1}{Ah_{EoL}(I_{nom}, T_{nom})}\frac{dAh_{eff}}{dt} = \frac{1}{Ah_{EoL}(I_b, T)}\frac{dAh}{dt} \tag{2.76}$$

That is, the aging over a particular window of time is equal to the instantaneous throughput divided by the cycle life throughput at the operating conditions over that timespan. So, a change in damage ΔD over a given time-step Δt can be defined as

$$\Delta D = \frac{dAh}{dt}\frac{1}{Ah_{EoL}(I_b, T)}\Delta t \tag{2.77}$$

Once again, this change-in-damage term can be used in an energy management system in an identical manner to the change in damage terms from Equations (2.66) and (2.70).

It should be noted that this method does not model any resistance growth in the battery.

2.3.3. Model Limitations. The models [**21**,**24**] presented in the last two subsections are both prominent models in the literature, with each used in a plethora of vehicle battery aging studies. They were chosen for this work for their prominence in the literature, because their respective authors provided sufficient data and clear methodology to fully reproduce their work, and because

both models readily lend themselves to use in control. However, both models leave off certain dynamics that limit their accuracy. For completeness, some of these limitations are discussed here.

The cycle-counting model, for instance, does not account for a charge-discharge cycle's center point. In other words, a cycle from $SOC = 100\%$ to 80% and back to 100% is counted the same as a cycle from $SOC = 20\%$ to 0% and back to 20%. The power-law model similarly does not capture the effect of SOC during cycling. [**5**] for instance applies a SOC-based modifier to Equation (2.67) to increase the severity of aging at high SOC. [**17**] on the other hand applies a similar modifier, but to account for extra damage during deep discharge cycles. Although both the power-law and cycle-counting models in this work include temperature effects, a battery thermal model is not employed so the effect of that aspect of aging is limited.

Most notably, neither the cycle-counting nor power-law model includes calendar aging effects. Calendar aging is battery degradation associated with time since manufacture rather than throughput or cycling, and is amplified by high temperature and high state-of-charge [**94**]. For instance, reference [**94**] describes the individual effect calendar aging, while [**26**] models calendar aging alongside cycle aging. Although calendar aging is not considered in the majority of this work, it is explored briefly in Chapter 6 to ensure the work developed on simpler models still holds up.

2.4. Model Selection

The studies presented later in this work use the models from this chapter, although the choice of a simple or complex model may vary depending on the particular application. The uses of each model are collected here for reference.

First, all models use the vehicle dynamics presented in Section 2.1. Vehicle parameters, component sizings, and the like are given in each particular chapter.

Chpater 4 presents an electric vehicle with onboard photovoltaics. Because of the large battery used in this model, the steady power flow from the PV, and the computational effort needed to simulate a year's worth of driving for proper PV analysis, the battery uses the simple quasi-static model for dynamics and discharge depth alone, per Equation 2.55 for aging.

Chapter 5 introduces hybrid energy storage using an ultracapacitor. This study uses the 4th-order ultracapacitor dynamics and the 2nd-order battery dynamics models for simulation, and the 1st-order ultracapacitor and quasi-static battery models for control development. Both simulation

and control make use of the cycle counting approach presented in Subsection 2.3.1 and consider discharge depth, charging current magnitude, and discharging current magnitude as variable aging factors. Battery thermal models and thermal management systems are outside the scope of this work, so a constant elevated temperature of 35°C for the battery is assumed.

Chapter 6 continues studying hybrid energy storage systems and uses the same dynamic models as Chapter 5. For battery aging, this study considers both the cycle-counting method as used in Chapter 5 and also the power-law method (including the severity factor approach) for control, and both the cycle-counting method and power-law method for simulation. The cycle-counting approach considers the same variables as in Chapter 5, while the power-law method considers throughput and current magnitude as variable aging factors, while temperature is again assumed constant.

Chapter 7 presents two studies: The first considers series hybrid energy management and does not consider aging, so the quasi-static model is used for battery dynamics. Ultracapacitor models and aging models are not applicable. The second study concerns battery aging in an electric vehicle with hybrid energy storage, and uses the same models for both dynamics and control as Chapter 6.

CHAPTER 3

Dynamic Programming Approaches

This research makes extensive use of the dynamic programming method for energy management. This chapter describes three different approaches to dynamic programming control. Specific control methods, e.g. the cost functions and constraints used, are described in later chapters as they apply to specific studies.

In all cases, the dynamic programming problem considers a discrete-time dynamic system

$$x(k+1) = f(x(k), u(k), w(k)) \tag{3.1}$$

where $x(k)$ is the state vector at time k, $u(k)$ is the control vector, and $w(k)$ is a vector of any exogenous variables, such as commanded inputs or disturbances. x, u, and w are assumed to exist in finite ranges $x \in X$, $u \in U$, and $w \in W$.

Implementation of DP for control involves quantizing the state, control, and possibly exogenous variables into discrete grids of points

$$x(k) \in X = x_i,\ i = 1,\ \ldots,\ N_x \tag{3.2}$$

$$u(k) \in U = u_i,\ i = 1,\ \ldots,\ N_u \tag{3.3}$$

$$w(k) \in W = w_i,\ i = 1,\ \ldots,\ N_w \tag{3.4}$$

where N_x, N_u, and N_w are the total number of discrete points in X, U, and W respectively. The DP problem is solved for these points only. Interpolation can then be used to find the control u for an exact value of x or w.

3.1. Deterministic Dynamic Programming

Deterministic dynamic programming (DDP) is a technique for finding the globally optimal control for a discrete-time dynamic system through use of a priori knowledge of driver behavior. DDP for energy management has been covered extensively in the literature—per [**95**], several dozen

papers have been written on DDP for HEV energy management. In this method, the full trajectory of $w(k)$ is assumed to be known exactly as a function of time. Then, the optimal control u^* is given as a function of state variables and time

$$u(k) = u^*(x(k), k) \tag{3.5}$$

Here, u^* is the optimal control that minimizes the cost function

$$J = \sum_{k=0}^{N} L(x(k), u(k), w(k)), \tag{3.6}$$

defined in terms of an instantaneous cost function $L(x, u, w)$ and where N represents the final time and $k = 0, \ \ldots, \ N$.

The optimal control is found by minimizing Equation (3.6) through application of Bellman's Principle of Optimality. A recursive cost-to-go function $V(x, k)$ is first used to find the optimal control at final time N. Then, a backwards in time update is used to find the optimal control from time $N - 1$ to N, followed by the optimal control from $N - 2$ to N, and so on.

$$V(x, N) = \min_{u \in U} \{L(x, u, w(N))\} \tag{3.7}$$

$$V(x, k) = \min_{u \in U} \{L(x, u, w(k)) + V(f(x, u, w(k)), k + 1)\} \tag{3.8}$$

$$\text{for } k = N - 1, \ \ldots, \ 0$$

$V(x, k)$ is evaluated for each $x \in X$, so that $V(f(x, u, w(k)), k + 1)$ can be interpolated from the prior update. The optimal control is found by a direct search of $u \in U$. Then, the optimal control u^* is given by

$$u^*(x, k) = \arg\min_{u \in U} \{L(x, u, w(k)) + V(f(x, u, w(k)), k + 1)\} \tag{3.9}$$

Although this method produces the global optimal control, it clearly is non-causal and not implementable: it requires exact knowledge of $w(k)$ from time $k = 0$ to $k = N$ before the optimal control can be found. Nonetheless, DDP provides a useful benchmark of performance for other types of control.

Note that some works such as [**96**, **97**] use the deterministic dynamic programming results to form a causal rule base. This method is not considered in this work.

3.2. Stochastic Dynamic Programming

SDP uses a stochastic model of $w(k)$ rather than rely on a priori knowledge. Although this is sub-optimal compared to DDP, it is causal and so can be implemented as a real controller. SDP for HEV energy management has been covered by a variety of literature, such as [**34**, **35**, **98**, **99**]. Because $w(k)$ is based on a stochastic model rather than an exact trajectory, the control must consider the entire range of possible w at each time step, and so becomes a function of x and w, rather than x and k as with DDP.

$$u(k) = u^*(x(k), w(k)) \tag{3.10}$$

The SDP control is found by minimizing *expected* future costs [**35**, **36**] according to

$$J = \mathbf{E}\left[\sum_{k=0}^{N} \gamma^k L(x(k), u(k), w(k))\right] \tag{3.11}$$

where γ is a discount factor $0 < \gamma < 1$ that allows the cost function to converge as $k \to \infty$. In this framework, the expected future costs are found using transition probabilities p_{ij}, where i and j are indexes of W per Equation (3.4) and p_{ij} describes the probability that $w(k+1) = w_j$ given that $w(k) = w_i$. These transition probabilities can be based off of real data or can be assumed to follow a chosen distribution, such as a normal or uniform distribution. An example of forming the transition probabilities with a Markov chain model and real-world data is given later in this section.

A recursive cost-to-go function is used to solve Equation (3.11), this time of the form

$$V(x, w, N) = \min_{u \in U} \{L(x, u, w)\} \tag{3.12}$$

$$V(x, w, k) = \min_{u \in U} \{L(x, u, w) + \gamma \cdot \mathbf{E}\left[V(f(x, u, w), w, k+1)\right]\} \tag{3.13}$$

$$\text{for } k = N-1, \ \ldots, \ 0$$

where

$$\mathbf{E}\left[V(f(x, u, w), w, k+1)\right] = \sum_{j=1}^{N_w} p_{ij} V(f(x, u, w_i), w_j, k+1) \tag{3.14}$$

given the discrete grid of $w \in W$ in Equation (3.4). $V(x, w, k)$ is evaluated for each $x \in X$ and $w \in W$, while the optimal control is found by a direct search of $u \in U$. Note that the expected

future costs in Equation (3.13) are "discounted" by γ over one time-step. Then because V is solved recursively, the expected cost at time N relative to the cost-to-go at $k = 0$ will be discounted by γ^N, the expected cost at time $N - 1$ will be discounted by γ^{N-1}, and so on. For $0 < \gamma < 1$ this ensures that J will converge.

The SDP problem can be treated as a finite horizon problem, where N is a fixed number of updates. Alternatively it can be treated as an infinite horizon problem, where N is arbitrarily large and the updates to the cost-to-go function are carried out until the control policy converges, in other words

$$V(x, w, k) = V(x, w, k + 1) \; \forall \; x \in X \text{ and } w \in W. \tag{3.15}$$

Then, the optimal control u^* is given by

$$u^*(x, w) = \arg\min_{u \in U} \left\{ L(x, u, w) + \gamma \cdot \mathbf{E}\left[V(f(x, u, w), w, 1) \right] \right\}. \tag{3.16}$$

That is, the control that optimizes the final ($k = 0$) update of the cost-to-go function. Although the SDP problem is solved backwards in time like the DDP problem, the resulting control policy is both time-invariant and causal. This is because the SDP problem does not require future knowledge of w; instead it relies on the time-invariant stochastic model.

3.2.1. Driver and Vehicle Stochastic Model. SDP requires a stochastic model of future inputs. For vehicle control, a two-dimensional Markov chain model can be used to represent the driver behavior. For the model presented in Section 2.1, the exogenous variables consist of the vehicle wheel speed ω_{wh} and the driver's electrical power request P_{dem}, given in Equation (2.7) and (2.11) respectively. (To avoid confusion, it should be noted that wheel speed is denoted by ω_{wh} while the set of exogenous variables is denoted with w.) Then per Equation (3.4), P_{dem} and ω_{wh} are partitioned into grids of N_p and N_ω points, respectively.

$$P_{dem} \in \{P_{dem,1}, \ldots, P_{dem,N_p}\} \tag{3.17}$$

$$\omega_{wh} \in \{\omega_{wh,1}, \ldots, \omega_{wh,N_\omega}\} \tag{3.18}$$

The notation w_{ij} can then be used to denote the pair of the i-th element of P_{dem} and the j-th element of ω_{wh}. Given this partitioning, the one-step transition probability $p_{ij,\ell m}$ denotes the probability that if at time k, $P_{dem} = P_{dem,i}$ and $\omega_{wh} = \omega_{wh,j}$, then at time $k + 1$ $P_{dem} = P_{dem,\ell}$

and $\omega_{wh} = \omega_{wh,m}$.

$$p_{ij,\ell m} = \Pr\left[w(k+1) = w_{\ell m} \middle| w(k) = w_{ij}\right] \tag{3.19}$$

$$i, \ell = 1, \ldots, N_p, \quad j, m = 1, \ldots N_\omega$$

$p_{ij,\ell m}$ is found for each w_{ij} by counting the frequency of transitions for a given drive cycle. Per [**35**], if $M_{ij,\ell m}$ is the number of times that w_{ij} transitions to $w_{\ell m}$ during a given driving scenario, and M_{ij} is the number of times that w_{ij} occurs, then the transition probability $p_{ij,\ell m}$ can be found according to

$$p_{ij,lm} = \frac{M_{ij,lm}}{M_{ij}} \tag{3.20}$$

3.3. Minimax Dynamic Programming (MDP)

MDP does not rely on a priori knowledge of $w(k)$, but neither does it use a statistical model to consider future values of $w(k)$. Instead, MDP presumes that for any $x(k)$, the future $w(k+1)$ will be whatever $w \in W$ that maximizes the cost function. This makes MDP-based controllers very robust to worst-case or unexpected operating conditions, but they also tend to be overly conservative, risking reduced performance at nominal operating conditions. An EMS similar to MDP was proposed in [**32**, **36**], in which the EMS was treated as a game theory problem. Like SDP, MDP must consider the entire range of possible w. So, the optimal control is given by

$$u(k) = u^*(x(k), w(k)) \tag{3.21}$$

The MDP control is found by minimizing the maximum possible future costs.

$$J = \max_{w \in W} \left\{ \sum_{k=0}^{N} \gamma^k L(x(k), u(k), w(k)) \right\} \tag{3.22}$$

where γ is a discount factor $0 < \gamma < 1$ that allows the cost function to converge as $k \to \infty$. A recursive cost-to-go function is used to solve Equation (3.22), this time of the form

$$V(x, w, N) = \min_{u \in U} \{L(x, u, w)\} \tag{3.23}$$

$$V(x, w, k) = \min_{u \in U} \left\{ L(x, u, w) + \gamma \cdot \max_{w \in W} \{V(f(x, u, w), w, k+1)\} \right\} \tag{3.24}$$

$$\text{for } k = 0, \ \ldots, \ N-1$$

$V(x, w, k)$ is evaluated for each $x \in X$ and $w \in W$, while the optimal control is found by a direct search of $u \in U$.

Like SDP, the MDP problem can be treated as either a finite horizon problem or infinite horizon problem. In either case, the optimal control u^* is given by

$$u^*(x, w) = \arg\min_{u \in U} \left\{ L(x, u, w) + \gamma \cdot \max_{w \in W} \{V(f(x, u, w), w, 1)\} \right\}, \tag{3.25}$$

the control that optimizes the final update of the cost-to-go function. The resulting control policy is both time-invariant and causal.

3.3.1. Minimax Constraints. Although MDP is presented generally in Equations (3.22)–(3.24), in practice the maximal cost-to-go should be constrained to points reachable from the current state. For instance, a vehicle does not need to consider high accelerations when already at or near the maximum vehicle speed, or large amounts regenerative braking when the vehicle is already stopped. If a bus is at rest, we can be certain that a second later it will not be traveling at 60mph! One possibility in the context of vehicle energy management would be to look at the motor specifications: what electrical power is the motor rated for, and what are the minimum and maximum accelerations that the motor can provide? Then, the exogenous variables (P_{req} and ω_{wh}) can be constrained to what is feasible. The power demand at $k+1$ is constrained to the minimum and maximum electrical power that the electric motor can provide.

$$P_{dem,min} \leq P_{dem}(k+1) \leq P_{dem,max} \tag{3.26}$$

The minimum and maximum wheel speed is variable; it depends on the current wheel speed, the minimum and maximum possible angular acceleration at the wheel, and the time step used when solving the DP problem.

$$\omega_{wh}(k) + \Delta t \cdot \alpha_{min} \leq \omega_{wh}(k+1) \leq \omega_{wh}(k) + \Delta t \cdot \alpha_{max} \tag{3.27}$$

where the minimum and maximum angular accelerations are determined from the vehicle dynamics model and the electric motor's minimum and maximum mechanical power.

Alternatively, one could constrain the minimum and maximum power demand and wheel speed based on observed behavior, such as the largest changes seen on a particular drive cycle. However, this approach would make and MDP controller no longer be drive cycle independent.

3.4. Note on Computation Costs

In general, dynamic programming control strategies are considered too computationally expensive to run in real time on a vehicle [**33**]. Nonetheless, it is still important to compare the computational complexity of these methods. The dynamic programming approach requires breaking the states x, control inputs u, disturbances w into sets of discrete points to be evaluated. So, the complexity of these methods can be compared by looking at the number of individual points that must be optimized. N_{ddp}, N_{sdp}, and N_{mdp} indicates the number of such points for each optimization method.

For simplicity, consider each state to be discretized into M points. Let n_x and n_w to be the number of state and disturbance variables, respectively. For deterministic dynamic programming, the trajectory of w is directly set at teach time step. So, the number of points to optimize is given by

$$N_{ddp} = N \cdot M^{n_x}$$

For SDP, MDP, and MASDP, the expected cost-to-go is dependent on the exact state of w, so all combinations of $x \in X$ and $w \in W$ must be considered. Then,

$$N_{sdp} = N \cdot M^{n_x+n_w}$$

$$N_{mdp} = N \cdot M^{n_x+n_w}$$

The complexity of all DP methods increases exponentially with the number of state variables. This applies a practical limit to DP performance: Adding new states may requiring decreasing the number of points into which state variables are discretized (such as to avoid issues with memory or computation time), which can in turn impact performance.

Comparatively speaking: in order to compute cost-to-go, the computation of the expected value for SDP is more complex than the lookup of a maximum value for MDP. So, although SDP and MDP must optimize the same number of individual points, the points for SDP take longer to compute. Because DDP only ever has a single exogenous input (time) and can look up cost-to-go

values directly, rather than compute expected values or search for maximum values, it generally is less computationally complex than SDP and MDP. However because it is directly dependent on the time-history of the inputs, the entire DDP solution must be stored in memory. MDP and SDP, on the other hand, only need to retain the most recent solution.

CHAPTER 4

On-Board Photovoltaics

The first work done in this dissertation is to investigate supplementing the battery with on-board photovoltaic modules. Electric vehicles operate with large batteries for long hours, so on-board photovoltaics are particularly well suited to this case: PV power could limit the battery's charge throughput but not affect dynamic aging factors like large currents. In this chapter, an on-board photovoltaics model is created to analyze their impact on electric bus range and battery lifespan. Photovoltaic systems that cover the bus roof and bus sides are considered. The bus model is simulated on a suburban bus drive cycle on a bus route in Davis, CA, for a representative sample of yearly weather conditions. Roof-mounted panels increased vehicle driving range by 4.7% on average annually, while roof and side modules together increased driving range by 8.9%. However, variations in weather conditions meant that this additional range was not reliably available. For constant vehicle range, rooftop photovoltaic modules extended battery cycle life by up to 10% while modules on both the roof and sides extended battery cycle life by up to 19%. Although side-mounted photovoltaics increased cycle life and range, they were less weight- and cost-effective compared to the roof-mounted panels.

4.1. Introduction

A possible method to reduce battery cost is to supplement the energy storage system with photovoltaic (PV) modules, so that additional power can be generated while the vehicle is on the road. Flexible PV panels allow for vehicle integration without aerodynamic losses or major infrastructural costs [**44**]. Interest in solar-powered vehicles has been long standing: The first solar-powered "car" dates back to 1955 when General Motors (Detroit, MI, USA) introduced the Sunmobile, a 15-inch long solar-powered vehicle. Various solar-powered or PV-augmented vehicle prototypes were introduced in the following decades [**100**]. Contemporary research for on-board PV (OBPV) can generally be broken into two groups: integrated PV for consumer vehicles and integrated PV for commercial vehicles.

As consumer vehicles are often parked throughout the day, much of the literature regarding consumer vehicles focuses on analyzing and maximizing collected solar energy for parked vehicles. References [**45**] and [**46**], for instance, analyze the day-to-day energy collected from parked vehicles to determine the driving distances for PV-augmented hybrid vehicles that minimize both fuel consumption and wasted solar energy. In [**47**], the relationship between vehicle usage and the impact of OBPV is considered with regards to well-to-wheel vehicle efficiencies and the life-cycle cost of PV cells. Other literature more generally considers the impact of OBPV on fuel consumption and vehicle emissions in an attempt to determine when PV modules will be efficient and inexpensive enough for widespread on-board use [**48**], [**49**].

In contrast, commercial vehicles are generally operated constantly throughout the day so analysis of OBPV on commercial vehicles tends to focus on powering vehicle components and on the long-term benefits of OBPV. For instance, PV modules have been integrated into health emergency vehicles in order to power medical equipment while the engine is not running and to help guarantee a charge when the vehicle must be started [**50**]. In another application, OBPV were shown to provide enough energy to power the refrigeration unit on a delivery vehicle [**51**]. Meanwhile, [**44**] examines the energy collected from roof-mounted PV modules on a diesel-powered bus operating in Poland, noting that such a system "does not require extensive modification to the vehicle electrical system." Experimental results indicated that the free solar energy, used to power auxiliary electrical loads, would quickly provide a positive return on investment. Reference [**52**] evaluates the economic feasibility and environmental impact of OBPV for diesel-powered trucks an buses, showing that OBPV could substantially reduce the carbon footprint of heavy-duty vehicles with a payback time of only two to four years.

Still, the majority of the literature for OBPV with commercial vehicles does not consider all-electric powertrains. A small amount of literature exists for light- and medium-duty commercial electric vehicles: for instance, [**101**] and [**102**] each investigate OBPV for agricultural electric vehicles while [**103**] looks at their impact on light utility electric vehicles.

This research chooses to investigate PV modules integrated on an electric bus. A bus is chosen for two reasons: one, the large, flat roof and sides of a bus provide ample space on which to attach PV modules and collect solar energy; two, the low speeds and frequent idle time of the bus allow

the PV modules to provide a larger share of the traction load compared to, for instance, a truck operating on the highway. This solar energy could be used to extend vehicle driving range.

Alternatively, the energy collected from OBPV could be used to reduce battery discharge instead because buses operate on fixed routes and may not need range extension. An electric vehicle, rather than a hybrid, is considered for this reason. The stored solar energy will reduce the depth of discharge or charge throughput of the battery, potentially increasing the battery cycle life and reducing the lifetime cost of the vehicle. On the other hand, power from PV modules is not controllable in the same way as power from an engine or ultracapacitor, so it cannot be used to affect aging factors like battery temperature or large currents that may be significant in a hybrid vehicle.

In this chapter, both the range-extension and battery cycle life effects of OBPV on electric buses are investigated through a numerical experiment. In Section 4.2, the models of the various components of the electric bus powertrain and PV system are introduced. In Section 4.3, a case study of electric buses with and without OBPV is presented. In Section 4.4, the results from the case study are discussed. Section 4.5 offers conclusions on this research.

4.2. Solar Radiation and Photovoltaics Model

This work is interested in how PV mounted on-board an electric bus affect that bus's stored energy consumption and the vehicle battery's lifespan. In this section, the modeling methods and assumptions are described for the solar radiation and photovoltaics model.

Accurate assessment of the impact of OBPV requires simulating a representative sample of the weather patterns that a real bus would experience. Additionally, simulation of side-mounted panels requires accurate modeling of different types of radiation in order to model the energy from a panel on the side of the bus facing away from the sun.

PV modules collect three types of radiation: Direct radiation, diffuse radiation, and reflected radiation. Direct radiation travels in a straight line from the sun to the PV module, while diffuse radiation has been scattered by atmospheric particles and approaches from many different directions. On a clear, sunny day, direct radiation makes up the vast majority of the radiation experienced by a PV panel. On the other hand, on a heavily clouded day, the total radiation experienced by a PV panel is entirely diffuse [**104**]. Reflected radiation is radiation that strikes the PV module

after having been reflected off some other surface, such as an asphalt road. The three types of solar radiation are illustrated in Figure 4.1. Reflected radiation is not considered in this work.

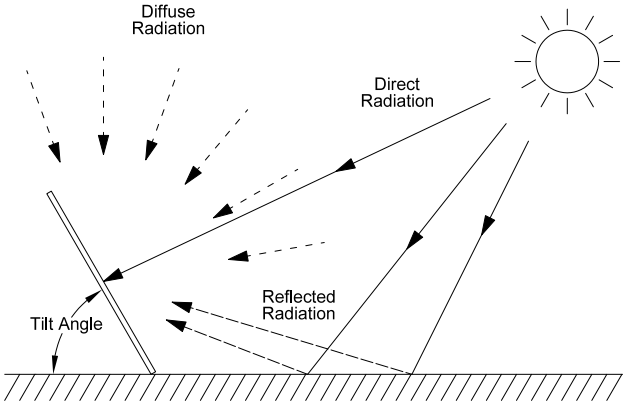

FIGURE 4.1. Types of solar radiation.

Although models exist to obtain an estimate of direct radiation on a clear day based on temporal variables and spatial coordinates [**105**], these models cannot predict the diffuse radiation, due to its dependency on, and the uncertainty of, local weather conditions. Instead, one can use typical meteorological year (TMY) data collected by the National Renewable Energy Lab (NREL) for locations throughout the United States [**106**]. As its name suggests, TMY data is made of 365 days of weather data selected to cover a range of typical weather phenomena while still matching a region's monthly and annual average meteorological data. TMY data sets include measurements of the direct normal irradiance (DNI) and the diffuse horizontal irradiance (DHI). DNI is the radiation experienced by a surface held perpendicular to the incoming radiation, while DHI is the radiation that reaches horizontal surface on an indirect path from the sun. The DNI and DHI time-histories from TMY data are used in the experiment for a PV-augmented bus.

In the following subsections, modifications to the vehicle model presented in Chapter 2 are given first, sizing of the OBPV modules is discussed next, followed by modeling of direct radiation on a moving surface and diffuse radiation on a non-horizontal surface. Finally, the model for conversion of solar power to electrical power is presented.

4.2.1. Vehicle Model. Figure 4.2 shows the power flow of the PV-integrated system. The power supplied to the electric machine is provided by the power from the PV panels, P_{pv}, and the

battery pack, P_{batt}. Equation 2.14 is modified to include the contribution of PV power.

$$P_{batt} = P_{dem} - P_{pv} \tag{4.1}$$

The busbar operates on direct current (DC). DC–DC conversion of the PV power to the voltage of the DC bus is assumed to be lossless. Figure 4.2 depicts the connection of Rooftop PV modules only; PV modules attached to the side of the bus are assumed to each have their own DC–DC converter and are connected to the DC bus in a similar manner to the rooftop modules.

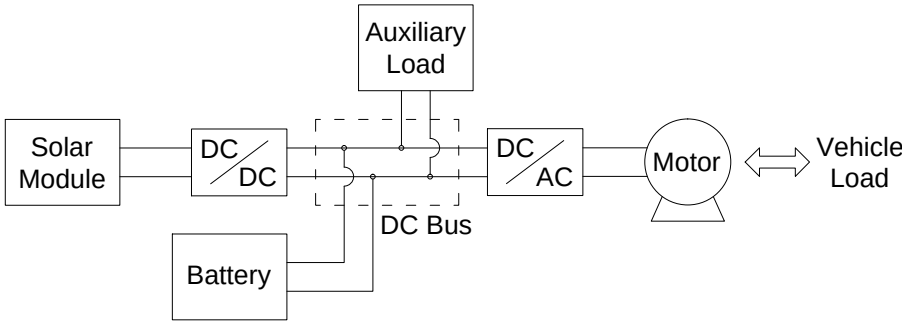

FIGURE 4.2. Diagram of battery, photovoltaic (PV) panel, and motor connections.

4.2.2. Module Sizing. Two PV system configurations are considered in this work: one where modules are mounted only on the roof of the vehicle, and another where modules are mounted on the sides and back of the bus as well. The sizing of the modules on the roof and each of the sides is described below.

The size of the PV modules are estimated from the bus geometry and are used to estimate the rating of the roof and side PV systems [**107**]. The bus is approximated as a box that is 12.9m long, 2.6m wide, and 3.4m tall, with dimensions estimated from manufacturer specifications for an electric transit bus [**108**]. In order to maximize the impact of OBPV, all possible surfaces should be exploited. It is estimated that the roof-mounted panels, used by both configurations, can cover 60% of the bus roof area A_{top}. The right and left side modules each cover the same area of their respective sides, and are estimated to cover 40% of the side area A_{side}, while 75% of the area of the back of the bus A_{back} is covered in PV panels. These areas are denoted $A_{pv,top}$, $A_{pv,right}$, $A_{pv,left}$, and $A_{pv,back}$, respectively.

$$A_{pv,top} = 60\% \cdot A_{top} \tag{4.2}$$

$$A_{pv,right} = 40\% \cdot A_{side} \tag{4.3}$$

$$A_{pv,left} = 40\% \cdot A_{side} \tag{4.4}$$

$$A_{pv,back} = 75\% \cdot A_{back} \tag{4.5}$$

Each of these areas is then multiplied by the surface power density, SPD, under standard reporting conditions (SRC), which are an operating temperature of $T_{SRC} = 25°\text{C}$ and radiation of $G_{SRC} = 1000W/m^2$ [**109**]. The SRC are the laboratory test conditions under which commercial and research PV modules are rated. This produces the rated power, P_{rated}, of the module under SRC as described in Equation (4.6). To avoid writing redundant equations, the bus surfaces are indexed by a subscript i, with $i = top,\ right,\ left,\ back$ referring to each surface of the bus. Then,

$$P_{rated,i} = A_{pv,i} \cdot SPD. \tag{4.6}$$

The surface power density is based on manufacturer data [**110**] for monocrystalline silicone PV cells, which are chosen for their high performance and low aerodynamic profile [**44**]. Based on these calculations, a bus roof can fit a PV system rated for 3,300W, the right and left sides can each fit a system rated for 2,900W, and the back a system rated for 1,100W.

Similarly, the mass of each PV module is determined from the module area and the area density AD of a PV module, again based on manufacturer data [**110**].

$$M_{pv,i} = A_{pv,i} \cdot AD \tag{4.7}$$

The PV mass is then used in Equation (2.4) to determine the total vehicle mass.

The parameters of the PV model are provided in Table 4.1.

TABLE 4.1. PV model parameters.

Parameter	**Variable**	**Value**
Vehicle Roof Area	A_{top}	33.2 m^2
Vehicle Side Area	A_{side}	44.1 m^2
Vehicle Back Area	A_{back}	8.81 m^2
Surface Power Density	SPD	165 W/m^2
Area Density	AD	1.89 kg/m^2
Peak Power Temperature Coefficient	K_{mpp}	-0.43%/°C

4.2.3. Direct Radiation Model. The direct radiation, sometimes called the beam radiation, represents the radiation that travels on a direct path from the sun to the PV panel. When the direct radiation strikes a PV panel tilted away from the direct radiation's path, only the component of the direct radiation that is perpendicular to the panel is converted into electrical energy. For direct normal irradiance with magnitude DNI and an angle of incidence θ_I, the panel experiences beam radiation G_b according to

$$G_b = DNI \cos \theta_I. \tag{4.8}$$

Alternatively, the direct radiation could be defined as a vector $\mathbf{I}$ pointing towards the PV module in a 3D coordinate system. Then, a unit surface normal vector $\mathbf{N}$ could be defined for the PV module. This work uses a convention for the normal vector such that a horizontal panel has a normal vector pointing directly up and a panel that is perpendicular to the direct radiation has a normal vector pointing towards the sun. Then, the incident beam radiation G_b could be obtained by taking the negative dot product of $\mathbf{I}$ and $\mathbf{N}$, with the caveat that if the panel is facing away from the direct radiation, the radiation is zero rather than negative.

$$G_b = \max(0, \langle -\mathbf{I}, \mathbf{N} \rangle) \tag{4.9}$$

Direct radiation is illustrated in Figure 4.3.

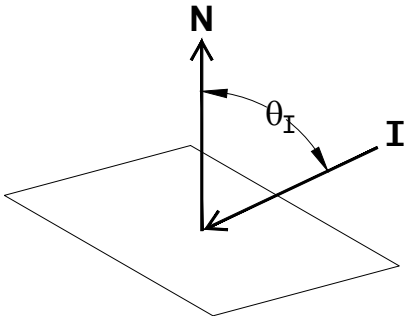

FIGURE 4.3. Direct radiation.

The PV modules under consideration in this work are pitching and turning as the bus pitches and turns, changing the angle of incidence on each surface of the bus at each time-step. In order to obtain the incident beam radiation on moving surfaces, the following method is proposed: The direct radiation is first placed into a global coordinate system and then transformed into a local coordinate system oriented with the moving bus. Meanwhile, surface normal vectors are defined in

the local coordinate system for each PV module on the bus. Then, the incident beam radiation on each surface is obtained using Equation (4.9). This process allows the incident beam radiation on each surface of the vehicle to be obtained at each time-step of the simulation.

The global coordinate system assigns the east/west direction to the x-axis, the north/south direction to the y-axis, and the vertical direction to the z-axis. The azimuth angle θ_A is the angle of the sun along the horizon, where an angle of zero indicates north. The zenith angle θ_Z is the angle of the sun off of the vertical axis. The direct radiation vector in this coordinate system is $\mathbf{I_G}$, where the subscript G indicates the global frame. The global coordinate system is illustrated in Figure 4.4.

The azimuth angle and zenith angle are obtained based on the latitude, longitude, time of day, and time of year at each time-step of the simulation. The process for finding the azimuth and zenith angles is given in [**111**]. For direct normal irradiance with magnitude DNI, obtained from TMY data, and azimuth and zenith angles θ_A and θ_Z, the direct radiation is put into vector form in the global coordinate system such that the direct radiation vector points towards the earth, according to Equation 4.10.

$$\mathbf{I_G} = DNI \cdot \begin{bmatrix} -\sin\theta_A \cdot \sin\theta_Z \\ -\cos\theta_A \cdot \sin\theta_Z \\ -\cos\theta_Z \end{bmatrix} \tag{4.10}$$

The negative signs in Equation (4.10) result from $\mathbf{I_G}$ being defined as traveling from the sun to the bus.

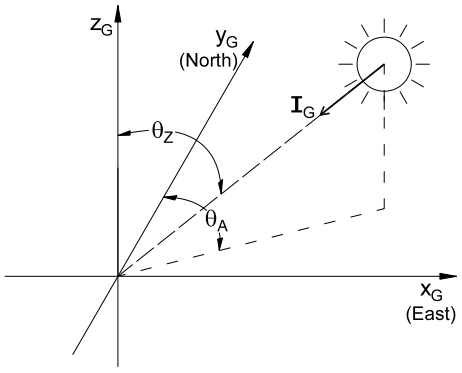

FIGURE 4.4. Global coordinate system.

Next, the vehicle coordinate system is defined such that the first coordinate indicates the lateral direction, the second coordinate indicates the longitudinal direction, the third coordinate indicates the vertical direction. For each axis, the rightward, forward, and upward directions are positive, as shown in Figure 4.5.

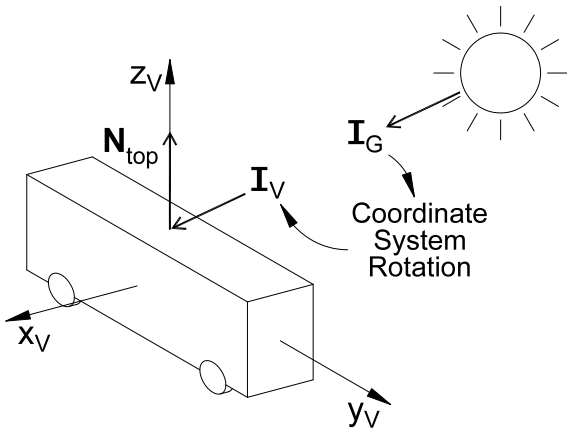

FIGURE 4.5. Bus coordinate system.

Then, for heading ψ and pitch angle θ_p, where $\psi = 0$ indicates north and $\theta_p = 0$ indicates a horizontal surface, $\mathbf{I_G}$ is rotated as shown in Figure 4.6(a) and Figure 4.6(b). These rotations are carried out using the two rotation matrices R_ψ and R_θ, given in Equations (4.11) and (4.12), to obtain the direct radiation vector in the vehicle coordinate system, $\mathbf{I_V}$. $\mathbf{I_I}$ denotes the direct radiation vector in the intermediate coordinate system between the global and vehicle coordinate systems.

$$\mathbf{I_I} = \underbrace{\begin{bmatrix} \cos\psi & -\sin\psi & 0 \\ \sin\psi & \cos\psi & 0 \\ 0 & 0 & 1 \end{bmatrix}}_{R_\psi} \mathbf{I_G} \tag{4.11}$$

$$\mathbf{I_V} = \underbrace{\begin{bmatrix} 1 & 0 & 0 \\ 0 & \cos\theta_p & -\sin\theta_p \\ 0 & \sin\theta_p & \cos\theta_p \end{bmatrix}}_{R_\theta} \mathbf{I_I} \tag{4.12}$$

$$\mathbf{I_V} = R_\theta R_\psi \mathbf{I_G} \tag{4.13}$$

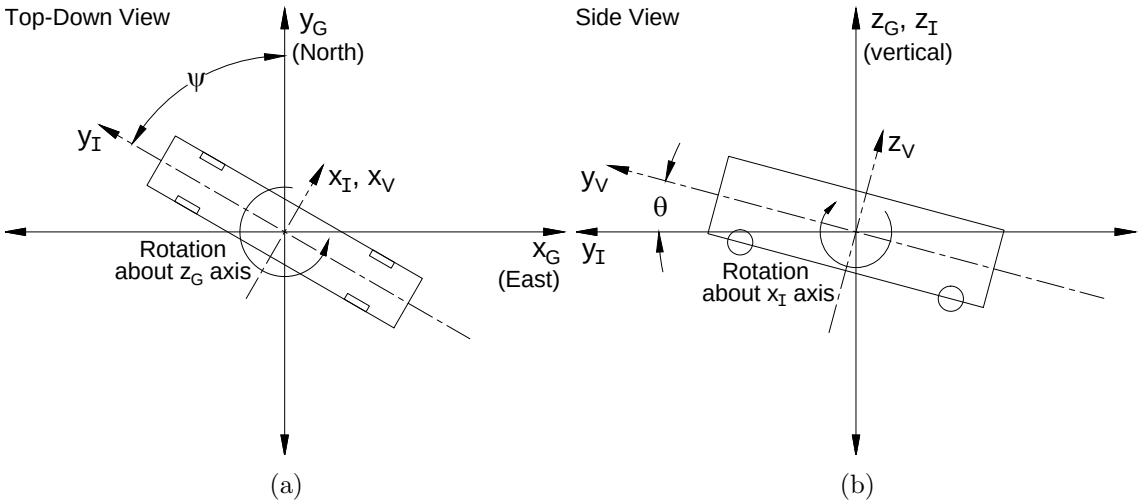

FIGURE 4.6. **(a)** Heading rotation. **(b)** Pitch rotation.

The unit normal vectors for the PV module surfaces are then defined in the vehicle coordinate system for each surface of the bus. The unit normal vector for the top surface is a unit vector pointing straight up, the unit normal vector for the right-side surface is a unit vector pointing directly to the right, and so on. These unit normal vectors are given by Equations (4.14)–(4.17).

$$\mathbf{N_{top}} = \begin{bmatrix} 0 & 0 & 1 \end{bmatrix}^T \tag{4.14}$$

$$\mathbf{N_{right}} = \begin{bmatrix} 1 & 0 & 0 \end{bmatrix}^T \tag{4.15}$$

$$\mathbf{N_{left}} = \begin{bmatrix} -1 & 0 & 0 \end{bmatrix}^T \tag{4.16}$$

$$\mathbf{N_{back}} = \begin{bmatrix} 0 & -1 & 0 \end{bmatrix}^T \tag{4.17}$$

Although this model only uses surfaces with normal vectors along the coordinate system axes, this method could be used for surfaces facing any arbitrary direction.

Then, per Equation (4.9), the incident beam radiation on each surface is given by

$$G_{b,i} = \max(0, \langle -\mathbf{I_V}, \mathbf{N_i} \rangle). \tag{4.18}$$

However, some amount of the direct radiation on the vehicle is expected to be blocked by things such as buildings or overhead trees. An additional efficiency factor η_{shade} is introduced to represent

losses from shading of the PV modules.

$$G_{b,i} = \eta_{shade} \cdot \max(0, \langle -\mathbf{I_V}, \mathbf{N_i} \rangle). \tag{4.19}$$

Based on experimental results in [**44**], it is estimated that $\eta_{shade} = 75\%$. In other words, 25% of all direct radiation is considered lost to shading. Although estimating η_{shade} as constant will reduce the model accuracy on small time scales, it is sufficient for measuring the total radiation over longer time scales, such as an hour or a day.

4.2.4. Diffuse Radiation Model. TMY data provide diffuse radiation as diffuse radiation on a horizontal surface. However, this work considers PV modules mounted on the sides and back of a bus, which are decidedly not horizontal. Additionally, the pitch motion of the bus is considered, so the roof- and back-mounted PV panels experience further tilt. A way to convert diffuse horizontal radiation into diffuse radiation on a tilted surface is needed.

Reference [**112**] compares the accuracy of several diffuse radiation models. Among them is the isotropic sky diffuse model, which models diffuse radiation as uniformly distributed across the sky. Under this modeling assumption, the diffuse radiation on a tilted surface is given by

$$G_d = \frac{1}{2} DHI(1 + \cos\theta_t), \tag{4.20}$$

where DHI denotes the magnitude of the diffuse horizontal irradiance and θ_t denotes the tilt angle. This is the simplest of sky diffuse models and the foundation upon which other models are built. More complex models include effects such as horizon and circumsolar brightening but often use empirical lookup tables that add to the model's computational load and rely on additional parameters such as the angle of incidence and zenith angle. The simplicity of the isotropic model makes it much more suitable for a vehicle simulation.

This model is applied to each surface. By using the isotropic model, only pitch angle is needed to determine the diffuse radiation on each module. Knowledge of the bus heading or the sun's position in the sky is not necessary. The top panel is tilted only with respect to the pitch angle. The side panels each remain vertical for the entire experiment, as it is assumed that the roll angle is constant and equal to zero. The back panel is tilted by 90° to start, and is subject to additional

tilt based on the pitch angle. This shown in Figure 4.7 and described in Equations (4.21)–(4.24).

$$G_{d,top} = \frac{1}{2} DHI(1 + \cos\theta_p) \tag{4.21}$$

$$G_{d,right} = \frac{1}{2} DHI(1 + \cos 90^\circ) = \frac{1}{2} DHI \tag{4.22}$$

$$G_{d,left} = \frac{1}{2} DHI(1 + \cos 90^\circ) = \frac{1}{2} DHI \tag{4.23}$$

$$G_{d,back} = \frac{1}{2} DHI(1 + \cos(90^\circ + \theta_p)) = \frac{1}{2} DHI(1 - \sin\theta_p) \tag{4.24}$$

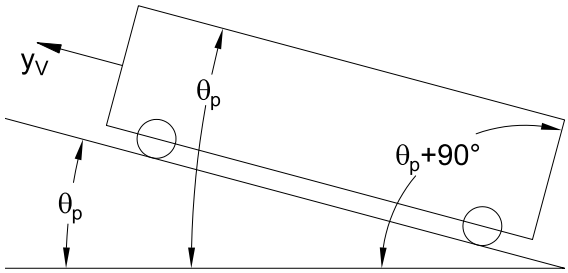

FIGURE 4.7. Tilt angle of rooftop and back PV modules.

4.2.5. Efficiency Modeling. Once the incident beam and diffuse radiations on each surface have been found, the total radiation on each surface is obtained by adding them together.

$$G_{t,i} = G_{b,i} + G_{d,i} \tag{4.25}$$

With the total radiation on each surface known, a model must be formed to relate the solar radiation to the electrical power extracted from each module.

The fundamental behavior of a PV cell can be modeled as a circuit with a current source, an ideal diode, and series and shunt resistances, as shown in Figure 4.8 [**113**]. However as will be discussed, an equivalent circuit model is more complex than necessary for this work; further details on the single diode model are widely available in the literature, such as Reference [**113**, **114**, **115**, **116**], and are not presented here.

Solving for the terminal voltage V_T and current I_{load} using the method described in [**116**] produces an I–V curve with a shape typified by Figure 4.9. For any given operating condition, PV modules have an ideal operating point, known as the maximum power point (MPP). The power, voltage, and current at the MPP can vary considerably with temperature and radiation. However, extensive literature exists showing how the MPP can be tracked in order to maximize PV

performance under variable conditions. Reference [**117**], for instance, reviews 19 distinct methods of MPP tracking that have been studied in academic literature.

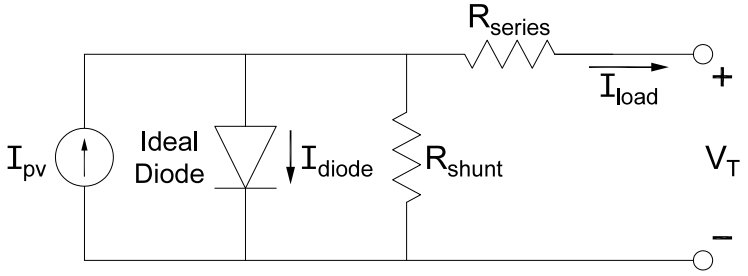

FIGURE 4.8. PV module equivalent circuit

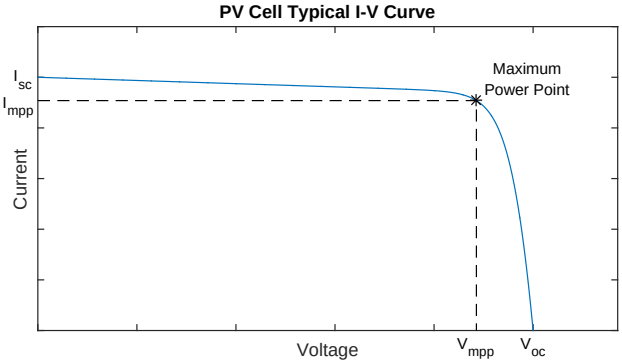

FIGURE 4.9. Typical PV module I–V curve.

In order to ensure as much solar energy as possible is utilized, it is assumed that the MPP is tracked on each PV module. Although this is a strong assumption given the difficulties in tracking the MPP for a system that may be partially shaded [**118**], the shading efficiency in Equation (4.19) is expected to encompass any losses from failing to track the MPP. The DC-DC converters described in Section 4.2.1 and shown for the rooftop module in Figure 4.2 are used to track the MPP of the top and side modules. By assuming the MPP is tracked accurately, it is only necessary to model the behavior of the peak power value rather than the behavior of the PV module as a whole. In this work, the temperature and radiation dependencies of the maximum power are considered.

It can be assumed that the peak power value varies linearly with temperature according to a peak power temperature coefficient, K_{mpp} [**109**]. K_{mpp} represents the fractional change in performance of the module as the actual cell operating temperature T deviates from the SRC temperature.

In this work, cell operating temperature is described by the thermal model presented in [**109**]. This thermal model estimates the operating temperature T from the current total radiation G_t and air temperature T_{air} as well as the nominal operating cell temperature $NOCT$ under a nominal thermal environment: radiation of 800 W/m^2 and ambient air temperature of 20°C.

$$T_i = T_{air} + \frac{G_{t,i}}{800\text{W/m}^2} \cdot (NOCT - 20°\text{C}) \tag{4.26}$$

It should be noted that while SRC represents standard lab conditions, the nominal thermal environment in [**109**] represents the conditions that the PV module is typically subjected to once installed outside. The ambient air temperature is acquired from TMY data. K_{mpp} is taken to be $-0.43\%/°\text{C}$ and $NOCT$ is taken to be 48°C , based on literature regarding mono-crystalline silicon PV cells [**119**], [**120**]. Manufacturer datasheets may provide this information as well.

The peak power value is modeled as varying linearly with radiation exposure. This is a first-order accurate model, per [**109**], and is seen by the authors as a suitable trade-off between complexity and accuracy. As discussed previously, the PV system is rated at test conditions of $G_{SRC} = 1000\text{W/m}^2$. So, the electrical power produced at T_{SRC} is given by the rated PV power times the ratio of the current total radiation and the SRC radiation.

The temperature effects described previously are then incorporated to form Equation (4.27), which describes the electrical power P_{pv} produced by a PV system subject to variations in temperature and radiation exposure.

$$P_{pv,i} = P_{rated,i} \cdot \frac{G_{t,i}}{G_{SRC}} \cdot (1 + K_{mpp}(T_i - T_{SRC})) \tag{4.27}$$

where $P_{rated,i}$ is from Equation (4.6) and $T_{SRC} = 25°$ as given in Subsection 4.2.2.

The shading factor in Equation (4.19) is expected to account for some potential losses like the MPP tracker finding a local (rather than global) optimal operating point. Additional sources of module inefficiency, such as soiling or degradation of the modules, are not considered in this study but will be the subject of future work.

4.3. Case Study

In this section, a case study is laid out to assess the impact of PV on the electrical energy consumption of the bus and the aging of the bus battery. The following subsections describe the

vehicle models, different bus configurations, the simulated geographic location, drive cycle, bus route, and time of operation examined in the case study. Because of the cost to implement and test the proposed system and the time needed to run the battery to the end of its life, simulation is used to assess the performance of OBPV on an electric bus.

4.3.1. Dynamic Model. This case study uses the vehicle model Section 2.1 using the parameters given in Tables 4.2. For this work, the vehicle mass M_v is determined from a base weight M_{bus}, the battery pack weight M_{batt}, and the weight of any PV panels M_{pv}.

$$M_v = M_{bus} + M_{pv} + M_{batt} \tag{4.28}$$

Battery weight is determined from the number of cells and the weight per cell. Weight per cell includes the weight of the battery management system, estimated from [**121**]:

$$M_{batt} = N_p N_s M_{cell} \tag{4.29}$$

PV weight was previously defined in Equation (4.7).

TABLE 4.2. Vehicle model parameters.

Parameter	**Variable**	**Value**
Bus Mass	M_{bus}	15,500 kg
Frontal Area	A_f	8.02 m^2
Aerodynamic Drag Coefficient	C_D	0.55
Rolling Resistance Coefficient	C_R	0.008
Wheel Inertia	J_w	20.52 kg-m^2
Motor Inertia	J_m	0.277 kg-m^2
Wheel Radius	R_w	0.48 m
Final Drive Ratio	N_{fd}	5.5:1
Gearbox Ratio	N_{gb}	5:1
Transmission Efficiency	η_{trans}	96%

The battery model uses the reduced-order equivalent circuit presented in Section 2.2 with parameters for the equivalent circuit from [**122**]. The battery characteristics are given in Table 4.3.

TABLE 4.3. Battery model parameters.

Parameter	Variable	Value
Open-Circuit Voltage per Cell	V_{cell}	2.0V to 3.4V
Rated Energy Capacity per Cell	E_{cell}	8Wh
Rated Charge Capacity per Cell	Q_{cell}	2.5Ah
Battery Cell Equivalent Resistance	R_{cell}	6 mΩ
Battery Cell in Series	N_s	110 sets
Series Sets in Parallel	N_p	385 cells
Battery Weight per Cell	M_{cell}	94 g

4.3.2. Battery Health Model. This research makes use of the cycle-counting aging model presented in Section 2.3.1, simplified by eliminating aging factors that are not expected to be significant in the experiment. It is assumed that the battery temperature is well-regulated by a battery management system, so the temperature effects of aging are not included in the aging model. Additionally, it will be shown in Section 4.4.3 that the average charge and discharge rates on the simulated bus are low, and the charge or discharge rates between bus configurations with and without solar power are mostly the same. The impact of large currents on aging are therefore assumed to be negligible as well. On the other hand, enough solar power is collected over the course a day of operation to impact the depth of discharge, so depth of discharge must be considered. Overall, an aging model that only considers depth of discharge is sufficient for this analysis.

This work uses the cycle life data [**123**] for the same battery used in the battery equivalent circuit model. The functional relationship between cycle life CL and depth of discharge DOD is logarithmic in nature [**82**] and is found by fitting a curve to the manufacturer data. The curve fit proposed in [**82**] and given in Equation (4.30) is found to provide the best fit to available data.

$$CL = \beta_0 \cdot DOD^{-\beta_1} \cdot \exp\left(\beta_2(1 - DOD)\right) \tag{4.30}$$

Using a least-squares regression, it is found that $\beta_0 = 2731.7$, $\beta_1 = 0.679$ and $\beta_2 = 1.614$ best fits the provided cycle life data. The curve fit results are shown in Figure 4.10.

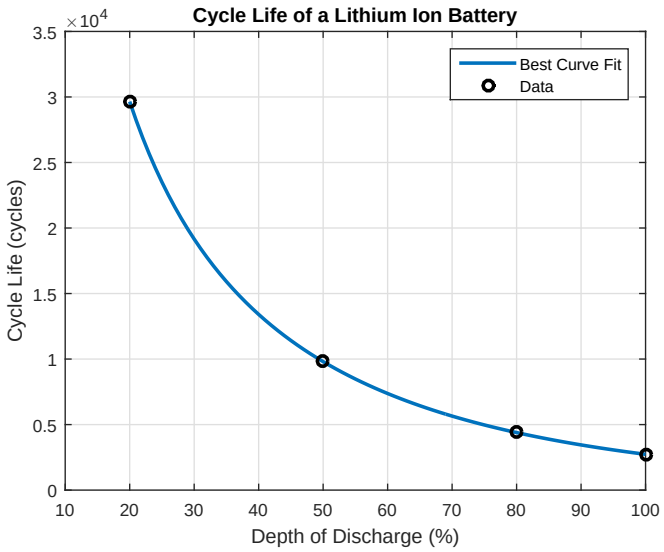

FIGURE 4.10. Depth of discharge versus cycle life of the lithium-ion battery.

4.3.3. Bus Configurations. As discussed in the Section 4.2, two different configurations of OBPV were simulated. One configuration, hereby referred to as the "Rooftop PV" configuration, has PV modules mounted to the roof of the bus only. The other configuration, hereby referred to as the "Full-Body PV" configuration, has PV modules mounted to both the roof, sides, and back of the bus. These configurations are listed in Table 4.4.

Simulation with these two configurations would reveal how integrated PV power can improve battery life and extend vehicle range. However, it is also true that battery cycle life and vehicle range could be extended by simply using a larger battery: with a larger battery, each individual cell experiences less throughput and the battery overall is not discharged as deeply. In order to assess how the benefits of integrated PV hold up against the benefits of increased battery capacity, two additional bus configurations are proposed.

The first additional configuration has no PV modules, but the battery pack has been enlarged to have a total energy capacity of 341.9kWh by adding an additional set of battery cells in series ($N_p = 385$, $N_s = 111$). This corresponds to adding batteries equal in weight to the weight of the rooftop PV module. This configuration is hereby referred to as the "Equal Weight" configuration.

The second additional configuration has no PV modules, but the battery pack has been enlarged to have a total energy capacity of 356.6kWh by adding 6 battery cells to each parallel set and by adding 4 additional battery sets in series ($N_p = 391$, $N_s = 114$). This corresponds to adding

batteries whose cost is approximately equal in to the cost of roof PV module. The cost of lithium-ion batteries and PV modules are estimated from industrial average prices [**124**], [**125**]. This configuration is hereby referred to as the "Equal Cost" configuration.

Simulation of these additional configurations allow the benefits of PV to be compared fairly to batteries. A nominal bus with no PV and with the original battery pack is simulated as well.

TABLE 4.4. Bus Configurations.

Configuration	**PV Modules**	**Battery Size**
Nominal	None	338.8 kWh
Rooftop PV	Top Only	338.8 kWh
Full-Body PV	Top, Sides, and Back	338.8 kWh
Equal Weight	None	341.9 kWh
Equal Cost	None	356.6 kWh

4.3.4. Simulation Location. The impact of OBPV on an electric bus depend on the local weather conditions and the geographic location of the bus's route. Clearer locations, locations closer to the equator, and locations with a higher elevation are exposed to more solar radiation, resulting in a greater impact on the vehicle's energy consumption. Additionally, the performance PV panels mounted on the side or back of the bus depend on the chosen route. For instance, side-mounted panels operating on a bus near the equator will collect more energy if the route is primarily in the north/south direction, perpendicular to the direction of travel of the sun and therefore exposed to more solar radiation.

This work considers a PV-augmented bus in Davis, California. Davis experiences hot, clear summers and cool, rainy winters. It is at roughly sea level and, at 38°33′14″N 121°44′17″W, is slightly south of the average latitude of the contiguous United States. The annual solar insolation on an optimally tilted plane in Davis is approximately 2,100 kWh/m^2 [**126**]. The TMY data for Sacramento International Airport (approximately 18km away from Davis) is used to estimate a full 365 days of weather [**127**].

4.3.5. Drive Cycle. The electric bus was simulated on the Orange County Transit Authority (OCTA) drive cycle [**128**]. This drive cycle was designed by West Virginia University from experimental data from the OCTA and represents a standard suburban bus velocity profile, but does

not correspond to any specific route. The velocity profile is shown in Figure 4.11. This cycle was repeated several times until the desired route length was reached.

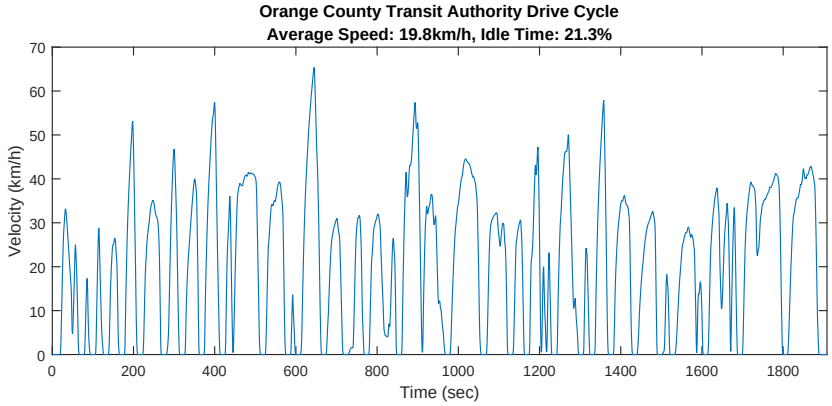

FIGURE 4.11. OCTA suburban bus drive cycle.

4.3.6. Route. The electric bus is set to follow the UC Davis Unitrans O-Route bus route, at a pace set by the OCTA drive cycle. Depicted in Figure 4.12, the route spends roughly equal time heading north, south, east, and west. The elevation was assumed to be constant; a reasonable assumption given that land grade in Davis is typically less than 1% and the difference between its highest and lowest points is approximately 10m [**129**]. This assumption means that there are no gravitational effects in the vehicle dynamics and that the angle of incidence for direct radiation on the rooftop panels does not vary with position along the route. However, the route choice still impacts the collection of PV energy from direct solar radiation on the side- and back-mounted panels.

In this case, the route functions essentially to ensure an realistic distribution of north, south, east, and west bus headings over the course of a day. It will be shown that direct radiation on the side panels makes up only about one quarter of the total PV energy on the Full-Body PV bus configuration; so, although the drive cycle does not correspond directly to the drive cycle, this discrepancy is expected to have minimal bearing on how the side PV panels are evaluated. With that said, applications on OBPV to hilly or even mountainous locations would need a drive cycle that matches the vehicle route to capture the effect of pitch angle changes and turns on both vehicle dynamics and PV collection [**130**].

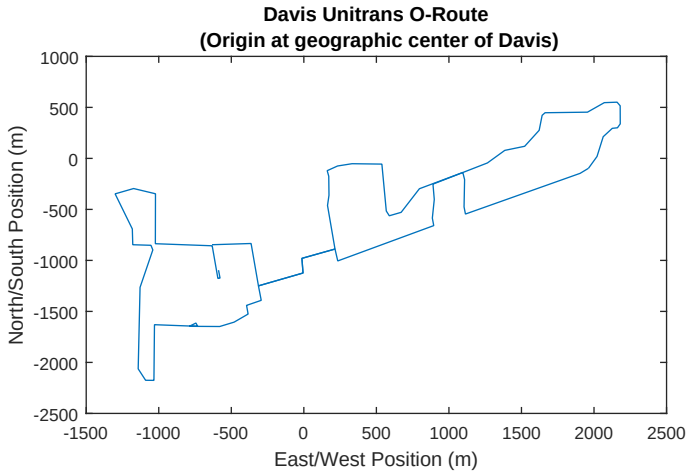

FIGURE 4.12. Davis Unitrans O-Route.

The degree of impact of OBPV was expected to vary with the usage patterns of the bus: different daily driving distances have different depths of discharge, resulting in different aging of the battery. In order to fully evaluate the impact of OBPV, each configuration of the bus was simulated for daily driving distances ranging from 120km to 200km. On the OCTA drive cycle, this corresponds to daily driving durations of 6 hours to 10 hours. The longest daily route length, 200km, corresponds to the furthest the nominal bus can drive using a battery with 20% capacity fade.

4.3.7. Simulation Timespan. The simulated bus begins its route each day at 7:00 am. Repeated simulations were carried out to find the battery cycle life for each configuration operating and daily driving distance. In the case of the Rooftop PV and Full-Body PV configurations, the daily weather conditions from TMY data was use chronologically. The repeated simulations were also used to measure the electrical energy collected by the PV modules on each day of the typical meteorological year.

4.4. Results and Analysis

The results of the case study are organized as follows: First, the range extension provided by the electric bus is estimated. Next, the results are used to measure the amount of electrical energy that was collected per year from an OBPV system, compared to the annual consumption of electric

energy by the bus. Third, the results are used to determine the impact of OBPV on battery aging, as compared to other methods of increasing battery life.

4.4.1. Range Extension. During the experiment, the nominal bus configuration used 129.6 kWh/100km on average. The Rooftop PV configuration also used 129.8 kWh/100km while the Full-Body PV configuration used 130.2 kWh/100km, the Equal Weight configuration used 129.8 kWh/100km, and the Equal Cost configuration used 130.8 kWh/100km. However, the Rooftop PV and Full-Body PV configurations met the bus power request using both battery stored energy and power from the PV modules. The battery stored energy consumed per 100km was 123.8 kWh/100km on average for the Rooftop PV configuration and 118.9 kWh/100km on average for the Full-Body PV configuration, although these values varied with the amount of usable sunlight. Figure 4.13 shows the consumption of battery stored energy per 100km for each configuration as it varied by month.

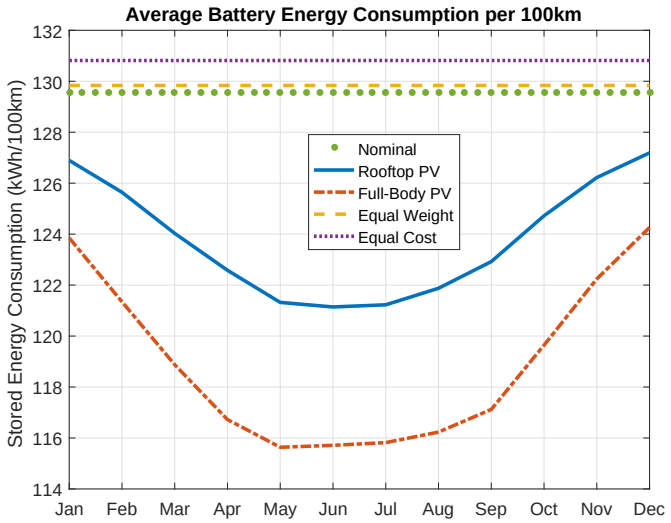

FIGURE 4.13. Simulated bus energy usage per configuration and time of year

Using these data, the range extension provided by either PV configuration compared to the nominal bus was estimated. Results are presented as additional range per 100km driven by the nominal bus. On an average day, rooftop PV could extend driving range on by 4.7km per 100km driven, while PV modules on the roof and sides could extend driving range by 8.9km per 100km driven. However, the amount of solar energy collected daily varied considerably with time of year and weather conditions — the rooftop PV could provide as little as 1.5kWh or as much as 19.2kWh

of electrical energy, while a bus with both roof and side modules could get as little as 3.0kWh or as much as 33.4kWh. In the worst case (an overcast winter day), rooftop PV could extended range by only 0.3km per 100km driven, while PV modules on the roof and sides could extend range by 0.6km per 100km driven. On the other hand, in best-case conditions (a clear summer day) range could be extended by 7.6km per 100km driven for rooftop PV and by 13.4km per 100km driven for roof and side PV. A histogram of the range extension provided by OBPV is shown in Figure 4.14. The implementation of OBPV had clear potential to extend vehicle driving range, as on the majority of days the bus range can be extended by several kilometers. However, the minimal energy collected in the worst-case weather conditions and the number of days were OBPV provides only a negligible increase in range indicate that OBPV was not a robust means to extend range every day of the year. The inclusion of side-mounted PV panels helps mitigate this somewhat, but still has some days with negligible range extension.

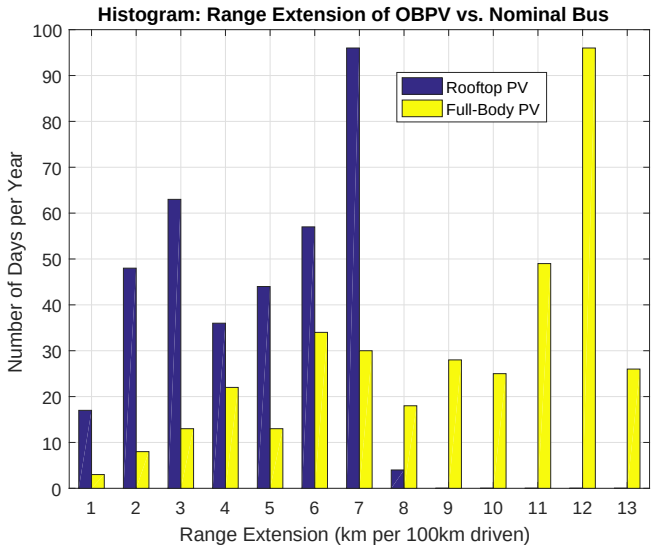

FIGURE 4.14. Histogram of range extension provided by OBPV.

4.4.2. PV Energy. The intensities of solar radiation reaching the bus roof and bus sides were compared in terms of daily irradiance and monthly insolation. Figure 4.15(a) shows the simulated radiation that reaches the bus on a fairly typical day. The side PV modules experienced more variation than the roof PV modules due to the changing bus orientation and also experienced a decrease in radiation during midday, when the sun was close to directly overhead. The side modules experienced less radiation in general because they could not always be exposed to direct

radiation. However, near sunrise and sunset when the sun was low in the sky, sunlight reached the side modules at a more direct angle, such that the side modules experienced more radiation than the roof module. Figure 4.15(b) shows the total solar insolation that reached the panels each month. In Figure 4.15(b) the total radiation on the side modules is found by taking a weighted average of the total radiation on the right, left, and back modules:

$$G_{t,sides} = \frac{G_{t,right}A_{pv,right} + G_{t,left}A_{pv,left} + G_{t,back}A_{pv,back}}{A_{pv,right} + A_{pv,left} + A_{pv,back}}. \tag{4.31}$$

The insolation is found by integrating the radiation with respect to time. Because the bus traveled north, south, east, and west roughly equally, the insolations on the right, left, and back PV modules were approximately equal to each other regardless of time of year.

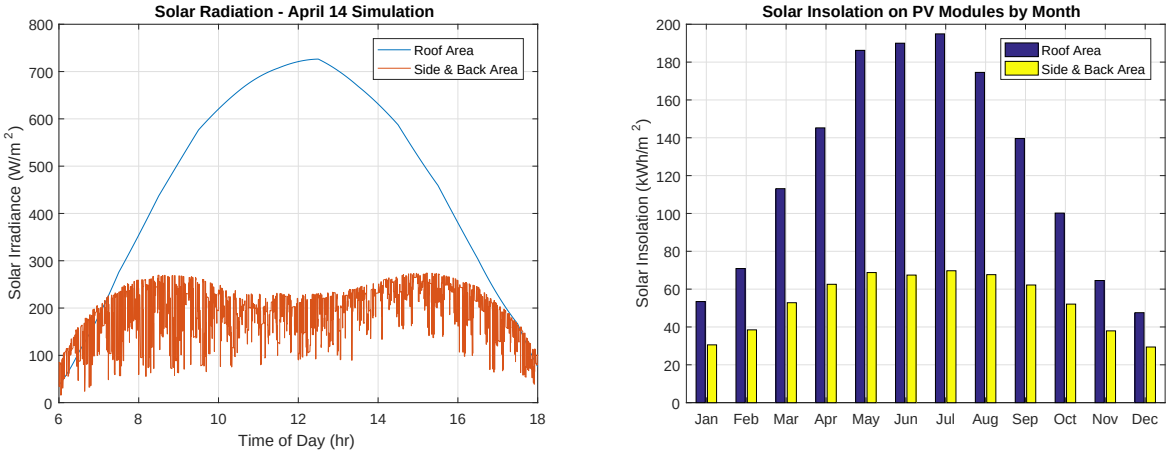

(a) (b)

FIGURE 4.15. Intensities of solar radiation reaching the bus **(a)** on a typical clear day; **(b)** over the course of each month.

The sun is lower in the sky in winter months compared to summer months, so solar radiation approached the side modules at a more direct angle. Also, greater cloud cover in the winter months meant that the diffuse radiation made up a larger portion of the total radiation. This resulted in less discrepancy between the rooftop PV modules and side PV modules during winter months compared to summer months. The total yearly solar insolation was 1,480 kWh/m^2 on the roof module and 640 kWh/m^2 on the side modules. Over the course of a year, approximately 38.3% of the collected PV power on the rooftop panels comes from indirect radiation, and the rest from

direct radiation. Side panels are more reliant on indirect radiation, with approximately 45.5% of coming from indirect radiation.

Assuming the PV modules could continue to collect energy and charge the battery while the bus was not in operation (such as parked at a depot), the roof-mounted panels collected a total of 4,560 kWh of electrical energy over one year, while the side-mounted panels collected a total of 4,321 kWh of energy. Figure 4.16 shows the electrical energy from PV modules by month. The electrical energy is found by integrating Equation (4.27), where the solar radiation and ambient temperature for each day of the year are obtained from the NREL's TMY data [**127**]. Because the side modules covered a larger area than the rooftop modules, they produced a comparable amount of electrical energy to the rooftop modules despite their lower annual insolation.

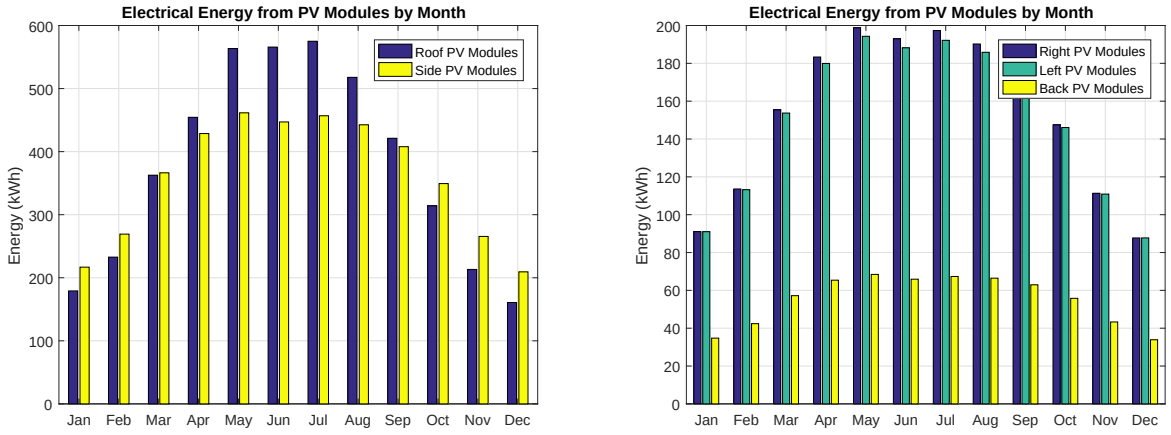

(a) (b)

FIGURE 4.16. Monthly electric energy collected from **(a)** roof and side PV modules; **(b)** right, left, and back PV modules.

Using the fuel economy results presented earlier, one can estimate the portion of the annual electrical energy consumption of the bus that the PV modules can provide for various daily route lengths. For instance, if a bus is driven 150km each day, rooftop PV modules could provide up to 6.4% of the electrical energy, while modules on the roof and sides could together provide up to 12.5%. The relation between this percentage and the average daily driving distance is illustrated in Figure 4.17.

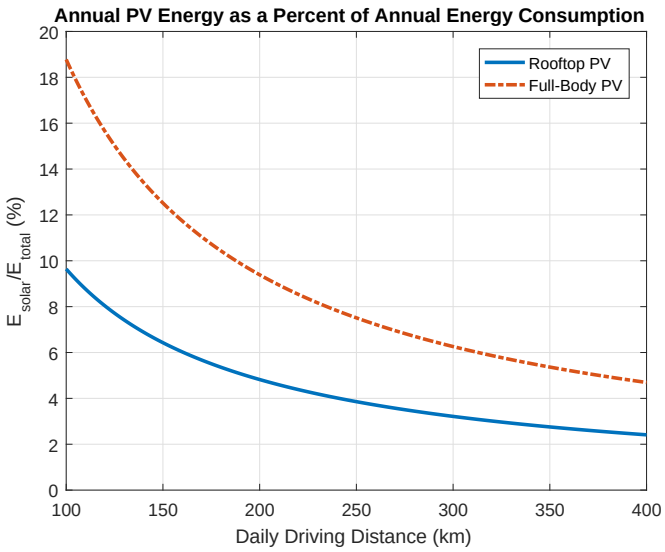

FIGURE 4.17. PV contribution towards total annual energy consumption.

An interesting finding was that although the side-mounted PV panels provided less power in summer months, they provided as much or more power than the rooftop PV modules during the winter months. This was because in winter months, the earth is tilted away from the sun, resulting in the radiation having a more direct path to the side modules than in summer months. Although the side PV modules were less efficient on a per-area basis, they reduced the variability in daily energy collected between summer and winter months.

The payback time can be computed for the top and side PV modules using the commercial off-peak cost of energy in Davis, \$0.23 per kWh [**131**]. Using the industrial average price per watt of solar panels, it is estimated that the rooftop module would cost \$6,247, while the side modules would cost \$13,139 [**125**]. Then, the rooftop panels are expected have a payback time of 6 years, while the side panels are expected to have a payback time of 13 years and 3 months. These payback times are longer than the amount estimated in [**44**] and [**52**] due to the lower price of electric energy compared to diesel fuel. For payback times of this length, it is questionable whether a manufacturer would want to go ahead with PV integration. However, these payback times do not account for any incentives that local government might offer for solar installation, nor do they account for the value added from extending the battery cycle life, which will be discussed in 4.4.3.

4.4.3. Battery Aging. Repeated simulations were carried out for each configuration to find the battery cycle life associated with each configuration and route duration. In this section, one

"cycle" refers to one day of driving. The nominal, Equal Weight, and Equal Cost configurations did not have any weather-dependent parameters, so the only variation from one simulation to the next was the maximum battery capacity. On the other hand, the Rooftop PV and Full-Body PV configurations had weather conditions that changed daily in addition to the changing maximum battery capacity. These experiments were carried out using chronological TMY data.

Before proceeding to the battery aging results, some of the aging modeling assumptions are verified. The battery aging model assumed that the charge and discharge rates, as well as the difference in charge and discharge rates between configurations, would be small enough that the aging model would only need to consider the depth-of-discharge per cycle. It was observed from the results that the average absolute C-rate for the nominal bus was 0.169C, while it was 0.166C for the Rooftop PV configuration and 0.165C for the Full-Body configuration. These rates are low and near the 0.5C C-rate of the test data in [**123**]. Additionally, the maximum discharging C-rates were 0.777C, 0.768C, and 0.764C, respectively, while the maximum charging C-rates were 0.968C, 0.977C, and 0.992C. Because the C-rates were low and near the C-rate of the empirical cycle life data, and because the differences in C-rate between the configurations were minimal, the assumption that charge and discharge rates could be neglected from the aging model was considered valid.

Figure 4.18 shows the aging of the five different configurations for a 160km daily bus route. The battery for the nominal configuration aged the fastest, reaching its end-of-life after approximately 6,000 charge-and-discharge cycles—or rather, approximately 6,000 days of driving. The Full-Body PV configuration aged the slowest, followed by Rooftop PV and then the two extra-battery configuration. For each configuration, as the maximum storage capacity of the battery decreased with each day of driving, it was discharged to greater depths which in turn caused each cycle to do more damage.

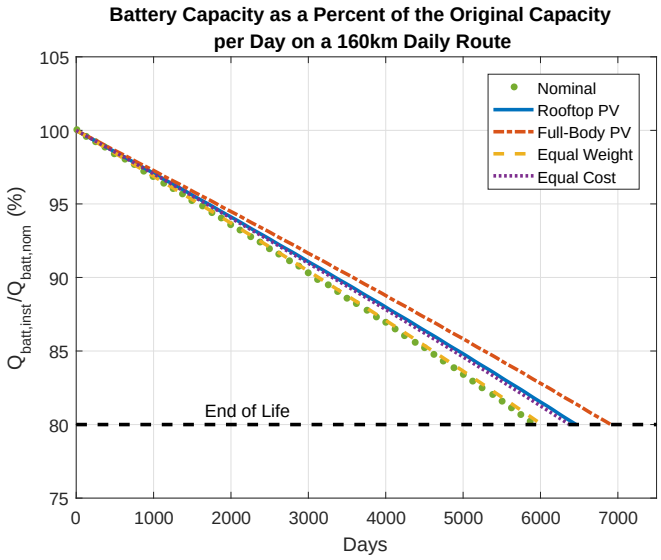

FIGURE 4.18. Battery capacity fade on the 160km bus route.

Figure 4.19(a) shows the cycle life for each configuration as it varies with route length, while Figure 4.19(b) shows the increase in cycle life of each configuration over the nominal configuration at each route length. Although the marginal cycle life for each configuration increased with decreasing route length, the percentage increase in cycle life was greater for longer routes. The Full-Body PV configuration increased the battery cycle life the most, followed by the Rooftop PV, then the Equal Cost, and finally the Equal Weight configuration.

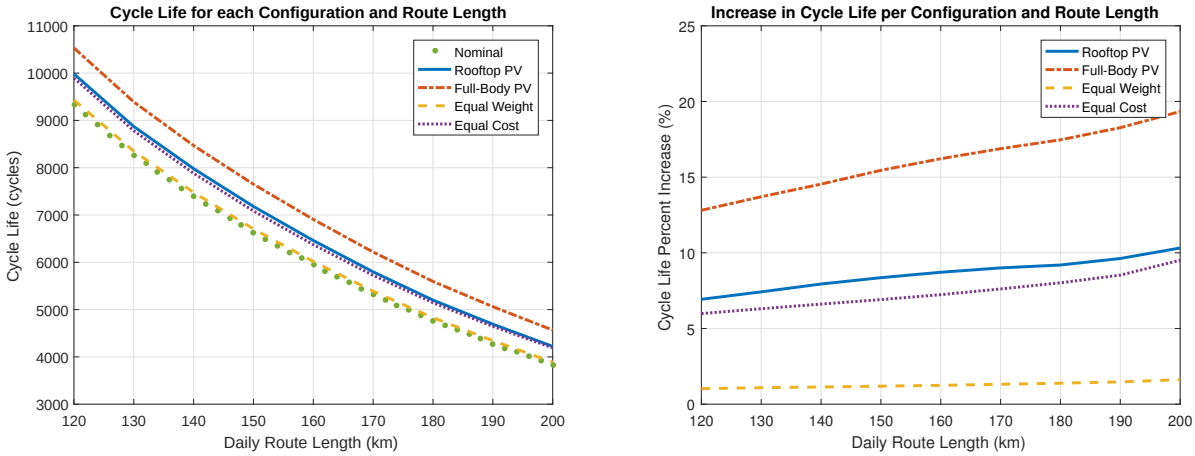

(a) (b)

FIGURE 4.19. **(a)** Battery cycle life; **(b)** increase in battery cycle per configuration.

TABLE 4.5. Marginal Mass and Cost of Bus Configurations.

Configuration	Marginal Mass	Marginal Cost
Rooftop PV	37.6 kg	$6,247
Full-Body PV	116.6 kg	$19,386
Equal Weight	36.2 kg	$1,220
Equal Cost	209.3 kg	$6,227

Increased cycle life on its own is not necessarily a good metric for each configuration's performance. Each configuration would have different drawbacks, such as added mass, size, or installation cost. The additional benefits of each configuration should therefore be compared to the additional penalty incurred by implementing that configuration.

This work first considers the marginal mass of each configuration. If the added PV modules or battery cells add too much weight, it might require the manufacturer to redesign other components of the bus or reduce the allowable number of passengers. The marginal mass of each configuration is summarized in Table 4.5.

Additionally, each configuration was looked at in terms of the effort required to implement that configuration. "Effort to implement" might include cost to install each configuration, ongoing maintenance costs, or additional hardware, such as a larger battery management system. This work considers the estimated marginal cost of the configuration, in terms of the industrial average price per watt of PV panels and price per kilowatt-hour of lithium-ion batteries, to be a reasonable proxy variable for "effort to implement". The price per kilowatt-hour for lithium-ion batteries is provided by [**124**], while the price per watt of PV systems is from [**125**]. The marginal cost of each configuration is summarized in Table 4.5.

Figure 4.20(a) shows the marginal increase in cycle life per marginal increase in mass for each configuration and route length. Although the Full-Body PV configuration yielded the most additional cycles, the Rooftop PV configuration was a more effective use of mass. In general, adding PV modules to the bus was a more effective use of weight than increasing battery size.

Figure 4.20(b) shows the marginal increase in cycle life per marginal increase in cost for each configuration and route length. Due to the low amount of radiation that the side modules experienced, the Full-Body PV configuration was the most inefficient use of funds. Although the Equal Weight configuration added the fewest cycles, its marginal increase in cycle life was achieved at very

little expense. Both added-battery configurations outperformed the Full-Body PV configuration, but the Rooftop PV configuration was clearly the most cost-effective.

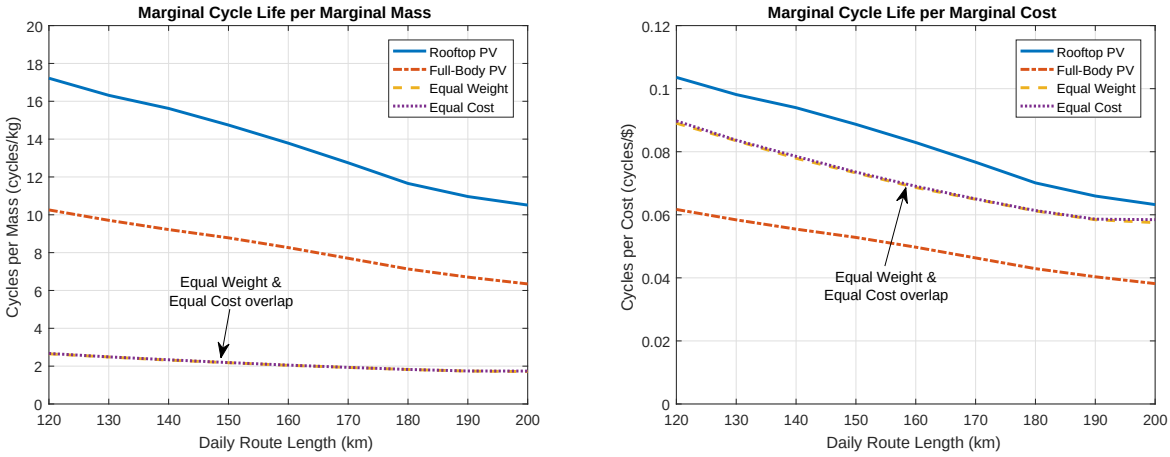

(a) (b)

FIGURE 4.20. Marginal cycle life **(a)** per marginal mass; **(b)** per marginal cost.

These relationships are visualized with the radar charts shown in Figure 4.21(a)–(d). It should be noted that these plots use the inverse of marginal cost and marginal mass so that a large value corresponds to a desirable trait: large "per cost" indicates an inexpensive option, while large "per mass" indicates a low-weight option. The axes of these plots are scaled so that the largest marginal cycle life, inverse marginal cost, and inverse marginal mass across the four cases are all the same distance from the origin. Although the Rooftop PV and Equal Cost configurations had the same initial cost, the Rooftop PV configuration provided moderately longer cycle life and was a much more effective use of weight. The Full-Body PV provided the largest extension to battery life, but was neither as cost or weight effective as PV modules on the bus roof only. The Equal Weight configuration was both low-cost and low-weight, but provided little in the way of additional battery lifespan. Overall, the Rooftop PV configuration offered the best balance of extending battery cycle life while keeping weight and cost low.

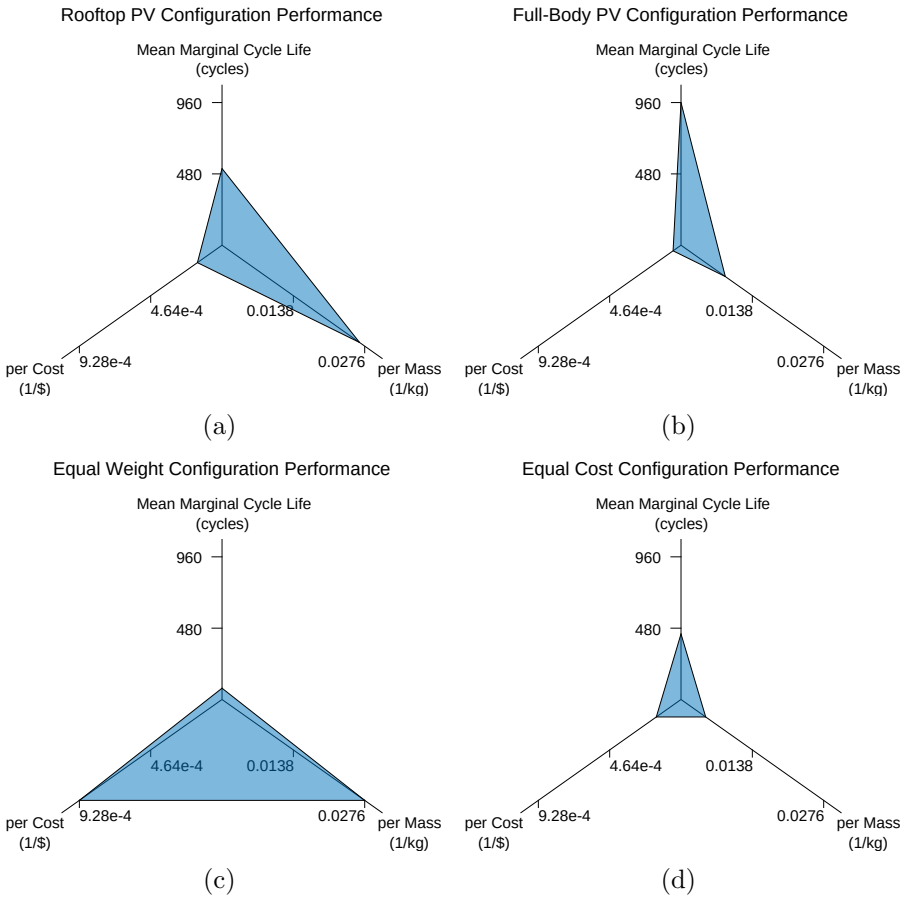

FIGURE 4.21. Radar plots of the performance metrics for **(a)** Rooftop PV, **(b)** Full-Body PV, **(c)** Equal Weight, and **(d)** Equal Cost.

Alternatively, one could define a non-dimensional cost or reward function to compare the four configurations with a single metric. For example, Equation (4.32) is a reward function that increases with larger cycle life improvements and decreases with larger costs at rates defined by the weighting parameters $B_{\Delta CL}$, $B_{\Delta M}$, and $B_{\Delta Cost}$, where ΔCL is the average marginal cycle life, ΔM is the marginal mass, and $\Delta Cost$ is the marginal cost.

$$R(\Delta CL, \Delta M, \Delta Cost) = B_{\Delta CL}\Delta CL - B_{\Delta M}\Delta M - B_{\Delta Cost}\Delta Cost \tag{4.32}$$

One could select $B_{\Delta CL} = 2$, $B_{\Delta M} = 4.59$, and $B_{\Delta Cost} = 0.0495$, which normalizes the three variables so that among the four configurations, the reward due to the maximum mean marginal cycle life is equal to the combined penalty of the maximum marginal mass and maximum marginal cost. The resulting reward/penalty of each configuration for this function and weighting are shown

in Figure 4.22. Once again, the Rooftop PV configuration strikes the best balance between added cycle life and added cost and weight. The higher weight lower marginal cycle life of the larger-battery configurations result in a net penalty rather than reward, indicating that OBPV is a better choice to extend battery lifespan. Of course, these results are heavily dependent on the choice of reward function.

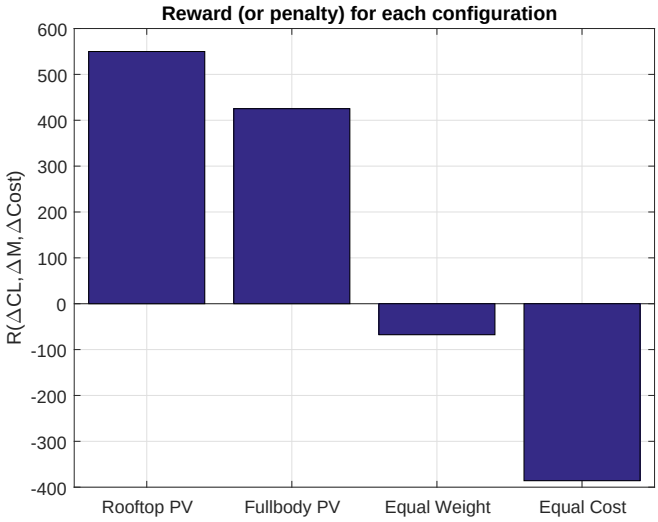

FIGURE 4.22. Evaluation of each configuration using a reward function.

A final metric for assessing the value of each configuration is the return on investment from increased in cycle life. The nominal configuration was estimated to cost $118,580. Then, the cost per cycle of the nominal configuration can be estimated by dividing the estimated cost by the nominal configuration cycle life CL_{nom}.

$$\text{Cost per Cycle} = \frac{\$118,580}{CL_{nom}} \tag{4.33}$$

The value of the cycles added by each configuration can then be found by multiplying the nominal cost per cycle by the marginal cycle life ΔCL of a given configuration.

$$\text{Cycle Life Value} = \frac{\$118,580}{CL_{nom}} \times \Delta CL \tag{4.34}$$

The net profit or loss is found by subtracting the marginal cost $\Delta Cost$ of a given configuration.

$$\text{Net Profit/Loss} = \frac{\$118,580}{CL_{nom}} \times \Delta CL - \Delta Cost \tag{4.35}$$

Return on investment (ROI) is then found by normalizing by the marginal cost of that same configuration and expressing the result as a percent.

$$ROI = 100\% \times \left(\frac{\$118,580}{CL_{nom}} \times \Delta CL - \Delta Cost \right) \times \frac{1}{\Delta Cost} \tag{4.36}$$

Here, $ROI = 0\%$ indicates the break-even point, while $ROI = 100\%$ indicates that the value of the added cycle life is twice the estimated cost of the configuration.

The ROI for each configuration and daily driving distance are shown in Figure 4.23. For all configurations, the ROI is greater with longer daily driving distances—or rather, for routes where the battery is discharged to a greater depth. The Rooftop PV configuration is seen to provide a positive ROI for all route lengths, while the Full-Body PV configuration is a net loss until the daily driving distance reaches 160km. The added-battery configurations are beneficial, but not to the extent of the Rooftop PV configuration.

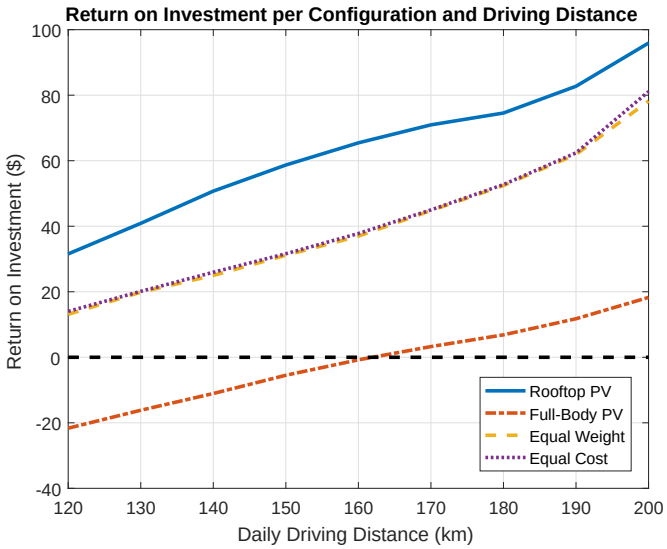

FIGURE 4.23. Return on investment of OBPV and increased battery size.

4.5. Conclusion

This work proposed modifying an electric bus to have OBPV power generation. PV modules mounted on both the vehicle roof and vehicle sides were considered. A modeling framework of an electric bus was developed so that the impact of the OBPV could be assessed for different locations, bus routes, and bus componentry. In particular, a method was developed to model the

solar irradiance on a moving surface. Daily operation of an electric bus on a suburban bus route in Davis, CA was simulated as a case study.

The results of the numerical experiment showed that on average, the collected power could extend range by approximately 4.7km per 100km driven with rooftop panels and 8.9km per 100km driven with rooftop and side panels. However, high variance in the daily power collected meant that OBPV were not a robust means of range extension.

The PV modules could supply up to 8,881 kWh of energy annually when mounted on both roof and side of the bus, or up to 4,560 kWh of energy annually when mounted on the roof only. Although the side modules occupied approximately twice the area of the rooftop module, over the course of a year they produced 5% less energy than the roof modules, indicating that side-mounted modules were not as effective but could still prove beneficial after all rooftop area has been exploited. The payback time for the roof-mounted panels was estimated to be 6 years, while the payback time of the side-mounted panels was estimated to be 13 years and 3 months. However, this payback time did not consider the value added by increasing battery cycle life.

The results were also used to assess the impact of OBPV on battery lifespan. For constant vehicle range, rooftop PV modules could extend battery cycle life by up to 10%, while PV modules on both the roof and sides could extend it by up to 19%. Rooftop PV modules were shown to be both a more weight-effective and cost-effective means of increasing battery cycle life than expanding the size of the battery. Adding PV modules to both the roof and sides of the bus extended battery life the most and was more weight-effective than increasing battery size, but was the least cost-effective method. The additional lifespan added by the rooftop PV was a positive return on investment, while the return on investment for a system with modules on both the roof and sides was negative unless the battery was discharged deeply each day.

CHAPTER 5

Aging-Aware Control for Electric Vehicles with Hybrid Energy Storage

In the previous chapter, we identified that EVs with very larger batteries did not have large currents as a significant aging factor, and so we used on-board photovoltaics to reduce battery discharge depth as a way to reduce aging. Now, we begin looking at cases with smaller batteries where large currents are a factor in battery aging. To start, this chapter investigates the control of a lithium-ion battery and ultracapacitor hybrid energy storage system (HESS) for an electric vehicle. It begins by discussing the purpose of hybrid energy storage and current research into HESS control. A new approach to HESS control is proposed: incorporating ultracapacitor aging into the energy management strategy. Then, a case study compares this new approach to existing methods. The chapter concludes by analyzing the case study results in terms of battery lifespan improvements and the overall cost/benefit of the HESS and by discussing the improvements related to active control of ultracapacitor aging compared existing methods, as well as general discussion of the efficacy of different types of HESS control.

5.1. Introduction

Electric vehicles that frequently stop and start—such as transit buses—may experience accelerated battery degradation due to large spikes in current related to braking and accelerating. One possible solution to this is to use a Hybrid Energy Storage System (HESS)—a combination of lithium ion energy storage with an ultracapacitor (UC) sized to handle large charge and discharge currents—in place of standard battery energy storage. In general, lithium ion batteries have a high energy density but low power density: they can storage a lot of charge, but cannot access it quickly without degrading. Specifically, large currents to and from the battery cause its capacity to fade and internal resistance to grow. High temperatures and deep discharges also contribute to battery aging. On the contrary, ultracapacitors have a low energy density and high power density [**6**]. A HESS, then, lets on obtain the efficient storage of lithium batteries while allowing an ultracapacitor

to handle the large currents [**6**, **33**]. Aging of UCs does not depend on current magnitude or discharge depth, rather on time, temperature, and cell voltage [**53**,**54**,**55**], so there is not necessarily a direct tradeoff between battery aging and UC aging in a HESS (although large currents do increase temperature, so there can be an indirect link). However, UCs operate more efficiently at higher cell voltages [**63**], so there can be a tradeoff between UC efficiency and UC aging.

Current research on HESS's considers HEV, EV, and fuel cell vehicle applications. The bulk of literature, for instance [**63**, **68**, **132**, **133**, **134**, **135**], is concerned with optimal sizing of the HESS so as to maximum the cost-effectiveness of such a system. However, battery aging is often not considered directly in this optimization; instead, battery aging factors like high temperatures and currents are minimized, rather than battery aging directly, and the improvements to overall aging are only assumed [**135**]. Some related work that does directly address aging is described here. In reference [**58**], for instance, an optimal control policy is developed to control UC behavior. This policy demonstrated clear aging improvements over a uncontrolled system using passive energy management. Reference [**59**] used multi-objective optimization while directly incorporating an aging model and using a rule-based control system to govern energy management for a study on HESS sizing in EVs. Reference [**60**] likewise carries out a parametric study on battery degradation versus UC size in EVs, using a control system based on fuzzy logic. Reference [**61**] considered a HESS that used lead-acid batteries rather than lithium ion, and developed an HEV energy management strategy that tuned for battery life extension. Notably, they found that for the HESS to be cost-effective, a 50% increase in battery cycle life was required. Reference [**62**] compared the aging benefits to an optimally-sized HESS to the theoretical maximum benefits—battery aging reductions with an infinitely large HESS. These benefits were experimentally verified, with the developed approach decreasing battery power fade and temperature rise in lithium-ion batteries on a vehicle load profile. Most notably, references [**65**,**66**,**67**] demonstrate an optimal control strategy to directly minimize battery aging in a HESS for a plug-in HEV. [**63**] can be considered the state-of-the-art, applying deterministic DP to jointly optimize for battery aging and energy losses in an electric bus.

However, the literature is lacking on the impact of ultracapacitor aging in the HESS and how this in turn affects the economic benefit of the HESS—for instance, [**63**] assumes a 1% degradation rate per year of the UC, rather than directly modeling and assessing the UC aging. Given that

UC aging and UC efficiency may be inversely correlated, this research proposes a new energy management strategy to jointly control battery aging, ultracapacitor aging, and energy losses. The benefit to this method is twofold: The primary benefit of including UC aging costs is to ensure that the HESS operates in a way that will not excessively degrade the ultracapacitor. A less apparent benefit, however, is that including the UC aging dynamics gives the controller a refined understanding of the electrical losses in the UC due to growth of the internal resistances. In the next sections of this chapter, this new strategy is developed and compared to existing methods in terms of both lifespan increase to the battery and the economic cost/benefit analysis of a HESS.

5.2. Ultracapacitor Aging Modeling

Reference [**53**] provides a model for ultracapacitor aging that is based on Eyring's Law, a chemical rate equation, which gives an ultracapacitor lifespan T_{life} based on the operating voltage and internal temperature where aging increases exponentially as the voltage and temperature increase. This experimental fitting is in line with other recent literature on ultracapacitor aging [**136**, **137**, **138**]. As [**53**] develops their model with dynamic simulation in mind, it is the most appropriate model for control applications. First, the lifespan of the ultracapacitor is given by

$$T_{life} = T_{life}^{ref} \times \exp\left(\ln(2)\frac{\theta_c^{ref} - \theta_c}{\theta_0}\right) \times \left(\exp\left(\ln(2)\frac{V^{ref} - V}{V_0}\right) + K\right) \tag{5.1}$$

where θ_c is the UC temperature, V is the UC voltage, and the remaining variables (T_{life}^{ref}, θ_c^{ref}, θ_0, V^{ref}, V_0, and K) are experimentally fitted parameters. Then, the aging rate at an instance in time is based on the inverse of the lifespan at the given operating conditions.

$$\frac{dSoA}{dt}(V, \theta_c) = \frac{1}{T_{life}(V, \theta_c)} \tag{5.2}$$

In this model, SoA is the state of aging that characterizes both capacitance fade and resistance growth, where $SoA = 0$ indicates start-of-life and $SoA = 1$ indicates end-of-life.

Reference [**53**] then finds that the instantaneous capacitance C and internal resistance R are given by

$$C = C_0 \times (0.95 - 0.15 \cdot SoA) \tag{5.3}$$

$$R = R_0 \times (1 - 0.3 \cdot SoA)^{-1} \tag{5.4}$$

where C_0 and R_0 are the initial values of C and R.

Reference [**53**] defines the UC end-of-life condition as similar to batteries: when the capacitance of the UC has faded by 20%. A thermal model for the UC is not included in this work; instead the UC pack is assumed to operate at a constant internal temperature of 55°C, estimated from the operating conditions found in [**139**].

This model is ready to be used for control as-is: aging-aware controllers can penalize the aging rate from 5.2 to reduce UC degradation. Typically, HESS controllers must include UC voltage as a state variable to enforce minimum/maximum voltage constraints. So, a basic understanding of UC aging can be added to the HESS EMS without any increase in the number of controller states. A more refined implementation, however, requires including a state-of-aging state variable to handle the capacitance fade and resistance growth over time.

5.3. Control

This research makes use of the dynamic programming framework developed in Chapter 3. In this research, DDP is used to obtain the global-optimal control strategy for a given cost function and represents the best-case scenario for a controller type. SDP on the other hand represents a causal, implementable controller and offers a more realistic understanding of the capabilities of a given cost function design.

In order to fully investigate the benefits of aging-aware control, four different types of energy management systems are considered:

(1) Minimizing the equivalent cost of the HESS but *excluding* the cost of UC aging, denoted EC for "equivalent cost".

(2) Minimizing the equivalent cost of the HESS and accounting for the cost UC aging, denoted ECX for "equivalent cost extended".

(3) Minimizing a combination of power to/from the battery and deviation of the ultracapitor state-of-charge from a setpoint, denoted PC for "power control".

(4) Load-leveling, a simple online method used to constrain large battery currents and denoted LL.

These methods are described below, followed by the constraints applied to the control systems.

5.3.1. Equivalent Cost. This strategy minimizes the combined cost of battery degradation and electrical energy losses from the battery and ultracapacitor according to the instantaneous cost function

$$L(x, u, w) = Cost_{batt}\Delta D + Cost_{elec}E_{loss} \tag{5.5}$$

where ΔD is the damage to the battery as a result of a given control decision, as given in Equation (2.66) and where E_{loss} is the energy losses from the battery and ultracapacitor, obtained from

$$E_{loss} = R_{s,pack}I^2_{batt,pack} + R_{uc,pack}I^2_{uc,pack} + P_{uc,conv\text{-}loss} \tag{5.6}$$

where, per the control-oriented models developed in Sections 2.2, $R_{s,pack}$ is the battery pack series resistance, $I_{batt,pack}$ is the total current through the battery, $R_{uc,pack}$ is the ultracapacitor pack series resistance, $I_{uc,pack}$ is the total current through the ultracapacitor pack, and $P_{uc,conv-loss}$ are losses due to DC-DC conversion of the UC power as given in Equation (2.53). Returning to Equation (5.5), the $Cost_{batt}$ and $Cost_{elec}$ terms are the price of the battery pack in USD and the price of electrical energy in USD/kWh, respectively.

The state variables needed for this approach are the ultracapacitor state of charge SOC_c, the battery depth of discharge for the current cycle DoD, and the accumulated battery damage D_{tot}. The controlled variable is the power allotted to ultracapacitor P_{uc}. The driver power demand P_{dem} is an input to the controller. For DDP, it is a precisely known function of time, while for SDP the future power demand is estimated from the current driver power demand and the current vehicle wheel speed ω_{wh}, based on a stochastic model as described in Section 3.2.

It should be noted at this point that DP provides an optimal control solution *on the assumption* that the model used to generate the optimal control matches the system to which the resulting controller is applied. Differences between the real system and the system modeled for control development can cause the DP method to return poor results. In this case, our "real" system includes ultracapacitor aging dynamics that the DP control is unaware of. If the affects of ultracapacitor aging are significant, we can expect the DP results for this controller type to be poor.

5.3.2. Equivalent Cost Extended. The newly proposed method from this research incorporates the cost of ultracapacitor aging into the DP instantaneous cost function.

$$L(x, u, w) = Cost_{batt}\Delta D + Cost_{elec}E_{loss} + Cost_{UC}\Delta SoA \tag{5.7}$$

where $Cost_{UC}$ is the price of the ultracapacitor pack in USD and ΔSoA is the change in the ultracapacitor's state of aging per Equation (5.2) resulting from some control decision. The remaining terms are the same as in Equations (5.5) and (5.6).

This approach uses the same controlled variables and inputs as the EC method, and includes the three state variable from the EC method. In theory, an additional UC state of aging state variable could be introduced to allow the increased electrical losses due to UC resistance growth to be incorporated into the optimization process, improving accuracy of the controller. This work does not simulate over the entire lifespan of the UC however and as will be shown in Section 5.5, when UC aging is controlled the aging rate is small enough to not require inclusion in the optimal control.

5.3.3. Power Control. The third and final strategy does not directly penalize aging but rather penalizes large power going to or from the battery

$$L(x, u, w) = (SOC_c - SOC_{c,tgt})^2 + Q_P P_{Batt}^2 \tag{5.8}$$

where Q_P is a tuned weighting parameter and P_{batt} is the power going to or from the battery per Equation (2.13). In this way, we are limiting battery and UC damage using only simple knowledge of how the energy storage components age: large currents degrade the battery and high operating voltages degrade the UC. Thus, we can distinguish the benefits of direct aging control in the EC and ECX strategies from the benefits of DP control generally. Additionally, the SOC_c deviation penalty helps maintain the UC's readiness to handle large currents. If the UC is near it's maximum charge, it may be unable to accept a large charging power demand, or conversely if it is near its minimum, it will be unable to provide a large discharging power demand.

This strategy does not incorporate any aging models, so only the SOC_c variable is required as a state variable. $SOC_{c,tgt}$ is set to the midpoint of the minimum and maximum SOC_c values, 75%. The DoD and D_{tot} state variables needed in the EC and ECX controllers can be ignored. The inputs and controlled variables are the same as for the EC and ECX controllers, however.

5.3.4. Load-Leveling. The final strategy considered is a simple method called "Load-Leveling". In this method, the battery is assigned a maximum allowable current for charging and discharging, $I_{b,max}$, which corresponds to minimum and maximum battery powers $P_{b,min}$ and $P_{b,max}$. $P_{b,min}$

provide the limit on power going into the battery while charging (negative values of P_{batt}) and $P_{b,max}$ provides the limit on discharging. Any power demand from the driver that exceeds the allowable amount is handled by the ultracapacitor.

$$P_{uc} = \begin{cases} P_{dem} - P_{b,max}, & P_{dem} > P_{b,max} \\ P_{dem} - P_{b,min}, & P_{dem} < P_{b,min} \\ P_{reset}, & \text{otherwise} \end{cases} \tag{5.9}$$

where P_{reset} is a small amount of power to or from the battery used to return the ultracapacitor SOC to a target value of $SOC_{c,tgt} = 75\%$.

$$P_{reset} = \begin{cases} 13kW, & SOC_c > SOC_{c,tgt} \\ -13kW, & SOC_c < SOC_{c,tgt} \\ 0 & \text{otherwise} \end{cases} \tag{5.10}$$

The 13kW value corresponds approximately to a 0.1C battery charge or discharge rate, considered sufficiently low to not majorly affect the battery aging. The particular value of $I_{b,max}$ is varied to tune the response of the controller.

This controller servers as a lower bound and useful benchmark for EMS performance, as it has neither an aging model nor any form of optimal control.

5.3.5. Constraints. Finally, there are several constraints that are applied to all controllers. First, the UC power per cell is limited to

$$-62.5\text{W} \leq P_{uc} \leq P_{uc,max} \tag{5.11}$$

where the minimum is based on a 25A limit per cell, in line with UC manufacturer specifications [**81**] and where the maximum is based on the same 25A limit and on a power limit obtained from the discriminant of Equation (2.46).

$$P_{uc,max} = \min\left(62.5\text{W}, \ \frac{q_c^2}{4R_{uc}C_{uc}^2}\right) \tag{5.12}$$

Notably, this means the UC discharging power is more tightly constrained at low amounts of charge. Next, SOC_c is constrained to

$$50\% \leq SOC_c \leq 100\% \tag{5.13}$$

where the lower bound of 50% ensures that the UC operates in a high-efficiency region and avoids an overly constrained $P_{uc,max}$, and is in line with the method proposed in [**63**].

5.4. Case Study

A case study is proposed to test and compare the energy management strategies presented in Section 5.3. This case study uses the vehicle, battery, and ultracapacitor models developed in Chapter 2 using the parameters given in Tables 5.1–5.3. The simulation uses the 4th-order UC and 2nd-order battery models while the control uses the simple 1st-order UC and quasi-static battery models. Both simulation and control use the cycle-counting method, considering discharge depth, charging current magnitude, and discharging current magnitude as aging factors, while constant temperature is assumed. Each strategy developed in Section 5.3 simulated on four hours of driving on the Manhattan Bus Cycle (MBC) drive cycle [**140**] for three HESS different designs: a small ultracapacitor unit $N_{pc} = 10$, a middle-sized ultracapacitor unit $N_{pc} = 40$, and a large ultracapacitor unit $N_{pc} = 100$.

TABLE 5.1. Vehicle model physical parameters.

Parameter	**Variable**	**Value**
Vehicle Mass	M_v	18,181 kg
Frontal Area	A_f	8.02 m^2
Drag Coefficient	C_D	0.55
Roll Resistance Coefficient	C_R	0.008
Wheel Inertia	J_w	20.52 kg-m^2
Motor Inertia	J_m	0.277 kg-m^2
Wheel Radius	R_w	0.48 m
Final Drive Ratio	N_{fd}	5.1:1
Gearbox Ratio	N_{gb}	5:1
Transmission Efficiency	η_{trans}	96%

TABLE 5.2. Battery model parameters.

Parameter	Variable	Value
Battery Cells in Series	N_{ser}	100 cells
Battery Series Sets in Parallel	N_{par}	160 sets
Total Charge Capacity	$Q_{batt,pack}$	368Ah
Nominal Open Circuit Voltage	$V_{ocv,pack}$	330v
Nominal Equivalent Resistance	$R_{s,pack}$	5.5 mΩ

TABLE 5.3. Ultracapacitor model parameters.

Parameter	Variable	Value
UC Modules in Series	N_{sc}	100 modules
UC Series Sets in Parallel	N_{pc}	10, 40, or 100
Resistance	$R_{uc,pack}$	44.3m$\Omega \times N_{sc}/N_{pc}$
Capacitance	$C_{uc,pack}$	105.9F $\times N_{pc}/N_{sc}$

The EC and ECX methods are simulated for both DDP (to find the global optimum) and SDP (to find an obtainable optimum). The PC and LL benchmark cases are simulated for an array of controller tunings. The load leveling controller has the $I_{b,max}$ parameter varied from 2C to 0.8C. The PC controlled type uses the SDP method with the Q_P parameter varied from 10^{-14} to 10^{-11}. This range of weights is determined by looking at orders of magnitude of the element of the PC cost function: the $(SOC_c - SOC_{c,tgt})^2$ term has an order of magnitude of at most 10^{-2}, while the P_{batt}^2 term can have an order of magnitude of up to 10^{10}. Thus, tuning of Q_P begins at $Q_P = 10^{-12}$ and is varied to larger and smaller values from that point. Additionally, a single baseline case that does not use the ultracapacitor is simulated. In this case, the EV battery is subjected to the large discharging currents from accelerating after a stop and the large charging currents ue to regenerative braking without the buffer provided by the UC.

Simulations begin with both the battery and ultracapacitor at the beginning of their life. Each driving period starts with the battery charged to $SOC_b = 98\%$. After each full discharge cycle, the aging of the battery and ultracapacitor are measured, and the capacity, capacitances, and resistances of the HESS are updated. For the purpose of measuring aging, the battery is assumed

to recharge at a rate of 0.5C. Simulations are then repeated until the battery reaches the end of its life, at which point the cycle life, ultracapacitor state-of-aging, and average energy consumption are measured from the simulation and recorded.

The battery aging is measured as with total distance that must be driven to reach battery end-of-life. For ease of interpretation, this distance-based lifespan is converted to an approximate time-based lifespan, years to battery end-of-life, using an estimate of the average number of miles driven per year, $D_{avg\text{-}year} = 34,000$ [**141**]. Energy consumption is likewise measured in kWh per km, but for ease of interpretation is converted to MPGe. This is for two reasons: First, it lets all measurements under consideration—lifespan, energy consumption, UC aging, and economic benefit per mile (to be defined shortly)—follow the same pattern of larger values being better and lower values being worse, which makes it easier to interpret and compare results. Second, MPGe is considered a more common unit of vehicle energy consumption in the US. Ultracapacitor aging is measured at the battery's end of life and normalized to aging per year.

Finally, the cost-benefit of the HESS is determined. First, the value of the HESS is determined based on industrial average price per kWh of \$300/kWH for lithium ion batteries and \$15000/kWh ultracapacitors from [**142**] and from the battery and ultracapacitor size given earlier in this section. This gives a battery value of $Val_{batt} = \$36{,}432$ and ultracapacitor values for the $N_{pc} = 10$, $N_{pc} = 40$, and $N_{pc} = 100$ cases of $Val_{uc,10} = \$1{,}302$, $Val_{uc,40} = \$5{,}208$, and $Val_{uc,100} = \$13{,}021$, respectively. Additionally, an average electrical energy price of $Val_{nrg} = \$0.1065$/kWh for the U.S. is obtained from [**143**].

Costs and benefits are normalized by mile driven for a fair comparison between configurations. Then, the battery cost per mile (BCPM) is determined from the miles driven over the life of the battery, denoted "battery lifetime miles driven" (BLMD).

$$BCPM = \frac{Val_{batt}}{BLMD} \tag{5.14}$$

The ultracapacitor cost per mile (UCCPM) is similarly determined, this time including a term for the ultracapacitor state of aging at the battery end-of-life (BEOL), SoA_{BEOL}.

$$UCCPM = SoA_{BEOL} \times \frac{Val_{uc}}{BLMD} \tag{5.15}$$

In this way, the ultracapacitor's cost is distributed across it's lifespan, rather than as a lump cost at the start of the vehicle's life. Finally, the energy costs per mile (ECPM) are given as

$$ECPM = \frac{Val_{nrg} \times GGE}{MPGe} \tag{5.16}$$

where GGE is the gasoline gallon equivalent to convert from gallons of gasoline to kWh, $GGE =$ 33.41kWh/gal. gasoline. Alternatively, the conversion from energy to GGE could be skipped by using the original kWh per km measurement. Then,

$$ECPM = 1.609 \times Val_{nrg} \times (\text{kWh per km}) \tag{5.17}$$

Then, the cost or benefit of the HESS can be determined by comparing to the nominal case where no UC is present. Letting the subscript *nom* denote the nominal case and (k) denote any particular simulation, the benefit per mile (BPM) is given by

$$BPM(k) = (BCPM_{nom} - BCPM(k)) - UCCPM(k) + (ECPM_{nom} - ECPM(k)) \tag{5.18}$$

where a positive benefit per mile indicates that value is being added to the system, while a negative value indicates that the cost of the UC outweighs the benefit it adds.

Finally, the payback time $T_{payback}$ (in years) for the HESS can be estimated from the UC value, average miles driver per year, and the benefit per mile.

$$T_{payback} = Val_{uc} \times \frac{1}{BPM(k)} \times \frac{1}{D_{avg\text{-}year}} \tag{5.19}$$

Payback time assumes a positive benefit per mile. If the BPM is zero or negative, then a payback time does not exist.

5.5. Results

The simulation results are analyzed as follows: First, the battery and capacitor states-of-charge are plotted to verify controller behavior. Next, the equivalent cost strategies are compared for both SDP and DDP to demonstrate the impact of ultracapacitor control. Following this, the aging-aware controllers are compared to the two benchmark cases. Finally, the sensitivity of the HESS cost-benefit is analyzed and discussed.

5.5.1. Time Response. This subsection compares the time response of the DDP-EC and DDP-ECX controllers for the $N_{pc} = 100$ case. Although the other cases (smaller UC sizes and SDP controllers) are not shown here, the same trends are observed between the EC and ECX controllers for these cases.

First, Figure 5.1 shows the battery SOC after four hours of driving on the Manhattan Bus Cycle for both a new battery and after 3750 charge-discharge cycles, which is near the end of the battery's lifespan. Only the final 15 minutes of these simulations are plotted, so that the differences between the controller types are more distinct. Again, this confirms prior expectations about the controller behaviors. For new batteries, we see the final SOC_b to be higher for the nominal case than for either the DDP-EC or DDP-ECX examples. This is expected due to the additional energy losses incurred from the ultracapacitor internal resistance. After 3750 cycles, we see that the capacity has faded such that the final SOC_b on all three cases has decreased. We also see that the nominal vehicle simulation's battery has aged the most; its final SOC_b after 3750 cycles has dropped by 18.8% versus at the battery's start-of-life. This is compared to a 14.5% drop with the DDP-EC controller and a 14.8% drop with the DDP-ECX controller. Additionally, these SOC plots let us observe the mechanism by which the controllers reduce battery aging: the SOC_b trajectory for the nominal vehicle battery is filled with "microcycles"—rapid changes of the battery current direction between charging and discharging [**144**]—which are tamped out by the DDP-EC and DDP-ECX controllers.

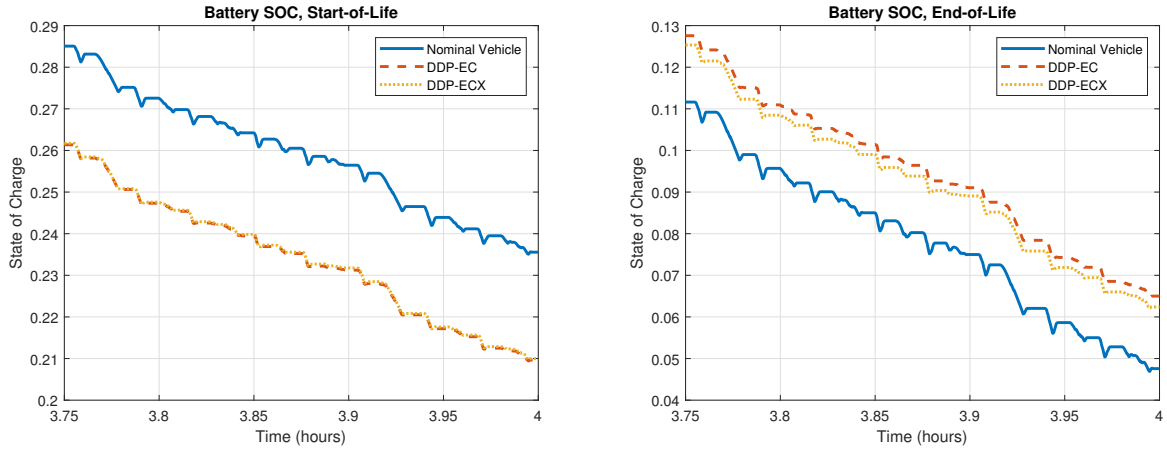

(a) (b)

FIGURE 5.1. SOC_b trajectory at (a) battery start-of-life and (b) after 3750 cycles, near battery end-of-life.

Next, the ultracapacitor state of charge is shown for a representative window of time in Figure 5.2. This plot shows both SOC_c for both DDP-EC and DDP-ECX controllers at the battery's beginning of life and after it has aged after 3750 cycles. From Section 5.2, we know that high operating voltage (and therefore high SOC_c) degrades the UC. This figure, then, clearly shows the benefit of UC aging control. The DDP-EC method is seen to consistently operate at a higher voltage than the DDP-ECX method, degrading the UC and affecting the long-term performance of the HESS. Overall, the DDP-EC controller was found to operate and an average SOC_c of 71.6% over the lifespan of the battery, compared to an average of 60.5% for the DDP-ECX controller.

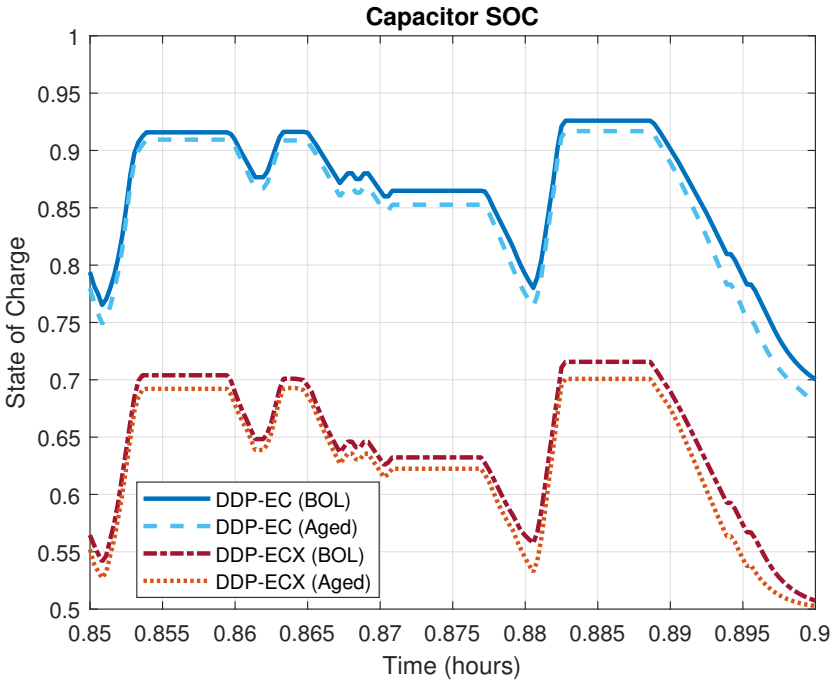

FIGURE 5.2. Comparison of DDP-EC and DDP-ECX capacitor SOC trajectories at battery BOL and approximate EOL.

Finally, the ultracapacitor usages for DDP-EC and DDP-ECX are plotted in Figure 5.3 alongside the driver's power demand over for the driving period between the simulation start and the first vehicle stop. These results confirm previous observations: Compared to DDP-EC, the DDP-ECX places more emphasis on discharing the UC and less on charging it, resulting in the lower operating SOC_c seen in Figure 5.2. This segment is representative of comparative ultracapacitor usage throughout the simulation.

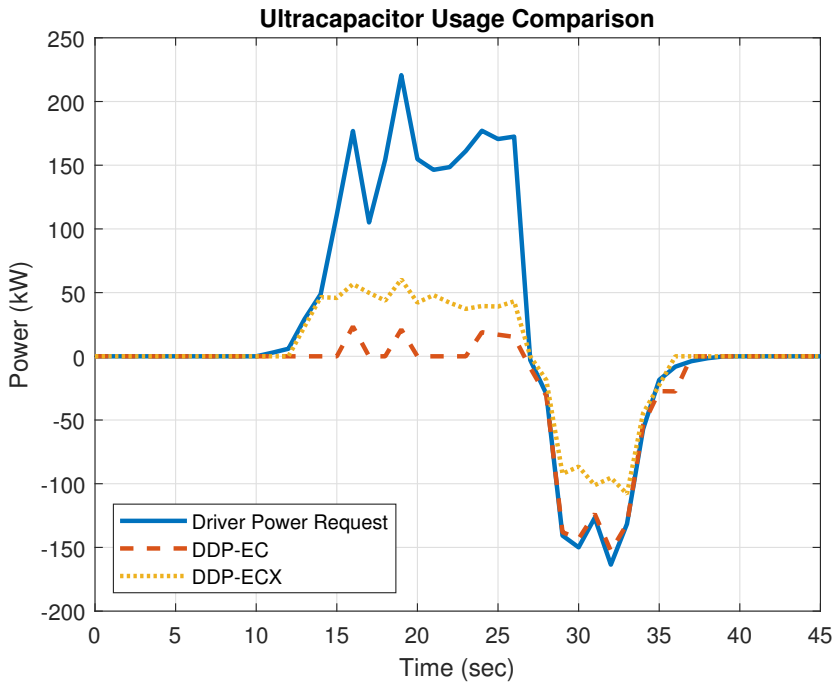

FIGURE 5.3. Comparison of ultacapacitor power usage on the MBC through the first stop.

5.5.2. Equivalent Cost Controllers. Next, the fuel economy, battery lifespan, and economic benefit of the DDP results for each case are compared. The DDP results are plotted in Figure 5.4(a)–(c) and summarized in Table 5.4. First, we see in Figure 5.4(a) that the EC method offers a greater increase in battery lifespan than the ECX method across all ultracapacitor sizes. Across the three UC sizings, the EC battery lifespan is on average 22% higher than ECX relative to the nominal lifespan.

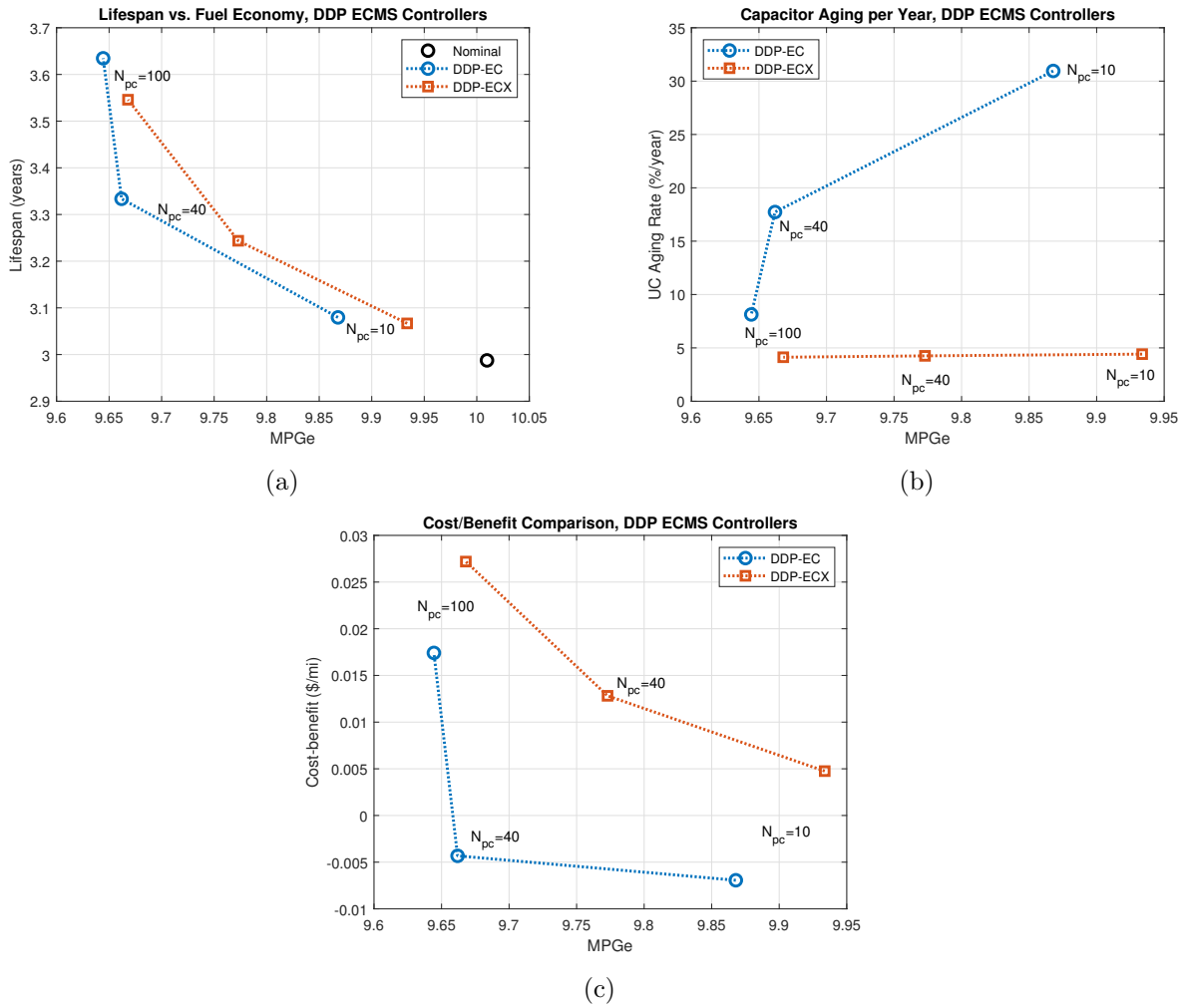

FIGURE 5.4. Energy consumption and (a) battery aging, (b) ultracapacitor aging, and (c) cost/benefit for the EC and ECX strategies using DDP.

However, Figure 5.4(b) shows that this improved battery lifespan comes at the cost of excessive ultracapacitor aging—the EC controllers are seen to age the UC at 2 to 6 times the rate of the ECX controllers. In the $N_{pc} = 10$ case, the UC ages at nearly the same rate as the battery and would require replacement every 3.2 years. The ECX strategies, on the other hand, maintain a slow aging rate of on average 4.3% per year across all UC sizings.

Figure 5.4(c) shows the net result of this trade-off: even though the EC strategy increased lifespan more than the ECX strategy, the extreme UC aging results in worse overall economics. In the best case ($N_{pc} = 100$), the EC controller produces a positive return on investment, but the ECX outperforms it by 56%. In the other cases, the HESS is a net financial loss compared

to a battery-only system. On the other hand, accounting for UC aging in the control strategy reduces the aging rate to a more reasonable level. At approximately 4.3%/year, the UC would only need to be replaced roughly every 23 years. In terms of UC sizing, the larger UC packs allow for greater increases in battery lifespan and a greater overall benefit per mile, however increased UC cost means that the payback time increases with larger UCs as well.

TABLE 5.4. Comparison of Equivalent Cost Controllers with DDP.

UC Size (N_{pc})	**Type**	**Lifespan (Years)**	**MPGe**	**UC Aging (%/Year)**	**BPM ($/mi)**	**Payback Time (Years)**
N/A	Nominal	2.99	10.01	–	–	–
10	EC	3.08	9.87	30.95	-0.0069	N/A
	ECX	3.07	9.93	4.41	0.0048	8.5
40	EC	3.33	9.66	17.73	-0.0043	N/A
	ECX	3.24	9.77	4.25	0.0128	12.7
100	EC	3.63	9.64	8.13	0.0174	23.3
	ECX	3.54	9.67	4.12	0.0272	14.9

Next, the SDP results are reviewed and compared both to each other and to the DDP results. The SDP results are plotted in Figure 5.5(a)–(c) and summarized in Table 5.5. In terms of battery lifespan, all cases perform roughly as expected: The EC controllers increase battery life to a greater degree than the ECX controllers. The SDP controllers improve battery lifespan, but not as much as DDP.

Interestingly, the SDP-EC method does not age the UC as much as the DDP-EC method. Because the SDP approach views the future driver behavior as uncertain, it has the UC spend less time near its maximum voltage limit so that it is able to accept a large charging current if necessary. Indirectly, this results in lower UC aging compared to the DDP-EC approach, even though the aging was not accounted for in this control strategy. Despite this, the ECX still outperforms the EC approach in terms of UC aging and overall cost-benefit.

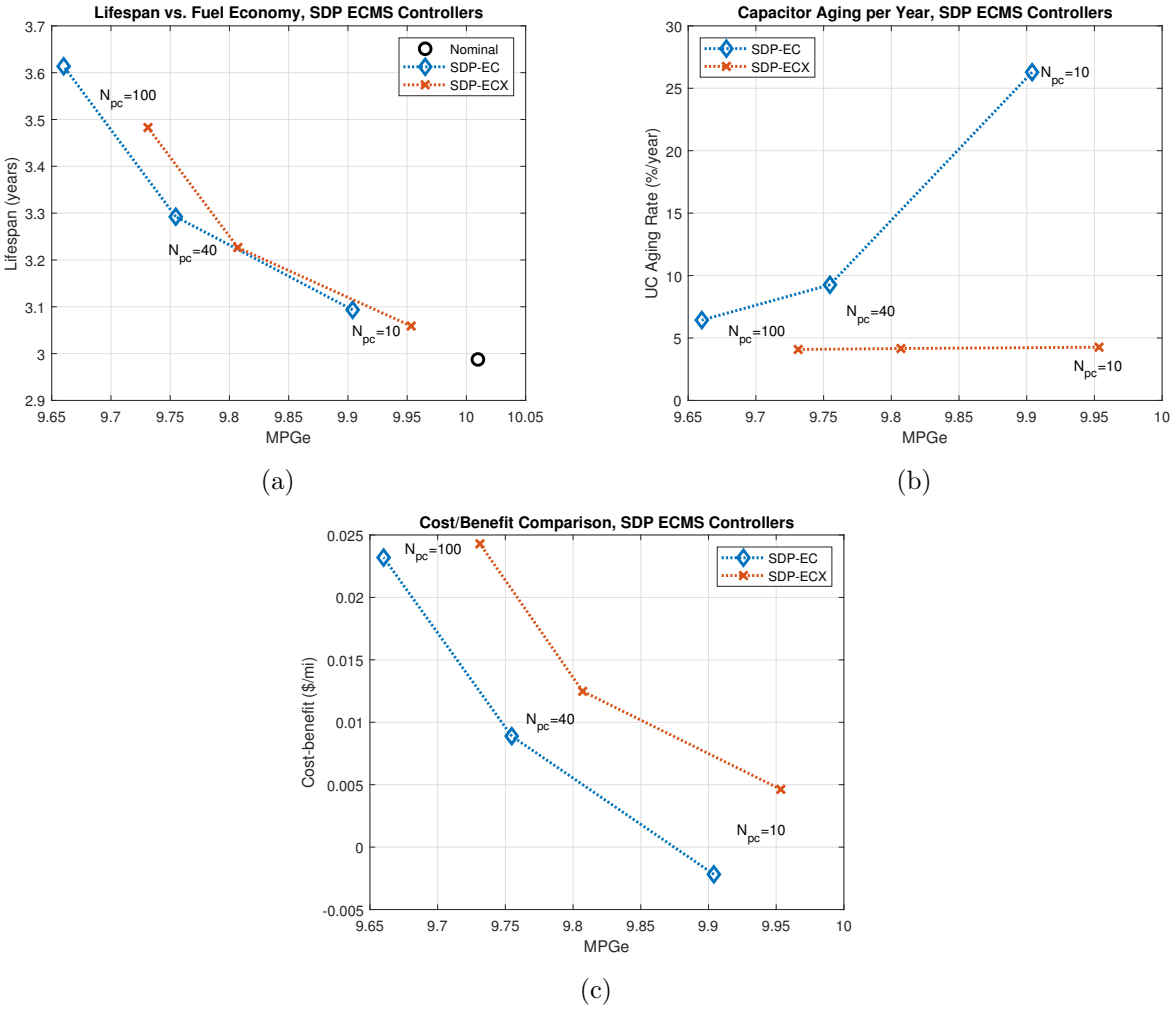

FIGURE 5.5. Energy consumption and (a) battery aging, (b) ultracapacitor aging, and (c) cost/benefit for the EC and ECX strategies using SDP.

TABLE 5.5. Comparison of Equivalent Cost Controllers with SDP.

UC Size (N_{pc})	**Type**	**Lifespan (Years)**	**MPGe**	**UC Aging (%/Year)**	**CPM ($/mi)**	**Payback Time (Years)**
N/A	Nominal	2.99	10.01	–	–	–
10	EC	3.09	9.90	26.29	-0.0022	N/A
	ECX	3.06	9.95	4.26	0.0046	8.8
40	EC	3.29	9.75	9.26	0.0089	18.2
	ECX	3.23	9.81	4.16	0.0125	13.0
100	EC	3.61	9.66	6.43	0.0232	17.5
	ECX	3.48	9.73	4.08	0.0243	16.7

5.5.3. Effect of Aging-Aware and Optimal Control. Next, all four causal strategies (SDP-EC, SDP-ECX, SDP-PC, and Load Leveling) are compared in terms of both battery lifespan increase and overall cost-benefit. The $N_{pc} = 10$ case is shown in Figure 5.6, the $N_{pc} = 40$ case is shown in Figure 5.7, and the $N_{pc} = 100$ case is shown in Figure 5.8.

Again, it can be seen that a larger HESS allows for greater improvements to battery lifespan. This is expected—the $N_{pc} = 10$ case only reduce current to or from the battery by approximately 0.5C, while the largest power demand from the driver corresponds to about 2.5C. On the other hand, the $N_{pc} = 100$ case can handle much larger power demands and can do much more to limit large battery current. However, these additional improvements come with a monetary cost, and the payback time increases as the UC size increases.

It is found across all three HESS sizing cases that the aging-aware controllers do the most to improve battery lifespan. Although the SDP-PC does improve lifespan in all 3 sizings and does exceed the performance of load-leveling (the non-SDP strategy), it does not improve lifespan as well as the SDP strategies that include direct aging control and economically it is a net loss as the value of the added battery lifespan does not overcome the cost of the UC and additional energy consumption. With that said, the simple methods of limiting UC aging—applying a quadratic cost to SOC_c deviations for SDP-PC, or having a small amount of power return the UC to a target charge when not in use for Load Leveling—is shown to be sufficient to limit battery aging. For all three UC sizings, the UC aging for the SDP-PC and LL methods are on par with the UC aging of

the SDP-ECX method. However, maintaining UC lifespan is not useful without extending battery lifespan, and these two methods do not "understand" the battery aging mechanics sufficiently to make them worthwhile strategies. The performance of SDP-ECX strategy relative to SDP-PC and LL clearly indicates the power of aging-aware energy management.

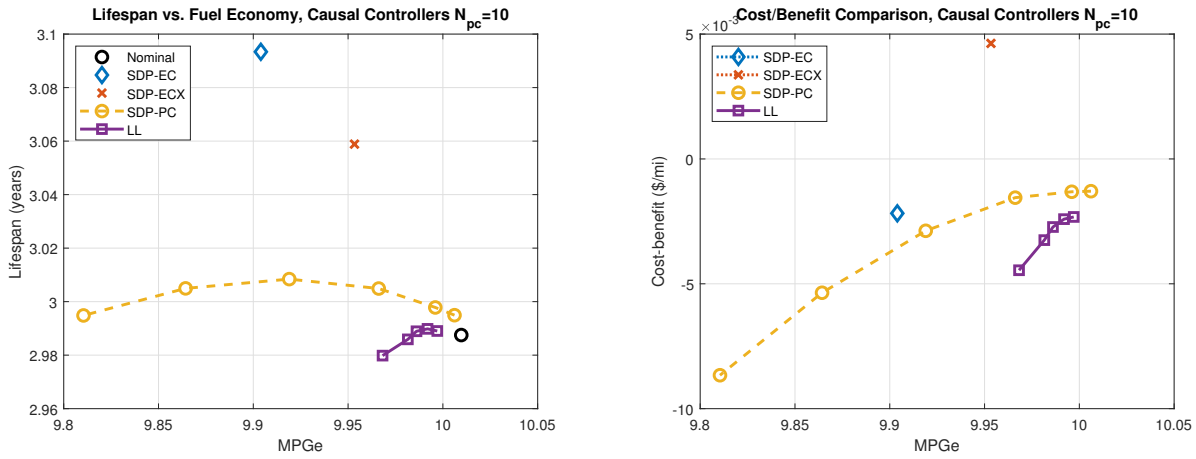

(a) (b)

FIGURE 5.6. Comparison of energy consumption with (a) battery aging and (b) cost-benefit for the four causal control methods, $N_{pc} = 10$.

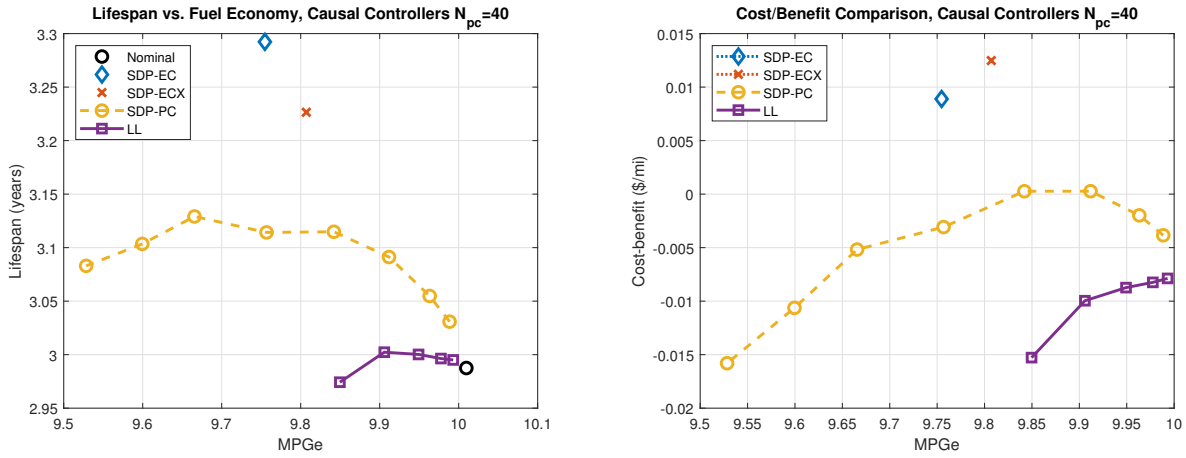

(a) (b)

FIGURE 5.7. Comparison of energy consumption with (a) battery aging and (b) cost-benefit for the four causal control methods, $N_{pc} = 40$.

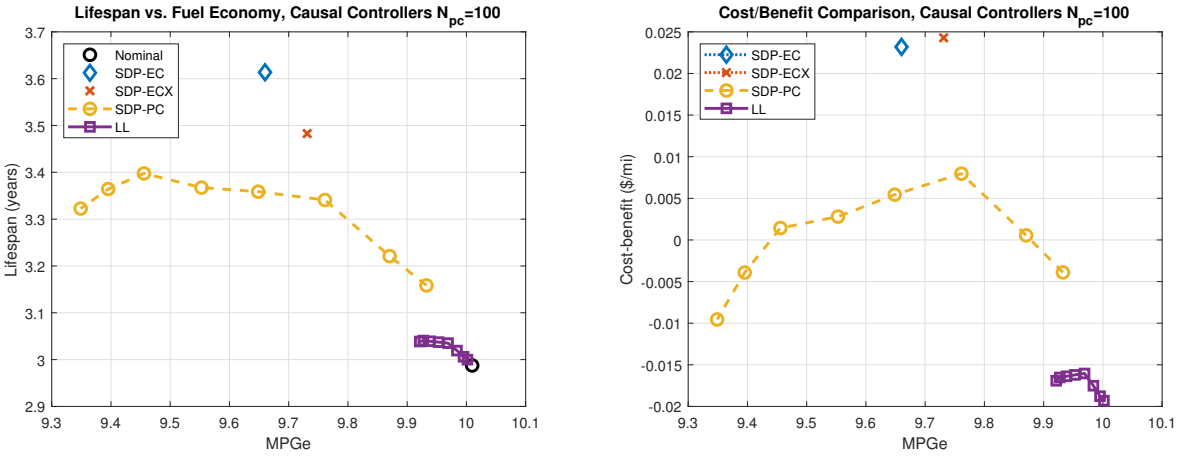

(a) (b)

FIGURE 5.8. Comparison of energy consumption with (a) battery aging and (b) cost-benefit for the four causal control methods, $N_{pc} = 100$.

TABLE 5.6. Comparison of Equivalent Cost Controllers with SDP.

UC Size (N_{pc})	**Type**	**Lifespan** (Years)	**MPGe**	**UC Aging** (%/Year)	**CPM** ($/mi)	**Payback Time** (Years)
N/A	Nominal	2.99	10.01	–	–	–
10	EC	3.09	9.90	26.29	-0.0022	N/A
	ECX	3.06	9.95	4.26	0.0046	8.8
40	EC	3.29	9.75	9.26	0.0089	18.2
	ECX	3.23	9.81	4.16	0.0125	13.0
100	EC	3.61	9.66	6.43	0.0232	17.5
	ECX	3.48	9.73	4.08	0.0243	16.7

5.5.4. Cost-Benefit Analysis. So far, it has been observed at that the ECX method offers clear value over the other methods: For any HESS sizing, the ECX method offers the highest benefit per mile. In the $N_{pc} = 10$ case, it was shown to be the only method that offered a positive return on investment. In the $N_{pc} = 40$ and $N_{pc} = 100$ case, while the EC and PC methods did offer a positive return, the ECX clearly outperformed them.

The estimated payback time was also computed for each method, and it was observed that the payback time increased as the ultracapacitor size increased: For the SDP-ECX controller, the small

HESS ($N_{pc} = 10$) had a payback time of 8.8 years, the mid-sized HESS ($N_{pc} = 40$) had a payback time of 13.0 years, and the large HESS ($N_{pc} = 100$) had a payback time of 16.7 years.

In order to observe the full trend of the payback period for different ultracapacitor sizes, additional simulations are run for N_{pc} equal to 2, 5, and all increments of 10 between 10 and 100 for the SDP-ECX strategy. The optimal EMS is recomputed for each new sizing and the vehicle is simulated again for the new EMS and new UC size. The payback time and battery lifespan are then plotted in Figure 5.9. This confirms that although increasing the HESS does improve the battery lifespan, the cost of the extra UC modules exceeds the savings of that extra lifespan.

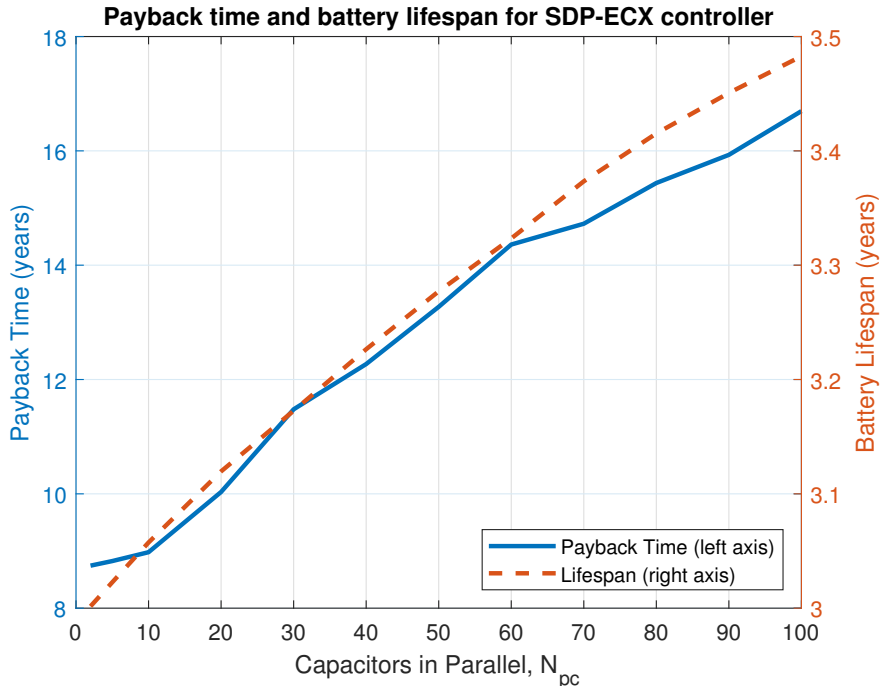

FIGURE 5.9. Estimated payback time for optimal SDP-EC controller with varying HESS size.

Finally, it must be noted that payback times in the period of 8 to 16 years may be outside the range of what a manufacturer or transit authority considers reasonable. However, it must also be noted the sensitivity of the benefit per mile and the payback time period to assumptions about component pricing, energy pricing, and aging mechanisms. For instance: This research assumes that energy is priced at the US average across all sectors, $Val_{nrg} = \$0.1065$/kWh [**143**]. If instead energy was priced at the transportation sector average for the state of Illinois (such as for a Chicago Transit Authority bus), the energy price of $Val_{nrg} = \$0.0632$/kWh, also from [**143**],

would reduce the payback time by approximately 16%. On the other hand, the California price $Val_{nrg} = \$0.1280$/kWh would increase the payback time by 11%.

Alternatively, we can consider that battery and UC components use the pricing of Reference [**145**] rather than [**142**] while maintaining $Val_{nrg} = \$0.1065$/kWh; the increased battery and ultracapacitor prices from [**145**] result in a payback time of 7.0 years for the $N_{pc} = 10$ UC and 13.0 years for the $N_{pc} = 100$ UC—higher component prices mean that there is more value derived from extending the component lifespan. On the other hand, the component prices of [**146**] would indicate that the HESS is not beneficial under any circumstance.

Alternatively, the Power Law aging model in Section 2.3.2 models lithium ion phosphate batteries as aging at up to 3× the rate of the Cycle Counting model used in this research. (This observation will be discussed more in Chapter 6). If the battery ages even 1.5× the modeled rate, then we would see a payback period of 5.2 and 9.8 years for $N_{pc} = 10$ and $N_{pc} = 100$, respectively.

Finally, although battery end-of-life can be considered a hard limit for battery use based on range constraints, the ultracapacitor on the other hand can continue to be used beyond 80% capacitance fade. This would not be unreasonable, considering how Figure 5.9 shows that the effectiveness of the proposed control method is maintained as the number of cells (and over UC pack capacitance) is decreased. So if, for instance, the UCs were used until 70% capacitance fade, then we would see a payback period of 8.0 and 13.6 years for $N_{pc} = 10$ and $N_{pc} = 100$, respectively.

All this is to say: an engineer must take caution that a HESS is economically appropriate for a given application; there may be circumstances where a HESS is highly beneficial, and others where it may be impractical. With that said, this research has demonstrated that for any HESS sizing and for any given MPGe, the SDP-EC method offers a larger increase to battery lifespan and a higher benefit per mile than the other considered methods. The important takeaway of this analysis is how proper control of the HESS is critical for both maximizing battery lifespan and HESS value, and that joint control of battery aging, UC aging, and energy losses is the most effective method to manage the HESS.

5.6. Conclusions

This research develops an ultracapacitor aging models for use in control. UC aging is incorporated into a vehicle energy management strategy, such that battery aging, UC aging, and energy

losses are jointly minimized. Three benchmark strategies are also developed: joint optimization of battery aging and energy losses but *not* UC aging, a simple SDP controller that limits large battery current but does not control aging, and a load leveling controller. As a case study, these controllers are applied to a simulated electric bus to determine the battery lifespan and energy consumption of the each strategy. An array of different HESS sizes and controller tunings are simulated in order to determine the trade-off between battery aging and energy consumption for each strategy. Additionally, the cost-benefit of the HESS is analyzed to determine the relative economic benefit of the proposed control strategies.

Simulation results showed that the newly proposed SDP-ECX method, which controls a weighted combination of battery aging, ultracapacitor aging, and energy losses, offers the best improvement to the aging-energy consumption trade-off across all considered HESS sizes. At the largest UC size, this strategy offered a 16.4% increase to battery lifespan and required only a 2.8% decrease in MPGe. The SDP-EC method, which controls battery aging and energy losses but not ultracapacitor aging, was highly effective at increasing battery lifespan but achieved these results at the expense of significant ultracapacitor aging, resulting in a worse overall cost-benefit.

Future work for this research includes optimization of component sizing, given the proposed new methods of energy management. Other energy management strategies should be considered and compared to the methods here, such as DDP formed into a rule base, model predictive control, or on-line applications Equivalent Consumption Minimization Strategy. Additionally, the next two chapters build on this work, with Chapter 6 investigating the robustness of the proposed control strategies to uncertainty in the battery aging model, and Chapter 7 extending this work to HEV applications.

CHAPTER 6

Analysis of the Robustness of Battery Aging Models for Control

In the previous chapter, a cycle-counting based aging model was used to implement aging-aware energy management. However, this study and the existing literature generally take for granted the accuracy of the controller's aging model, despite a wide variety of aging models available. This chapter investigates the robustness of different battery aging models: First, dynamic programming is used to produce optimal aging-aware energy management strategies. Then, these strategies are simulated on a vehicle for cases where the battery aging model matches the aging model used in the controller and cases where it substantially differs. Simulation results show that an energy management system designed with the "incorrect" aging model have considerably worse performance than those designed with the "correct" model. However, aging control using the cycle-counting model or the severity-factor approach to the power-law model can be easily re-tuned using a simple measurement of aging rate; aging control designed using the full power-law dynamics would require a full refitting of the battery aging model.

6.1. Introduction

A challenge to developing aging-aware energy management is the wide array of aging models present in the literature. Research of battery aging in EVs and HEVs instead tends to utilize empirical models [**5**, **15**, **16**, **17**, **18**, **19**, **20**]. For instance, references [**15**, **16**, **21**, **22**] develop aging models that relate charge throughput to degradation, with temperature and current magnitude as additional stress factors. References [**23**, **24**] include depth of discharge as an additional stress factor, while [**24**] also distinguishes the impact of charging versus discharging currents on battery degradation. The aging models for hybrid vehicle applications in [**19**, **20**] consider number of charge/discharge cycles and calendar life and use temperature, depth of discharge, and average state of charge as aging stress factors. Other models in the literature such as [**11**, **28**, **43**, **147**] use simple cycle counting to measure the state-of-health. [**148**] provides a comprehensive review of the variety of degradation models that have been developed. This array of literature includes

research purely on developing aging models, such as in the case of [**11**, **19**, **21**, **22**, **23**, **24**, **43**], and direct applications of the developed models to EV and HEV systems, including vehicle-to-grid studies [**15**, **16**, **20**], diagnostic tools for EVs and HEVs [**18**, **28**], and evaluating the effect of on-board photovoltaics [**28**, **147**, **149**].

All this is to say: there are a plethora of aging models and applications of aging models in the literature. However, existing literature on aging control in energy management has not considered uncertainty in aging dynamics—batteries are assumed to aging following the same model used to design or size the aging-aware energy management system, and it may not always be practical or feasible for an engineer to carry out the amount of testing needed to fit their batteries' aging behavior to a a given aging model. If battery aging behavior is significantly different from the model used in control development or used to size the HESS, are the results still valid?

This research demonstrates the robustness of battery aging control to substantial model variations. Given that battery aging is a slow process and aging tests are destructive to the battery and therefore are expensive, the simulations proposed in this chapter are an ideal way to explore the robustness of battery degradation control methods. The contribution of this research is the analysis of how well aging-aware control holds up when subjected to an uncertain battery aging model, and proposed adjustments to aging control methods when and the discussion of why the strategies experience this degree of robustness to uncertainty.

This chapter begins with a brief overview of the vehicle modeling method is in this research and a more detailed overview of the two used methods of battery aging modeling, one based on cycle-counting [**24**] and one based on charge throughput [**21**]. In the next section, the method for designing energy management systems for aging control are using dynamic programming are described. Deterministic Dynamic Programming (DDP) is used for finding a global optimal result, while Stochastic Dynamic Programming (SDP) is used for causal, implementable controllers. The vehicle model and energy management strategies are then applied to a case study of an electric bus with a HESS and simulated for the lifespan of the battery for both aging models. Finally, these simulation results are analyzed and compared. A simple SDP control that does not use an aging model is used as a baseline for comparison, as well as a case where an ultracapacitor is not used at all. Conclusions are drawn regarding how well the controllers perform when the designed aging model does not match the simulated aging model.

6.2. Modeling and Control

Once again, because of the cost to implement and test the proposed system and the time needed to run the battery to the end of its life, simulation is used to assess the performance and robustness of the proposed energy management strategies on an electric vehicle. The study uses the same vehicle, battery, and ultracapacitor models as the study in Chapter 5, with parameters given in Tables 6.1–6.3.

TABLE 6.1. Vehicle model physical parameters.

Parameter	**Variable**	**Value**
Vehicle Mass	M_v	18,181 kg
Frontal Area	A_f	8.02 m^2
Drag Coefficient	C_D	0.55
Roll Resistance Coefficient	C_R	0.008
Wheel Inertia	J_w	20.52 kg-m^2
Motor Inertia	J_m	0.277 kg-m^2
Wheel Radius	R_w	0.48 m
Final Drive Ratio	N_{fd}	5.1:1
Gearbox Ratio	N_{gb}	5:1
Transmission Efficiency	η_{trans}	96%

TABLE 6.2. Battery model parameters.

Parameter	**Variable**	**Value**
Battery Cells in Series	N_{ser}	100 cells
Battery Series Sets in Parallel	N_{par}	160 sets
Total Charge Capacity	$Q_{batt,pack}$	368Ah
Nominal Open Circuit Voltage	$V_{ocv,pack}$	330v
Nominal Equivalent Resistance	$R_{s,pack}$	5.5 mΩ

TABLE 6.3. Ultracapacitor model parameters.

Parameter	Variable	Value
UC Modules in Series	N_{sc}	100 modules
UC Series Sets in Parallel	N_{pc}	60 sets
Resistance	$R_{uc,pack}$	73.8mΩ
Capacitance	$C_{uc,pack}$	63.5F

Both the cycle counting aging model and power law aging model, presented in Sections 2.3.1 and 2.3.2 respectively, are used in this study. Neither implementation includes a thermal model; instead in both cases the battery pack is assumed to have a cooling system, such that the battery temperature is maintained at 35°C. These models have the same fundamental underpinnings: large currents and temperatures are exponentially worse for the battery; every instances of battery usage, whether measured in throughput or cycles, ages the battery. Some differences include the overall aging rates each model predicts, particular rates at which damage increases due to temperature and large currents as measured by [**21**] and [**24**], whether charging and discharging currents are treated as distinct (as in the cycle-counting model) or the same (as in the power law model), and whether usage is measured in charge throughput or charge-discharge cycles of varying depths. The biggest difference, and the one that may lead to significant variation in controller performance, is how damage accumulation varies with time: In the power law model, the capacity fade rate is approximately proportional to the inverse square root of the throughput. From Equation (2.68),

$$\frac{dQ_{loss}}{dt} \propto Ah^{z-1} \tag{6.1}$$

where $z \approx 0.552$ [**21**]. In other words, the degradation rate decreases as the battery is used and throughput increases. On the other hand, the cycle-counting method assumes linear accumulation of damage: identical cycles produce identical capacity fade, regardless of the battery's instantaneous state of aging.

The ultracapacitor aging model from Section 5.2 is used as well.

Finally, the Equivalent Cost Extended (ECX) strategy developed in Section 5.3 is used to assess the affect of aging model variation on controller performance, using both the DDP and SDP

approaches. ECX controllers developed using the cycling counting aging model are denoted ECX-CC, while those developed with the power law aging model are denoted ECX-PL. Additionally, a second set of power-law controllers are developed using the severity factor method described in Equations (2.71)–(2.77), denoted ECX-SV. The ECX-CC and ECX-PL use the same number of state variables; the CC method uses a discharge depth state variable to evaluate battery damage, while the PL method uses a throughput state variable. Because the severity factor approach to the power law aging model does not track throughput, the ECX-SV controllers have one fewer state variable. The Power Control (PC) method, also from Section 5.3, is used as a benchmark strategy: The PC method limits battery aging independently of an aging model, so if the ECX controller subjected to aging model variation performs worse than the PC method, we can say that the ECX controller is not robust.

The controllers used in this study use the same constraints as Section 5.2.

6.3. Case Study

The model and developed controllers are now used for a case-study analysis of aging-aware energy management: Simulation is used to determine how the various strategies perform when the aging model used to develop the EMS matches the true HESS aging and for when it differs from the true HESS aging. Overall, the two battery aging models differ in both structure, such as how overall use is counted (cycle-counting versus throughput counting), whether discharging current magnitude has a different or identical effect to the charging current magnitude, the type of curve-fits used, and whether or not the aging model includes resistance growth, and in the overall differences in aging rates found from the respective experimental trials.

As in Chapter 5, the high-order ultracapacitor and battery models are used for simulation, while the low-order models are used for control. Cycle-counting aging considers discharge depth, charging current magnitude, and discharging current magnitude as aging factors, while power-law aging considers throughput and current magnitude. In both cases, temperature is assumed constant. Each strategy is simulated on the OCTA bus drive cycle [**128**] repeated for two hours. This is drive cycle consumes more energy from the MBC used in Chapter 5, and sees the battery SOC drop to approximately 30% after these two hours of driving at battery start-of-life.

In this research, DDP is used to obtain the global-optimal control strategy for a given control method and represents the best-case scenario for a controller type. Because DDP represents an unobtainable optimum, DDP-ECX-CC is only simulated with cycle-counting aging, and DDP-ECX-PL and DDP-ECX-SV are only simulated with power law aging. SDP on the other hand represents a causal, implementable controller and offers a more realistic understanding of the capabilities that strategy. So, the SDP controllers are simulated on both types of aging. Thus, each causal ECX controller is simulated for a case where the aging dynamics are known (the controller aging model matches the simulated aging) and unknown (the controller aging model differs from the simulated aging). SDP-PC is simulated for both cycle-counting and power-law aging for controller tunings ranging from $Q_P = 10^{-14}$ to $Q_P = 10^{-11}$. Additionally, a single baseline case that does not use the ultracapacitor is simulated and is referred to as the nominal vehicle simulation.

Simulations begin with both the battery and ultracapacitor at the beginning of their life. After each full discharge cycle, the aging of the battery and ultracapacitor are measured, and the capacity, capacitances, and resistances of the HESS are updated. For the purpose of measuring aging, the battery is assumed to recharge at a rate of 0.5C. Simulations are then repeated until the battery reaches the end of its life, at which point the cycle life, ultracapacitor state-of-aging, and average energy consumption are measured and recorded. In each simulation, the battery starts at $SOC_b = 95\%$ and the ultracapacitor starts at $SOC_c = SOC_{c,tgt} = 75\%$.

Energy consumption is measured in miles per gallon gasoline-equivalent (MPGe), while battery aging is presented in an approximate lifespan in years. The approximate lifespan is obtained from a measured capacity loss per mile and an estimate of 34,000 miles driver per year for an average transit bus [**141**]. The cost-benefit of each controller is evaluated used the steps presented in Equation (5.14)–(5.19), using the same battery, ultracaapacitor, and energy values as in Chapter 5.

6.4. Results

Throughout this section, cases where the controller aging model matches the simulated aging model are referred to as "nominal aging." Likewise, cases where the controller aging model differs from the simulated aging model are referred to as "uncertain aging."

The results of each simulation are plotted in Figure 6.1 and Figure 6.2. Each point on the plots represents a complete simulation for a particular controller type and tuning parameter value.

Figure 6.1 shows results where the Cycle Counting aging method is simulated, while Figure 6.2 shows results where the Power Law aging method is simulated.

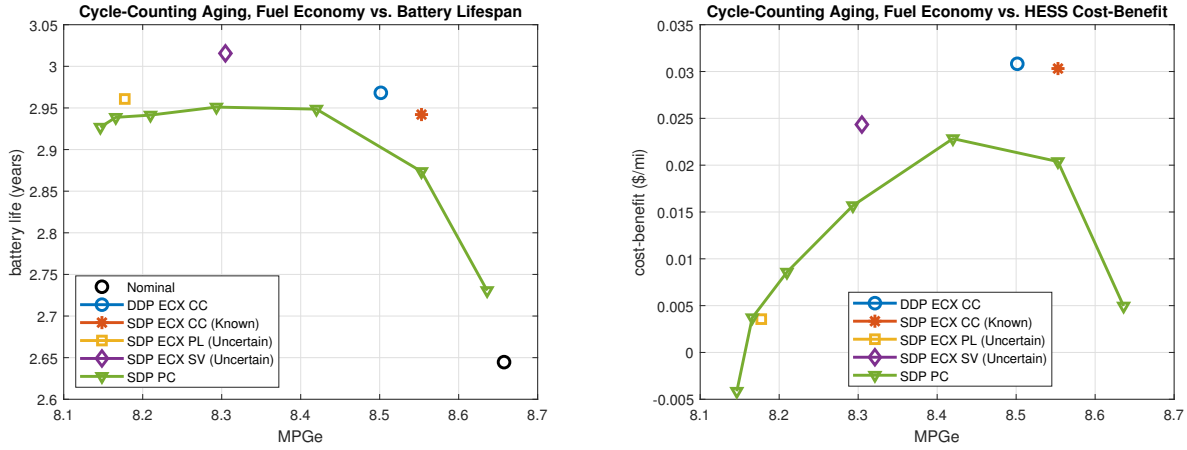

(a) (b)

FIGURE 6.1. Comparison of energy consumption with (a) battery aging and (b) economic benefit for aging via Cycle Counting Model.

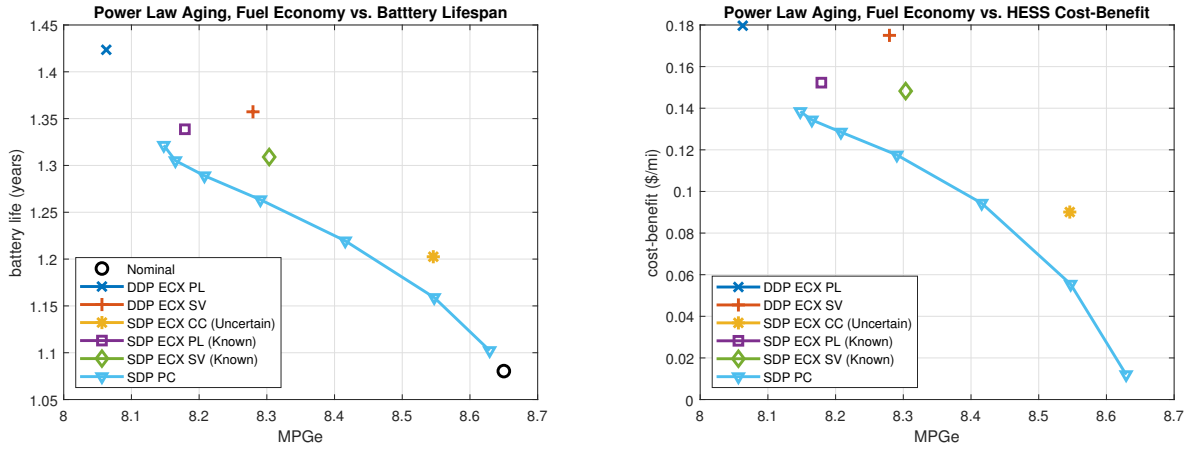

(a) (b)

FIGURE 6.2. Comparison of energy consumption with (a) battery aging and (b) economic benefit for aging via Power Law Model.

The first thing to notice is that the two different aging models predict substantially different battery lifespans, whether measured in terms of operational years, lifetime battery throughput, or cycle life. Before considering the effects of the HESS, the same vehicle and sees the cycle-counting method predict 2.5× the life of the power-law method. The cycle-counting model see the

HESS provide a peak lifespan increase of 13.2% on the cycle counting model, compared to a 32.5% increase when measured on the power-law model. It is not the goal of this study to reconcile the differences between these models, which are both based on empirical real-world testing of lithium iron phosphate batteries; the models used in this chapter are able to accurately reproduce the results of the models produced in the original literature [**21**] and [**24**]. Rather, the goal is only to review how these differences impact the performance of aging-aware energy management.

The DDP and SDP methods are compared for the nominal case—when the simulated aging method matches the method used to design the energy management strategy. In both Figure 6.1 and Figure Figure 6.2, it can seen that the SDP result closely tracks the DDP global optima, indicating that the SDP controllers behave as intended. A full comparison of the nominal results are summarized in Table 6.4. Additionally, the severity factor approach used in the ECX-SV controllers is shown to be a reasonable approximation of the full power-law aging dynamics used in the ECX-PL controllers: Figure 6.2(a) shows that the severity factor approach offers lesser lifespan improvements but greater mileage, resulting in an overall economic benefit that is 2.7% lower than control with the full dynamics for both DDP and SDP, as shown in Figure 6.2(b).

Table 6.4. Comparison of DDP and SDP controllers for nominal aging.

Type	**Lifespan (Years)**	**MPGe**	**UC Aging (%/Year)**	**BPM ($/mi)**
Nominal (CC)	2.65	8.66	–	–
Nominal (PL)	1.08	8.65	–	–
DDP-ECX-CC	2.97	8.50	3.02	0.031
SDP-ECX-CC	2.94	8.55	3.43	0.030
DDP-ECX-PL	1.42	8.06	4.07	0.180
SDP-ECX-PL	1.34	8.18	4.97	0.152
DDP-ECX-SV	1.38	8.28	3.67	0.175
SDP-ECX-SV	1.31	8.30	3.22	0.148

Next, the causal strategies (SDP-ECX-CC, SDP-ECX-PL, and SDP-Power) are compared for both aging models, with results summarized in Table 6.5 for cycle counting aging and in Table 6.6 for power law aging. Expectedly, the SDP-ECX-CC controller has the best economic benefit when

actual aging uses the cycle counting model, and the SDP-ECX-PL controller has the best economic benefit when actual aging uses the power law model. Interestingly, the SDP-ECX-PL and SDP-ECX-SV controllers increase battery lifespan to a greater degree than the SDP-ECX-CC controller on when simulating with cycle-counting aging. However, this is obtained from increased fuel consumption, resulting in an 88% and 20% decrease in benefit per mile compared to the SDP-ECX-CC controller, respectively. On the other hand, the SDP-ECX-CC increases lifespan by only half as much as SDP-ECX-PL when simulating with power law aging, but uses considerably less fuel. The net result is a benefit per mile that is roughly half of the SDP-ECX-PL benefit per mile. The diminished performance of all three controllers points to neither method being particularly robust to aging model uncertainties, although the SDP-ECX-PL method fares considerably worse due to its high energy consumption.

If one knows the "true" aging model, then the SDP-PC controller is a distinctly worse choice than the SDP-ECX-CC or SDP-ECX-PL controllers. On cycle-counting aging, the peak benefit of the SDP-PC controller is approximately \$0.023/mi for a tuning parameter value of $Q_P = 10^{-11.8}$; on power-law aging, converges to a benefit of \$0.14/mi as Q_P is made increasingly large. However, the SDP-PC method suffers similar robustness issues to the SDP-ECX controllers: if one were to tune the SDP-PC controller based on a cycle-counting aging model and choose $Q_P = 10^{-11.8}$ yet have aging that follows the power-law model, the benefit per mile would be half of what could have been obtained—effectively equal to the SDP-ECX-CC controller. Similarly, if one were to tune the SDP-PC controller based on a power-law aging model and choose a larger Q_P ($Q_P > 10^{-10.5}$) yet have aging that follows the cycle-counting model, there would in fact be no economic benefit: the ultracapacitor cost and high energy usage would outweigh the battery lifespan increases.

TABLE 6.5. Comparison of Causal Controllers for Simulation with Cycle Counting Aging Model.

Type	Lifespan (Years)	MPGe	BPM ($/mi)	Life wrt SDP-ECX-CC	BPM wrt SDP-ECX-CC
SDP-ECX-CC (Nominal Aging)	2.94	8.55	0.030	—	—
SDP-ECX-PL (Uncertain Aging)	2.96	8.18	0.004	+0.64%	−88.2%
SDP-ECX-SV (Uncertain Aging)	3.02	8.31	0.024	+2.52%	−19.7%

TABLE 6.6. Comparison of Causal Controllers for Simulation with Power Law Aging Model.

Type	Lifespan (Years)	MPGe	BPM ($/mi)	Life wrt SDP-ECX-PL	BPM wrt SDP-ECX-PL
SDP-ECX-PL (Nominal Aging)	1.34	8.18	0.152	—	—
SDP-ECX-SV (Nominal Aging)	1.31	8.30	0.148	−2.24%	−2.62%
SDP-ECX-CC (Uncertain Aging)	1.20	8.56	0.090	−10.1%	−40.8%

6.5. Controller Refinement

We observe that the difference in aging rate between the two models appears to be the primary source of error. Recall the instantaneous cost function used to design the ECX controllers from Section 6.

$$L(x, u, w) = Cost_{batt}\Delta D + Cost_{elec}E_{loss} + Cost_{UC}\Delta SoA \tag{6.2}$$

If the aging model produces large ΔD values then the controller expends more energy (allow higher E_{loss}) to keep battery aging low, and vice versa. We see this reflected in the results shown in

Figure 6.1 and Figure 6.2: The power-law aging model predicts a faster aging rate, and the ECX-PL controllers correspondingly allow larger energy losses to limit aging. The cycle-counting model predicts a slower aging rate, and the ECX-CC controllers result in greater fuel economy, as battery degradation is comparatively less important.

We next consider that one could measure the aging rate of the batteries used in the vehicle under the expected operating conditions, and compare this to the predictions given by model and data in the literature. Then, the relative difference between the modeled and actual aging rates could then be used to adjust the ECX instantaneous cost function.

$$Q_{aging} = \frac{\text{Measured aging rate}}{\text{Modeled aging rate}} \tag{6.3}$$

$$L(x, u, w) = Q_{aging} Cost_{batt} \Delta D + Cost_{elec} E_{loss} + Cost_{UC} \Delta SoA \tag{6.4}$$

(Again, we must consider that while performing a full array of battery aging tests to precisely fit a model to one's batteries might be the most accurate option, it is not always practical or feasible to do this.) This adjustment corresponds to adjusting the $CL\text{-}DOD$ curve fit in Equation (2.56) for the cycle-counting model, and adjusting the $A(I_b)$ curve-fit parameter in Equation (2.68) for the power-law aging model.

This correction factor is next tested on the three SDP-ECX control strategies. Simulation results show that in the nominal case, the cycle-counting model predicts a roughly 2.5× longer lifespan than the power-law model. We can use this as a simple estimate for a Q_{aging} parameter to adjust the aging-aware energy management. If designing control using the cycle-counting model, but real aging follows the power-law model, one would measure an aging rate of 20% capacity fade in 1.08 years, but predict an aging rate of 20% capacity fade in 2.65 years. Then,

$$Q_{aging} = \frac{\frac{0.2}{2.65}}{\frac{0.2}{1.08}} = 2.45 \tag{6.5}$$

The SDP-ECX-CC controller can then be recomputed using this correction factor. For designing control using the power-law model, but real aging follows the cycle-counting model, this would be

$$Q_{aging} = \frac{\frac{0.2}{1.05}}{\frac{0.2}{2.65}} = 0.408 \tag{6.6}$$

Likewise, the SDP-ECX-PL and SDP-ECX-SV controllers can be redeveloped, now with the aging rate adjustment parameter. The vehicle is then simulated again following the same steps as before for the three new adjusted controllers. The new result are shown overlaid on the old results in Figures 6.3 and 6.4.

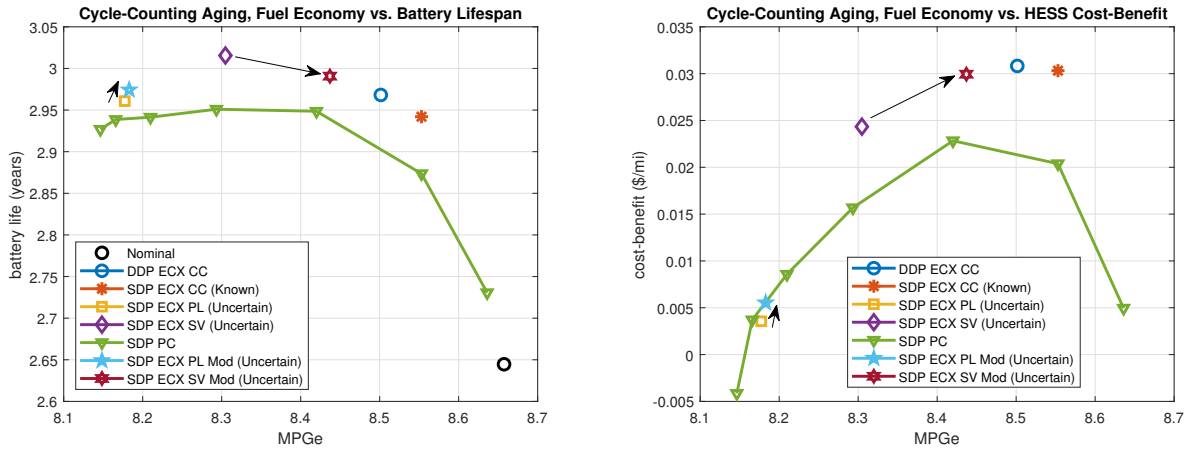

(a) (b)

FIGURE 6.3. Comparison of energy consumption with (a) battery aging and (b) economic benefit for aging via Cycle Counting Model, including adjusted SDP-ECX-PL and adjusted SDP-ECX-SV.

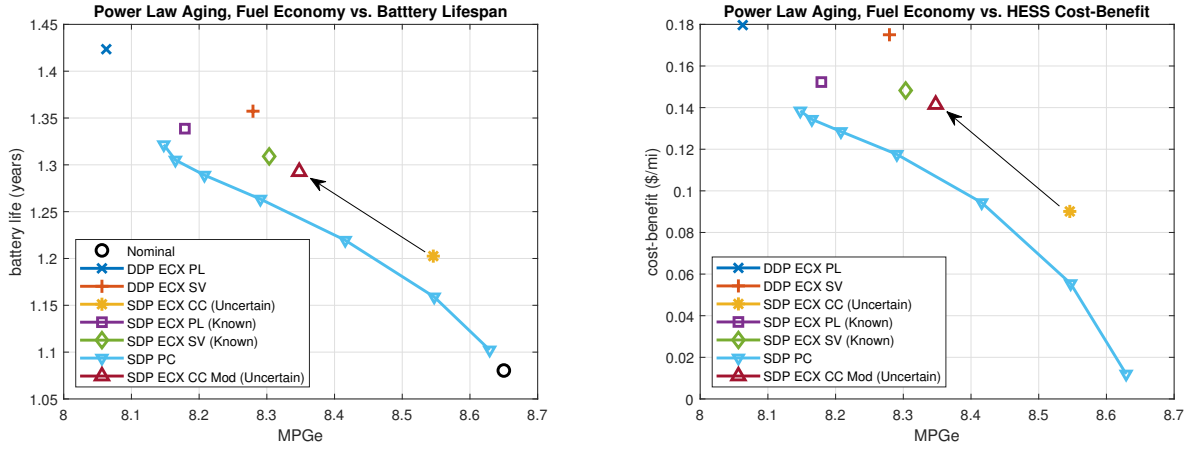

(a) (b)

FIGURE 6.4. Comparison of energy consumption with (a) battery aging and (b) economic benefit for aging via Power Law Model, including adjusted SDP-ECX-CC.

From Figure 6.4, we can see that the simple adjustment proposed in Equation 6.4 is sufficient to make a controller designed with the cycle-counting method robust to changes in the aging

model. The adjusted SDP-ECX-CC controller has lifespan within 3.4% and benefit per mile within 7.1% of the SDP-ECX-PL controller. On the other hand, Figure 6.3 indicates that the adjusted SDP-ECX-PL controller still performs poorly compared to the SDP-ECX-CC, while the adjusted SDP-ECX-SV controller is nearly able to match the SDP-ECX-CC performance.

6.6. Validation with Higher-Order Aging Model

As a final test of controller robustness to aging model variation, each of the controllers are simulated on a new, higher-order aging model. Developed in [**26**] and used in aging studies such as [**150**, **151**, **152**], this model builds off the same throughput and Arrhenius equation basis as [**21**] while incorporating calendar aging—time-dependent aging amplified at high temperatures and states-of-charge—and expanding cycle aging to cover three terms:

(1) High-temperature aging associated with total throughput;
(2) Low-temperature aging associated with total charging throughput and amplified by large charging current;
(3) An additional high-SOC term for low-temperature aging, again associated with total charging throughput and amplified by large charging current.

This model is given in the equations

$$Q_{\text{Loss}} = Q_{\text{L,Cal}} + Q_{\text{L,Cyc,High T}} + Q_{\text{L,Low T}} + Q_{\text{L,Low T,High SOC}} \tag{6.7}$$

$$Q_{\text{L,Cal}} = \int k_{\text{Cal}}(T, SOC_b) \cdot (2t^{0.5})^{-1} dt \tag{6.8}$$

$$Q_{\text{L,Cyc,High T}} = \int k_{\text{Cyc,High T}}(T, I_b, SOC_b) \cdot (2Q_{tot}^{0.5})^{-1} dQ_{tot} \tag{6.9}$$

$$Q_{\text{L,Cyc,Low T}} = \int k_{\text{Cyc,Low T}}(T, I_{bc}) \cdot (2Q_{ch}^{0.5})^{-1} dQ_{ch} \tag{6.10}$$

$$Q_{\text{L,Cyc,Low T,High SOC}} = \int k_{\text{Cyc,Low T,High SOC}}(T, I_{bc}, SOC_b) dQ_{ch} \tag{6.11}$$

where Q_{Loss} is a measure of capacity fade as in Equation 2.67 while $Q_{\text{L,Cal}}$ is the capacity fade related to calendar aging and the $Q_{\text{L,Cyc,i}}$ are the three cycle aging components listed above. t is the calendar time in hours, T is the battery temperature, SOC_b is the battery state-of-charge, Q_{tot} is the total ampere-hour throughput, Q_{ch} is the total *charging* ampere-hour throughput, and I_{bc}

is the charging current in amperes. The k_i terms are experimentally fitted functions, whose full definitions are not given here but can be found in [**26**].

As this model includes calendar aging and introduces time as a state variable, aging must be accounted for while the vehicle is not in operation. The bus is assumed to drive one cycle (as specified in Section 6.3) per day. After this driving period, the battery is held at $T = 20°C$ and at the final SOC, typically between $SOC_b = 25\%$ and $SOC_b = 5\%$ depending on the controller and battery age, before being recharged at 1/2 C just before the next driving period begins.

In this case, all SDP-ECX controllers are being simulated on an "unknown" aging model, although the power-law model bears more similarity to the high-order model than the cycle-counting model does. Developing a controller based on this higher-order model is outside the scope of this work, so there is no performance benchmark for an aging model with certain aging dynamics.

The nominal case, unmodified SDP-ECX, and SDP-PC controllers are simulated first. The Q_{aging} adjustment parameter is then found by comparing the expected aging found in Section 6.4 to the newly found aging for the nominal case, which is then used to tune and simulated the adjusted SDP-ECX controllers. The simulation results are shown in Figure 6.5.

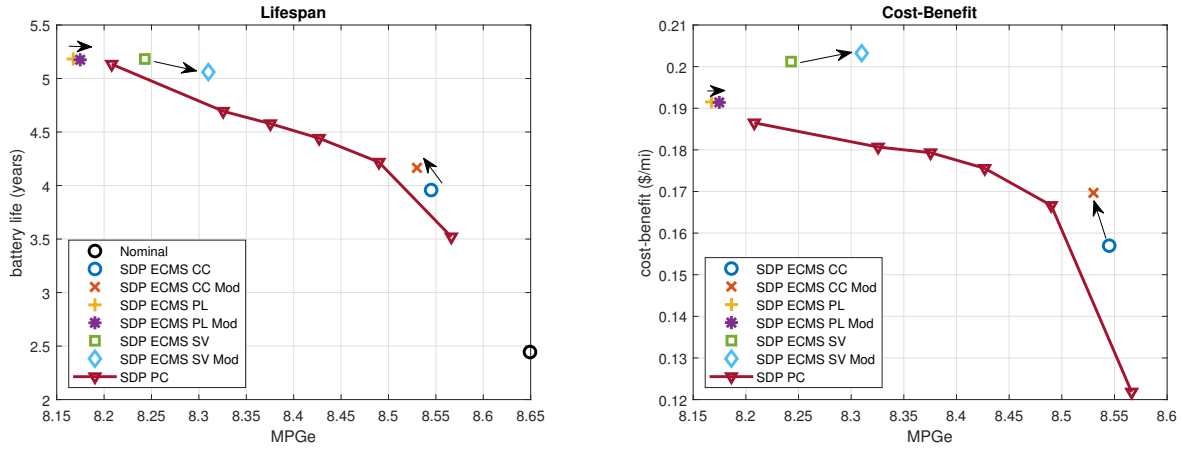

(a) (b)

FIGURE 6.5. Comparison of energy consumption with (a) battery aging and (b) economic benefit for aging via on a higher-order aging model.

The first and most notable result is that all three controllers perform well without adjustment. All offer clear lifespan improvements over nominal as well as a positive economic benefit per mile. Although more complex dynamics such as calendar aging and accelerated aging at high SOC were

not included in the control, aging-aware energy management still outperformed the aging unaware-controllers in terms of both battery lifespan increase and economic viability.

As seen throughout this chapter and Chapter 5, aging-aware control incurs additional energy losses from the ultracapacitor's internal resistances and uses the ultracapacitor to as a buffer against aging due to high currents such as from regenerative braking. As a result, a battery subject to aging-aware control is depleted more rapidly than the nominal battery, such as shown for a segment of time in Figure 6.6(a). Additionally, the aging-aware control uses the ultracapacitor as a buffer against large charing and discharging associated with regenerative braking and accelerating from rest, and tamps down the "microcycles" seen in the nominal vehicle's battery state-of-charge. This reduces charging currents including while in the high SOC region, as shown in Figure 6.6(b). For instance the decrease from 7A to 3.5A between the nominal and SDP-ECX-SV simulations seen in the peak at $t = 1360$ seconds in Figure 6.6(b) decreases the $k_{\text{Cyc,Low T,High SOC}}$ term by a factor of 938.

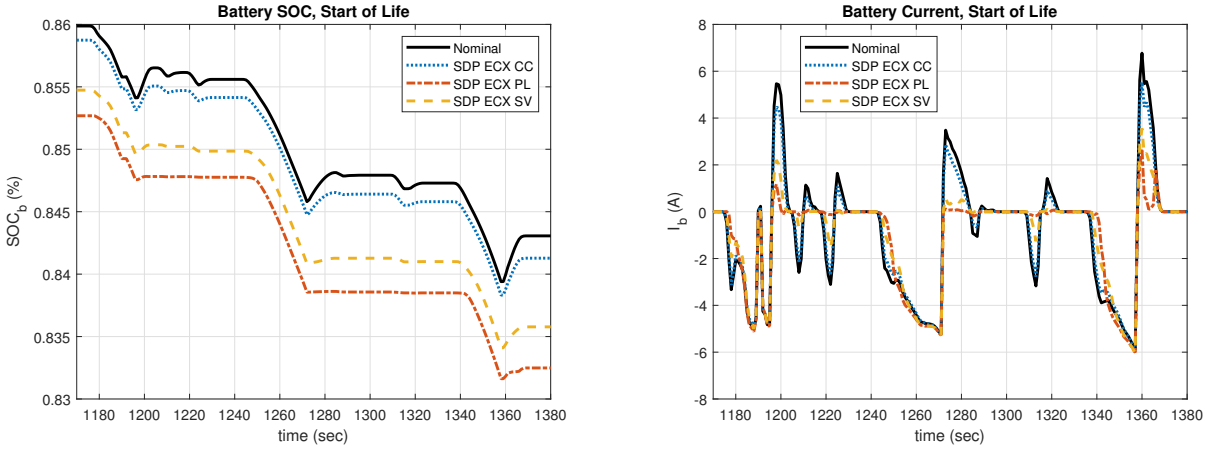

(a) (b)

FIGURE 6.6. Comparison over a segment of time of (a) battery state-of-charge and (b) battery current at battery start-of-life.

Overall, this leads to the reduction in calendar aging and cycle aging associated with charging the battery (especially at high battery SOC), even when those dynamics are not modeled in the aging-aware control. Figure 6.7 compares each aspect of aging for the nominal vehicle and for the vehicles with aging-aware energy management over the first 10 days of driving; methods that use the ultracapacitor more heavily are seen to have lower aging across all four aging factors.

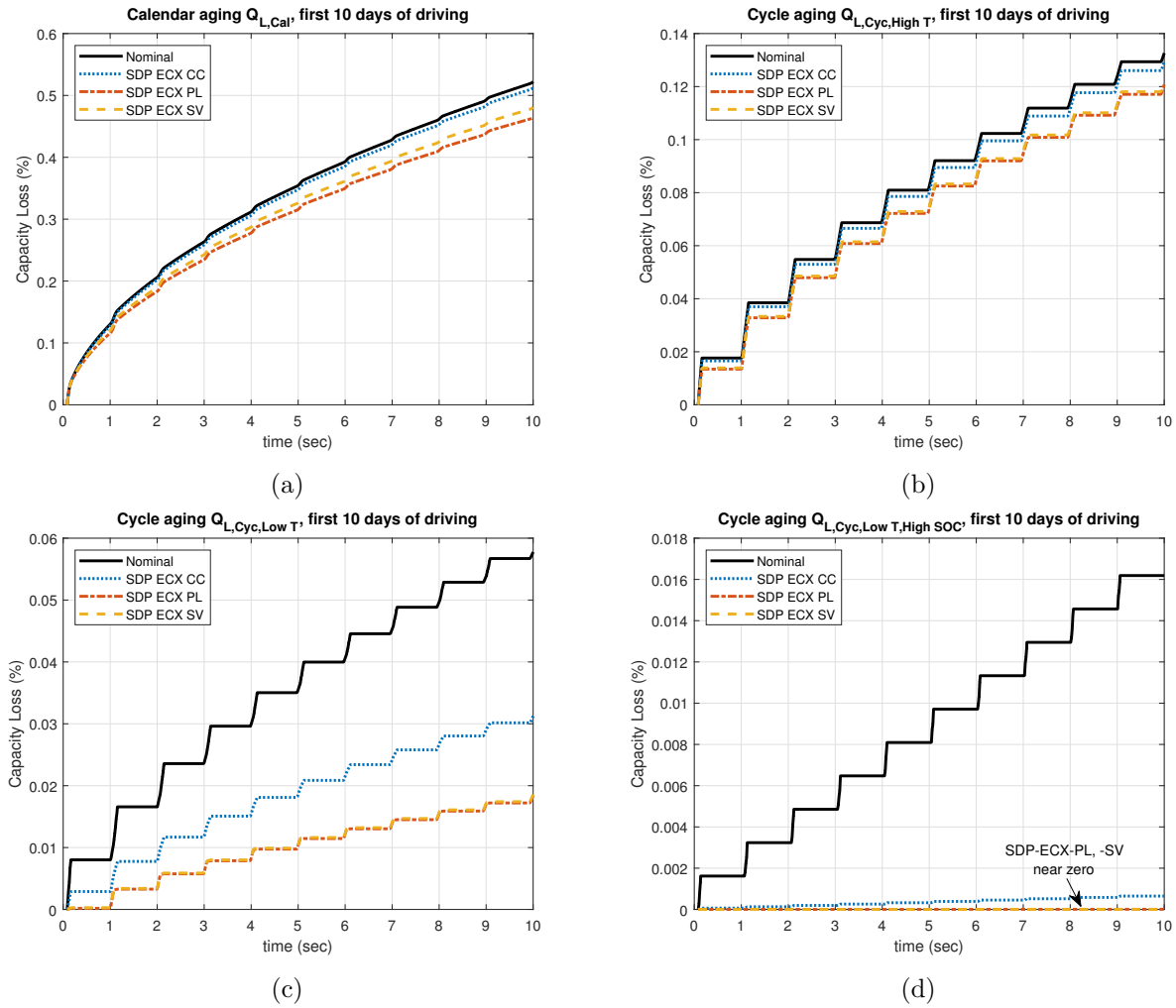

FIGURE 6.7. Comparison of (a) calendar aging, (b) high temperature cycle aging, (c) low temperature cycle aging, and (d) low temperature, high state-of-charge cycle aging over the first 10 days of driving.

Next, we see that the adjustment parameter improves the benefit per mile in all three cases. The nominal battery lifespan for the new aging model is seen to be marginally less than the nominal lifespan for the cycle-counting model, so the adjustment factor the SDP-ECX-CC solution to value the battery slightly more, leading to an increase in lifespan and economic benefit at the expense of energy consumption. On the other hand, the power-law model predicts a shorter lifespan than the high-order model, so the adjusted controllers relax their emphasis on increasing battery lifespan in favor of decreasing energy consumption, but in a manner that increases the overall economic benefit. Similar to what was seen in the previous section, the two controllers using linear damage

accumulation both performed better overall and responded better to the aging rate adjustment than the method without linear damage accumulation.

Overall, it appears that in absence of a aging model verified for one's particular batteries, the most robust choice for aging-aware energy management strategy is to design the controller using an aging model with linear damage accumulation and to obtain a basic estimate of one's batteries' lifespans relative to the aging model's prediction. The two controllers that consider damage to accumulate linearly maintain a reasonable economic benefit when subject uncertainty in the aging dynamics. A simple scaling of the aging rate—without adjusting any other model parameters—allows both to come relatively close in performance to controllers that do not have aging model variations.

On the other hand, a controller designed on the full power-law method and subjected to aging behavior variations sees severely diminished economic benefit due to excessive energy consumption, and does not respond to simple aging rate adjustments. This model may work well if the battery aging model parameters can be fully refitted for a particular use case, but without such a validated model, it may produced a poorly-tuned controller.

6.7. Conclusions

This chapter presents controllable battery and ultracapacitor aging models for a HESS. In the previous chapter, an energy management strategy was developed for the purpose of minimizing battery aging; this strategy can use either a cycle counting aging model or a power law aging model for controlling battery damage. Control using the power-law aging model can either use the full aging dynamics or a "severity factor" approach that models damage accumulation as linear.

As a case study, this strategy is applied to a simulated electric bus. The control strategy is designed using either aging model and simulated on either aging model for both DDP and SDP controllers. An SDP controller that penalizes large battery power was also simulated as a benchmark case. The range of cases simulated allows us to evaluate the robustness of the battery aging control to uncertainty in the actual aging behavior.

Simulation results showed that an energy management system designed with the "incorrect" aging model had degraded performance: The SDP-ECX-CC controller improved lifespan by less than half as much as the SDP-ECX-PL controller when simulating with power-law aging. On the

other hand, the SDP-ECX-PL and SDP-ECX-SV controllers, when simulated for cycle-counting aging, consumed substantially more energy than the SDP-ECX-CC controller, to the extent that there was little to no economic benefit to the HESS.

A simple aging-rate adjustment was proposed to improve the aging control strategy. One could measure the aging rate of their battery, compare it the rate predicted by an aging model, and scale model's damage term by the ratio between them. This method was first applied to the SDP-ECX-CC controller being used where battery aging follows the power-law model, and was shown to improve the SDP-ECX-CC's robustness to aging model variation. The adjusted SDP-ECX-CC controller performed nearly as well as the SDP-ECX-PL controller: The economic benefit rose by 55% compared to the unadjusted controller and came within 10% of the controller not facing aging model uncertainty. On the other hand, the simple adjustment failed to improve the performance of the SDP-ECX-PL controller when subject to aging model uncertainty.

The aging rate adjustment was next applied to the SDP-ECX-PL and SDP-ECX-SV controllers being used where battery aging follows the cycle-counting model. On one hand, the adjustment improved the SDP-ECX-SV controller enough to nearly match the SDP-ECX-CC performance. On the other hand, the SDP-ECX-PL controller saw only marginal improvements to lifespan. This collectively points to the importance of using an aging model with linear damage accumulation (cycle-counting or the severity factor approach to power-law aging): such controllers could be easily tuned to match observed aging rates, while similar tuning on control using the power-law aging model proved ineffective.

A final test applied the various controllers to a higher-order battery aging model that included calendar aging effects—an aging factor not considered in the original models. Once again, the methods using aging-aware control outperformed the aging-unaware control, and aging control using linear damage accumulation outperformed the alternative and was easier to tune to the new model. A controller designed around the higher-order model was not considered, but could be a subject of future work.

Substantial future work can follow from the results presented in this chapter. First, other forms of robustification can be considered for aging control. For instance, a strategy that jointly controls both the throughput and cycle counting damage models could be developed and may potentially improve robustness. Incorporating the severity factor approach into the cycle-counting controller

would not require any additional state variables and so is computationally feasible. Incorporating the full power-law aging dynamics, however, would "cost" an extra state variable in the DP controller, potentially causing issues with the curse of dimensionality.

The proposed strategies could also be tested against a wider array of uncertainties. This might include increased aging model variation such as other higher-fidelity aging models or variation in aging model parameters, or additional uncertainties like passenger count variation or road grade variation. Sensitivity of the controller to changes in component and energy prices should also be studied in more depth.

CHAPTER 7

New Strategies for Robust Energy Management and Aging-Aware Control

While Chapter 6 looked at the robustness of existing energy management methods, this chapter develops a novel energy management strategy that incorporates minimax decision-making into an optimal control problem to make the control robust to uncertainties, such as unknown driving conditions or modeling errors. This new method augments a stochastic dynamic programming controller with minimax dynamic programming. The stochastic element uses a Markov chain model to represent driver behavior and is used to optimize the control for expected future driver behavior. The minimax element instead optimizes against potential worst-case (maximal) future costs.

This method is first demonstrated on a series hybrid electric bus model. Robustness to uncertain driving conditions is tested by simulating on a variety of heavy-duty vehicle drive cycles that differ from the drive cycle on which the EMS was trained. A single tuning parameter is used to balance the stochastic and minimax elements of the EMS, and a parametric study shows that with proper tuning, using minimax control could increase the vehicle fuel economy on multiple uncertain driving conditions, with a trade-off of decreased fuel economy when the driving conditions match the designed conditions. That is, it offers an exchange of performance on the nominal driving conditions for performance on uncertain driving conditions.

A second application of this new method looks at aging-aware energy management of an electric bus with hybrid energy storage. Results from the SDP-ECX control developed in Chapter 5 are first used to infer how minimax augmentation can be expected to affect control of battery aging. Given that battery damage tends to occur in large peaks, the new method is concluded to act as a tuning knob to trade an increase in battery lifespan for a decrease in fuel economy. Simulation is then used to test the minimax augmentation considering both the cycle-counting and power-law aging

models, and it is shown that the inclusion of minimax control improved the overall economic benefit of the HESS by reducing battery aging to a greater degree than it increased energy consumption.

7.1. Introduction

One of the main issues in the development of hybrid electric vehicles is how to efficiently control the power flow from the engine and battery to meet the driver's torque demand. The energy management system provides the supervisory control that governs how this torque demand is met and seeks to provide the requested power in the most efficient manner possible.

Energy management strategies are typically designed around specific driving conditions. This gives high efficiency when actual driving conditions match the designed conditions, but performance can suffer if actual conditions vary from the nominal. Reference [**153**] shows this phenomenon while analyzing the robustness of SDP to changing driving conditions. However, it does not explicitly design its controller to be robust to these changes. Several methods exist in the literature to counter the effects of this uncertainty. One field of study is in drive cycle recognition: by using past driving information and comparing it to the statistical properties of known drive cycles, different control strategies can be scheduled to match the varying driving conditions [**154**, **155**, **156**]. Alternately, on-line learning methods can be used to adapt the EMS to changing conditions. For instance, reference [**37**] proposes a model predictive controller that continuously updates a Markov chain model to reflect current driving conditions, while reference [**157**] implements a neural network to adapt the energy management to changing driving conditions. A further option is the adaptive forms of the Equivalent Consumption Minimization Strategy (ECMS), which seeks to update the equivalence factor used in ECMS based on current driving conditions, and has been studied in a wide range of papers including [**158**, **159**, **160**, **161**, **162**].

This chapter proposes a new method where, instead of adapting to uncertain driving conditions, the EMS can instead be made robust to these and other uncertainties, so that performance is maintained without needing to alter the control policy. This proposed method uses minimax dynamic programming (MDP) to robustify the EMS to driving condition uncertainty. As illustrated in Figure 7.1, robust control lets one balance performance under nominal operating conditions with performance when the system is subjected to uncertainty. Minimax decision-making, per [**163**], performs optimization with regards to all possible evolutions of the disturbance and obtains

robustness by minimizing the impact of the worst-case (maximal cost) potential outcome of a scenario. In other contexts, MDP has been referred to Minimax Model Predictive Control (MPC) [**163**], and in fact bears resemblance to the Stackelberg game from game theory [**164**].

The downside of this approach is that the worst-case scenario, in the context of vehicle control, tends to not happen often. So, an MDP-based controller tends to be overly conservative. This is demonstrated in references [**32**, **36**], which develop a game-theory based EMS that utilizes the minimax principle as part of a back-and-forth competition between the EMS and the driver (the EMS tries to minimize a cost function, assuming the driver is trying to maximize it). To mitigate the conservativeness of the minimax approach, the authors of [**32**,**36**] included a weighting function that makes likely-to-happen driving conditions have a high cost. This chapter proposes a different approach to mitigate the conservativeness of MDP while still garnering its robustness: a control policy that augments stochastic dynamic programming with MDP to form an implementable control policy that is robust to uncertainties, such as modeling errors and off-cycle driving conditions.

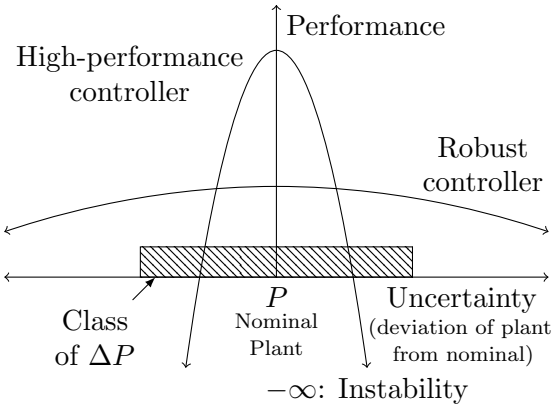

FIGURE 7.1. Robustness and performance for a generic dynamic system. Robust control offers a compromise between nominal performance and performance in face of uncertainty.

First, this chapter introduces a new control concept of blending SDP and MDP. Next, this control concept is applied to the energy management of a series-hybrid electric bus as a case study. Simulation results are presented showing how uncertain driving conditions impact vehicle efficiency. Following this, the method is applied to energy management of a electric bus with HESS for aging-aware control. Simulation results are again presented and discussed.

7.2. Minimax-Augmented Stochastic Dynamic Programming

Chapter 3 presented the DDP, SDP, and MDP approaches to dynamic programming that have been used so far in this work. This section proposes a new method of DP-based control that incorporates the optimality of SDP with the robustness of MDP

Recall that the dynamic programming problem considers a discrete-time dynamic system

$$x(k+1) = f(x(k), u(k), w(k)) \tag{7.1}$$

where $x(k)$ is the state vector at time k, $u(k)$ is the control vector, and $w(k)$ is a vector of any exogenous variables, such as commanded inputs or disturbances. x, u, and w are assumed to exist in finite ranges $x \in X$, $u \in U$, and $w \in W$. Recall also that SDP control minimizes *expected* future costs according to

$$J = \mathbf{E}\left[\sum_{k=0}^{N} \gamma^k L(x(k), u(k), w(k))\right] \tag{7.2}$$

while MDP control minimizes the *maximum possible* future costs.

$$J = \max_{w \in W}\left\{\sum_{k=0}^{N} \gamma^k L(x(k), u(k), w(k))\right\} \tag{7.3}$$

This chapter proposes a new method of DP control, named "Minimax-Augmented Stochastic Dynamic Programming" (MASDP). This method blends the SDP controller with MDP in order to capture both the performance of SDP with the robustness of MDP. The MASDP cost function is defined as

$$J = p \cdot \mathbf{E}\left[\sum_{k=0}^{N} \gamma^k L(x(k), u(k), w(k))\right] + q \cdot \max_{w \in W}\left\{\sum_{k=0}^{N} \gamma^k L(x(k), u(k), w(k))\right\} \tag{7.4}$$

where q, $0 < q < 1$, and $p = 1 - q$ are a tuning parameters to balance the importance of expected cost and maximal cost in J. Then, per (3.12)–(3.13) and (3.23)–(3.24), the cost-to-go function for

MASDP can be written as

$$V(x,w,N) = \min_{u\in U}\{L(x,u,w)\} \tag{7.5}$$

$$V(x,w,k) = \min_{u\in U}\Bigg\{L(x,u,w) + \gamma\cdot\Big(p\cdot\mathbf{E}\left[V(f(x,u,w),w,k+1)\right] + q\cdot\max_{w(k+1)\in W}\left\{V(f(x,u,w),w(k+1),1)\right\}\Big)\Bigg\} \tag{7.6}$$

$$\text{for } k = N-1,\ \ldots,\ 0$$

$V(x,w,k)$ is evaluated for each $x \in X$ and $w \in W$, while the optimal control is found by a direct search of $u \in U$.

Like SDP and MDP, the MASDP problem can be treated as either a finite or infinite horizon problem. The optimal control u^* is given by

$$u^*(x,w) = \arg\min_{u\in U}\Bigg\{L(x,u,w) + \gamma\cdot\Big(p\cdot\mathbf{E}\left[V(f(x,u,w),w,k+1)\right] + q\cdot\max_{w(k+1)\in W}\left\{V(f(x,u,w),w(k+1),1)\right\}\Big)\Bigg\} \tag{7.7}$$

the control that optimizes the final update of the cost-to-go function. The resulting control policy is both time-invariant and causal.

7.3. Case Study: Hybrid-Electric Bus with Uncertain Driving Conditions

The first application of the MASDP method is to a series hybrid bus subjected to drive cycle variations. The bus model is described first, followed by control. Next, the experimental design is developed and the simulation results are presented and discussed.

7.3.1. Modeling. This study uses a model for a series hybrid electric bus (SHEB) based on the dynamics developed in Chapter 2. Parameter values for the vehicle model can be found in Table 7.1. The bus is assumed to be fully loaded and at its maximum allowable weight. Vehicle parameters are estimated from existing literature on bus simulation [**70**, **71**, **72**]. The SHEB model uses a 200kW generator and 180kW diesel engine, sized based on [**74**] with a 6:1 fixed gear ratio between them.

TABLE 7.1. Vehicle model physical parameters.

Parameter	**Variable**	**Value**
Vehicle Mass	M_v	18,181 kg
Frontal Area	A_f	8.02 m^2
Drag Coefficient	C_D	0.55
Roll Resistance Coefficient	C_R	0.008
Wheel Inertia	J_w	20.52 kg-m^2
Motor Inertia	J_m	0.277 kg-m^2
Wheel Radius	R_w	0.48 m
Final Drive Ratio	N_{fd}	5.1:1
Gearbox Ratio	N_{gb}	5:1
Transmission Efficiency	η_{trans}	96%

This study uses the simple Rint battery model with the same cell parameters as the study in Chapter 4, sourced from [**121**]. The parameters for the battery model can be found in Table 7.2. The nonlinear SOC curve is simplified to the affine relationship

$$V_{ocv,cell} = a_0 \cdot SOC + a_1 \tag{7.8}$$

where a_0 and a_1 are fitted to the linear region of the OCV vs. SOC curve, shown in Figure 7.2. The number of cells in series was chosen so that the OCV would be in line with the recommendations in [**77**]. The number of cells in parallel was chosen so that the bus can meet the maximum power demand of a suburban bus route [**128**] and in line with the power requirements in [**74**, **77**].

TABLE 7.2. Battery model parameters.

Parameter	Variable	Value
OCV Slope	a_0	0.10v
OCV Intercept	a_1	3.17v
Equivalent Resistance	R_{cell}	6 mΩ
Battery Cells in Parallel	N_{par}	8 cells
Parallel Sets in Series	N_{ser}	80 sets
Total Charge Capacity	Q_{batt}	20Ah

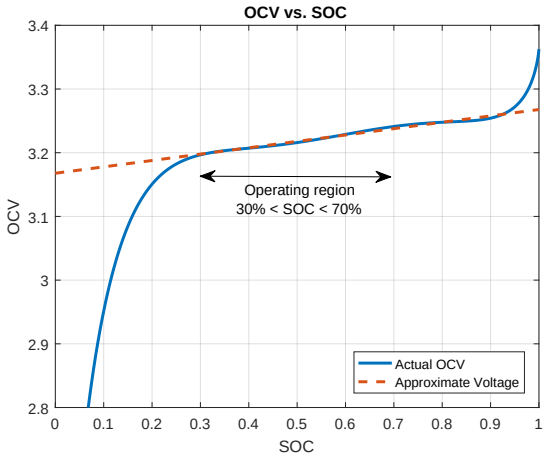

FIGURE 7.2. Battery OCV and SOC relationship.

7.3.1.1. *Comparison to Real-World Vehicles.* The bus model used in this study is built in-line with existing models in the literature and uses data for components also in the literature or on real buses. To validate the overall model, the performance of the bus can be compared to real-world hybrid bus performance. Reference [**165**], for instance, finds real-world series hybrid buses operating on bus drive cycles to have fuel economy ranging from approximately 2.6 MPG to 6.9 MPG. Similarly, reference [**166**] shows hybrid bus fuel economy in the range of 7.2 MPG to 8.8 MPG and reference [**167**] gives a range of 4.2 MPG to 8.0 MPG. This chapter's model, meanwhile, has fuel economy ranging from 3.9 MPG to 8.3 MPG, depending on the precise drive cycle and controller type. The model's performance falls squarely in the range of of existing literature on hybrid buses, so we conclude that this model is valid for use in simulation and control development.

7.3.2. Control Development.

7.3.2.1. *Dynamic Programming.* DDP, SDP, and MASDP are applied in this case study. This subsection describes the cost functions and constraints used to implemented the DP control policies.

Per [**37**], the instantaneous cost function should account for three terms:

(1) SOC regulation
(2) Optimal operation of the engine and generator
(3) Power smoothing for rider comfort

To accomplish the first objective, a quadratic cost

$$cost_{SOC} = Q_1(SOC - SOC_{tgt})^2 \tag{7.9}$$

is used to penalize deviation of the SOC from the target value of $SOC_{tgt} = 0.5$. This penalty enforces a charge-sustaining policy. Additionally, SOC is constrained so that

$$0.3 \leq SOC \leq 0.7. \tag{7.10}$$

For this model, $Q_1 = 3.4 \times 10^6$

For the second objective, a quadratic cost

$$cost_{Pgen} = Q_2(P_{gen} - P_{tgt})^2 \tag{7.11}$$

is used to penalize deviation of the generator power from a target value P_{tgt}. When the engine is on, the target value for P_{gen} is the peak efficiency point P^*_{gen}. However, the engine must also be able to shut down when it is not needed. So, a threshold P_{th} is defined so that the target value for P_{gen} is zero when below the threshold. In other words,

$$P_{tgt} = \begin{cases} P^*_{gen} & P_{gen}(k) > P_{th} \\ 0 & P_{gen}(k) \leq P_{th}. \end{cases} \tag{7.12}$$

Then, (7.11) can be written as

$$cost_{Pgen} = \begin{cases} Q_2(P_{gen} - P^*_{gen})^2 & P_{gen}(k) > P_{th} \\ Q_2(P_{gen})^2 & P_{gen}(k) \leq P_{th}. \end{cases} \tag{7.13}$$

Additionally, a shutdown threshold P_{sd} is defined so that when $P_{gen}(k) < P_{sd}$, the engine is considered off; no fuel is consumed and no power is generated. So, $P_{gen}(k) < P_{sd}$ indicates that the engine is fully off, $P_{sd} < P_{gen}(k) < P_{th}$ indicates that the engine is in the process of starting up or shutting down, and $P_{gen}(k) > P_{th}$ indicates the engine is fully on. For this model, $Q_2 = 6 \times 10^{-5}$, $P_{th} = 25$kW and $P_{sd} = 5$kW were implemented. Finally, the generator power is constrained to

$$0 \leq P_{gen} \leq 180kW. \tag{7.14}$$

Power smoothing is accomplished by rate-limiting the generator power, by penalizing large rates of change of generator power, and by limiting the generator state transitions. Specifically, a quadratic cost

$$cost_{rate} = R_1(P_{gen}(k) - P_{gen}(k-1))^2 \tag{7.15}$$

and a rate limit of

$$-5kW \leq P_{gen}(k) - P_{gen}(k-1) \leq 5kW \tag{7.16}$$

are applied to discourage large changes in the generator power. This limit is based off the limit imposed on [**37**]. For this model, $R_1 = 10^{-8}$ was implemented. State transitions are limited as shown in Figure 7.3. When off, the engine can stay off or begin turning on. When turning on, the engine must continue turning on until it is fully on ($P_{gen} > P_{th}$). When on, the engine may stay on or begin turning off. When turning off, the engine must continue turning off until it is fully off ($Pgen = 0$).

The weights Q_1, Q_2, and R_1 were tuned by hand. The weights from [**37**] were used as a starting point, adjusted for the difference in vehicle scale, and then tuned by trial-and-error to maximize the SDP efficiency. These same weights were then used for DDP and MASDP without additional tuning.

Equations (7.9), (7.13), and (7.15) give an instantaneous cost function

$$L(x, u, w) = cost_{SOC} + cost_{Pgen} + cost_{rate}. \tag{7.17}$$

$\gamma = 0.95$ is selected for the cost function J in (7.4), in line with work in [**98**, **99**]. Additionally, the controllers for this study use an infinite horizon. Discussion of the selection for p and q are

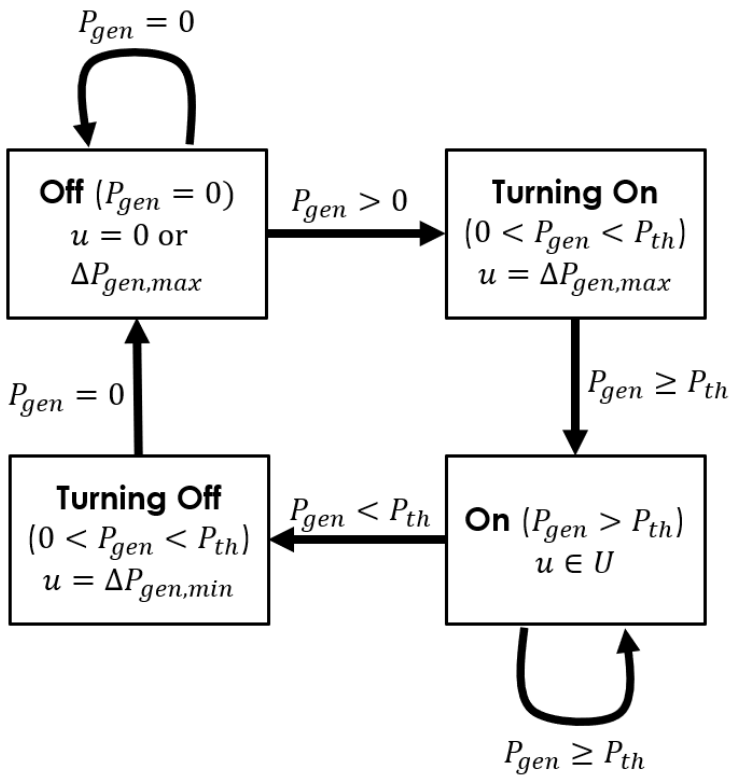

FIGURE 7.3. Engine/generator state transitions.

found in the next subsection. Under this formulation, the controlled variable $P_{gen}(k)$ is a function of $SOC(k)$, $P_{gen}(k-1)$ (to apply the power smoothing), $P_{req}(k)$, and $\omega_{wh}(k)$.

A time step of $\Delta t = 1$ second is used for the DP problem. From the rated motor power of 250kW and the vehicle dynamics given in Chapter 2, the minimum and maximum angular acceleration are found to be $\alpha_{max} = -\alpha_{min} = 15.3\ rad/s^2$, which act as constraints on reachable ω_{wh} for minimax control.

7.3.2.2. *Equivalent Consumption Minimization Strategy.* This study considers an additional controller type, unrelated to dynamic programming: an on-line application of the Equivalent Consumption Minimization Strategy (ECMS). The concept of ECMS is to assign a cost (or reward) to the consumption (or storage) of electrical energy, so that the use of electrical energy can be made equivalent to the use of fuel [**39**]. Then, fuel consumption can be optimized instantaneously at each time step. This study follows the method developed in [**40**] using an equivalence factor tuned for each drive cycle, and uses this ECMS result as a benchmark for the other controllers. Other forms of ECMS, such as ECMS utilizing Pontryagin's Minimization Principle to obtain a global

optimum [**6**] or the adaptive ECMS discussed in [**41**], are not considered at this time but are a subject for future consideration.

7.3.3. Simulation Design. The developed model is now used for a case-study analysis of MASDP control: Simulation is used to determine how the MASDP controllers perform relative to an SDP controllers. This case study only looks at the SHEB and only considers uncertainty coming from driving conditions.

In order to test the robustness of controllers to uncertain driving conditions, MASDP controllers are designed on the Orange County Transit Authority (OCTA) suburban bus drive cycle and then simulated on the following six drive cycles [**140**]:

(1) OCTA bus cycle
(2) Heavy-Duty Urban Diesel Dynamometer Schedule (HD-UDDS)
(3) City Suburban Heavy Vehicle Route (CSHVR)
(4) Manhattan Bus Cycle (MBC)
(5) West Virginia University City Cycle (WVUC)
(6) West Virginia Univeristy Suburban Cycle (WVUS)

The first case represents driving in known operating conditions—the vehicle is driven on the same cycle that was used to form the stochastic model. However, the remaining five drive cycles are driving in uncertain conditions, in the sense that the EMS is using a stochastic model that does not match the actual driving conditions. In all cases, a backwards-facing simulation is used.

MASDP controllers were designed for a range of values $0.03 \leq q \leq 0.12$. Additionally, an SDP,controller designed in the OCTA cycle and DDP and ECMS controllers designed on each of the six drive cycles were simulated to provide a benchmark for the performance of the MASDP controllers.

The vehicle is a standard (not plug-in) hybrid, so it operates entirely in charge-sustaining mode, starting at 50% SOC and maintaining an SOC target of 50% throughout the simulation. All simulations begin with the generator turned off. For each simulation, the fuel economy in miles per gallon (MPG) was calculated by obtaining the fuel power P_{fuel} from the generator power P_{gen} per (2.19) using the OEC shown in Figure 2.5. Then, P_{fuel} is integrated to obtain the total energy consumed, which is then converted gallons of fuel using the energy and volumetric densities of diesel

fuel. An additional amount of fuel is consumed whenever the engine is turned on. MPG is used rather than MPG-equivalent (MPGe) as all energy consumption comes from the stored fuel.

The SHEB is driven on each drive cycle for four hours of driving. Fuel economy is measured at each simulation's end. At the end of the simulation the difference between the initial and final state of charge is transformed to an equivalent amount of fuel that is added or subtracted from the actual fuel consumption, as in [**37**]. In essence, if the SOC finishes below 50%, then the amount of fuel needed to return to 50% is calculated and added to the total fuel consumption; if the final SOC is greater than 50%, then the excess fuel spent is subtracted from the total fuel consumption. With that said, the energy stored in or lost from the battery is small with regards to the total energy consumption, given the length of the simulation timespan.

7.3.4. Simulation Results. Figure 7.4 shows the SOC of the SHEB for each of the six drive cycles for the DDP, SDP, and MASDP (for $q = 0.08$) controllers. These plots are truncated to the first drive cycle of several consecutive drive cycles, so that the method differences can clearly be seen. For each drive cycle and controller type, the SOC stays close to the target of 50%. The SDP and MASDP controllers yield roughly similar SOC trajectories, while the DDP solution is more distinct.

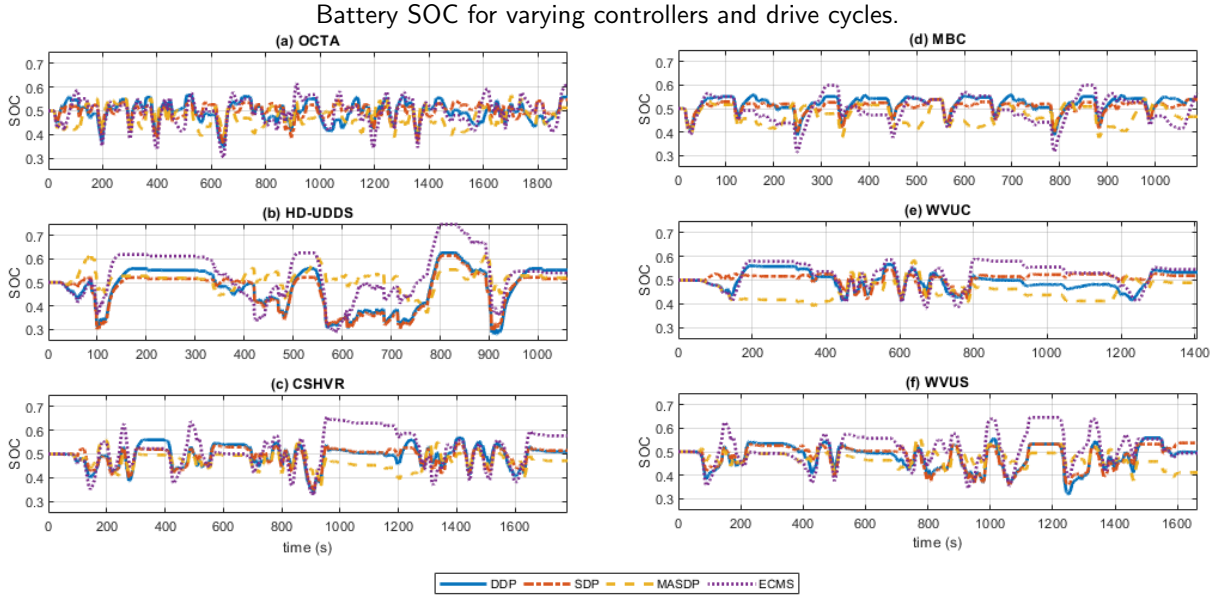

FIGURE 7.4. SOC of DDP, SDP, and MASDP ($q = 0.08$) controllers on each drive cycle.

Figure 7.5 shows the fuel economy of the SDP and each MASDP controller as a function of the tuning parameter q for each drive cycle. To better visualize the impact of minimax augmentation, Figure 7.6 shows the percent increase or decrease in fuel economy with respect to the SDP control on each drive cycle. Note that $q = 0$ corresponds to the SDP controller. Because MASDP is a modified version of the SDP and because DDP is noncausal and therefore not implementable, it is more useful to compare the MASDP results to the SDP results, rather than DDP results. Fuel economies from each of the simulations and controller types are summarized in Table 7.3. The MASDP results in Table 7.3 are for $q = 0.08$, which per Figure 7.6 generally saw the largest increase in performance for uncertain driving conditions. The far-right column on Table 7.3 shows the percent change in fuel economy of the MASDP ($q = 0.08$) controller compared to the SDP controller.

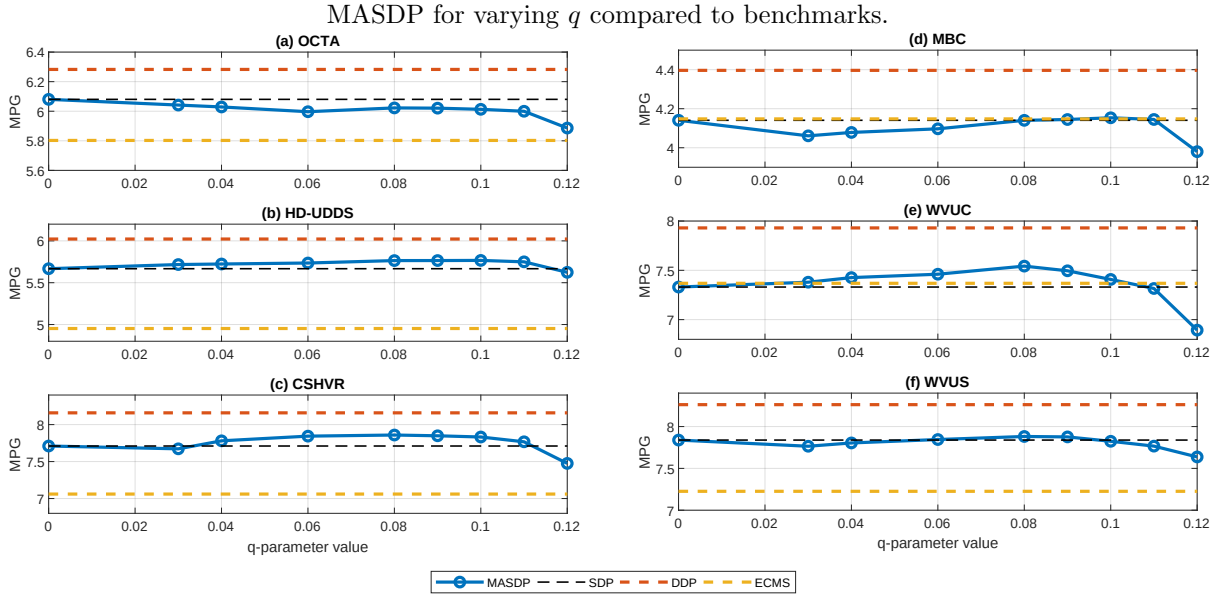

FIGURE 7.5. MPG of MASDP controllers on each drive cycle, with SDP ($q = 0$), DDP, and ECMS for reference).

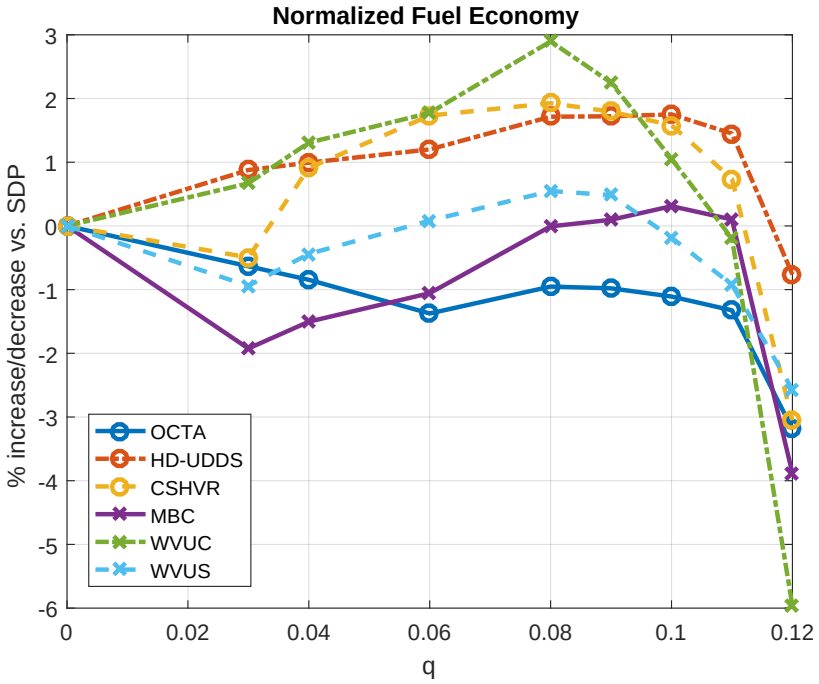

FIGURE 7.6. Percent increase or decrease in fuel economy of MASDP controllers with regards to SDP on each drive cycle.

TABLE 7.3. Fuel Economy by Controller and Drive Cycle (in miles per gallon) at $q = 0.08$.

Drive Cycle	**DDP**	**SDP**	**MASDP**	**ECMS**	**MASDP wrt SDP**
OCTA	6.28	6.08	6.02	5.80	−1.0%
HD-UDDS	6.02	5.67	5.76	4.95	+1.7%
CSHVR	8.16	7.71	7.86	7.06	+1.9%
MBC	4.40	4.14	4.14	4.14	0.0%
WVUC	7.93	7.33	7.54	7.37	+2.9%
WVUS	8.26	7.84	7.88	7.22	+0.5%

For the nominal drive cycle (OCTA), the unaugmented SDP controller outperforms the MASDP outright. However, this is not unexpected. Referring back to Figure 7.1, robust control provides a trade-off between performance at nominal operating conditions and performance in uncertain operating conditions. A drop in performance on the nominal drive cycle was expected—the important

question is whether or not performance in uncertain conditions increase enough to make the robust control worthwhile.

Although the performance on the nominal drive cycle declines slightly, each of the remaining drive cycles experiences increased fuel economy for at least some values of $q > 0$. In the case of the HD-UDDS, CSHVR, and WVUC cycles, the improvement well exceeds the loss in nominal performance. On the other hand the MBC and WVUS cycles actually see a decrease in performance for low values of q. However, the MASDP improves the MBC fuel economy for $0.08 \leq q \leq 0.11$ and improves the WVUS fuel economy for $0.05 \leq q \leq 0.1$.

In particular $q = 0.08$ offers the best improvement when considering all six drive cycles. However, after $q = 0.1$ the overall performance of the MASDP controller begins to drop, and after $q = 0.12$ the MASDP controller is uniformly worse than conventional SDP. This indicates that the control has become too robust and too conservative. Referring back to Figure 7.1, one could consider the class of driving condition uncertainties to fall entirely under the "high-performance" controller: very high q provides robustness to a degree of uncertainty that the bus does not experience, resulting in an inefficient controller.

Both the SDP and MASDP appear capable of getting close to the DDP results. Not unexpectedly, the SDP fuel economy comes closest to the DDP result for the OCTA simulation, where it is 3.3% less than DDP. On uncertain driving conditions, the SDP fuel economy is instead between 5.4% and 8.2% less than the DDP results.

7.4. Case Study: Aging-Aware Energy Management

This next section explores applying the MASDP method to aging-aware energy management. Considering the same electric bus with hybrid energy storage used in previous chapters, we first explore the characteristics of an SDP controller and infer how the addition of minimax control might impact the energy management behavior. Next, several MASDP-based controllers are developed and simulated to confirm the inferred expectations. Simulation results and the impact of minimax control on HESS energy management are then discussed.

7.4.1. Justification for Minimax Augmentation. This study begins by looking more in depth at the SDP-ECX results from Chapter 5 for the $N_{pc} = 100$ case—that is, an electric bus

with hybrid energy storage simulated using the SDP-ECX energy management strategy from Section 5.3 designed and simulated on the Manhattan Bus Cycle following the procedure established in Section 5.4.

Recall the ECX cost function, a weighted combination of three terms.

$$L(x, u, w) = Cost_{batt}\Delta D + Cost_{elec}E_{loss} + Cost_{UC}\Delta SoA \tag{7.18}$$

How might the minimax augmentation affect the response? In other words, how will MASDP control balance these three cost terms differently? The "goal" of the minimax approach is to minimize maximum values—peaks—in the instantaneous cost. If a particular cost function term is prone to large peak values, it can be expected that the minimax augmentation will work towards that term and those peak values over other terms. Standard deviation and the coefficient of variation (that is, relative covariance) are used to assess how the different terms of Equation (7.18) contribute to the overall cost. For an arbitrary variable a with mean μ_a and standard deviation σ_a, the coefficient of variation is defined as

$$c_{\mathrm{v},a} = \frac{\sigma_a}{\mu_a} \tag{7.19}$$

If a term has high standard deviation and coefficient of covariance, the term contributes to total cost in spurts; periods of little cost followed by peaks of large cost. If standard deviation and coefficient of covariance is low, then the term contributes to the total cost steadily with minimal peaks.

The components of Equation (7.18) are separated into three separate parts.

$$c_{batt}(t) = Cost_{batt}\Delta D(t) \tag{7.20}$$

$$c_{elec}(t) = Cost_{elec}E_{loss}(t) \tag{7.21}$$

$$c_{uc}(t) = Cost_{UC}\Delta SoA(t) \tag{7.22}$$

Each of these terms is evaluated from simulation results, and their statistical measures at the battery's beginning of life are obtained and given in Table 7.4. Based on these measures, it appears that the battery cost term experiences the type of peaking that minimax augmentation would work against: the standard deviation is nearly twice the mean, and the relative covariance exceeds that

of other terms. This makes some intuitive sense: battery degradation grows exponentially with discharge depth and current, and it is not surprising that these exponential relationships can lead to large peaks in cost. Figure 7.7 confirms this behavior, plotting a window of the time-history of c_{batt} as measured from simulation.

TABLE 7.4. Statistical measures of cost terms from SDP-ECX simulation results on MBC.

Variable	μ $(\times 10^{-6})$	σ $(\times 10^{-6})$	c_v	max $(\times 10^{-6})$
c_{batt}	261.5	512.8	1.96	5308.3
c_{elec}	31.2	0.48	0.015	38.9
c_{uc}	22.7	32.4	1.42	223.9

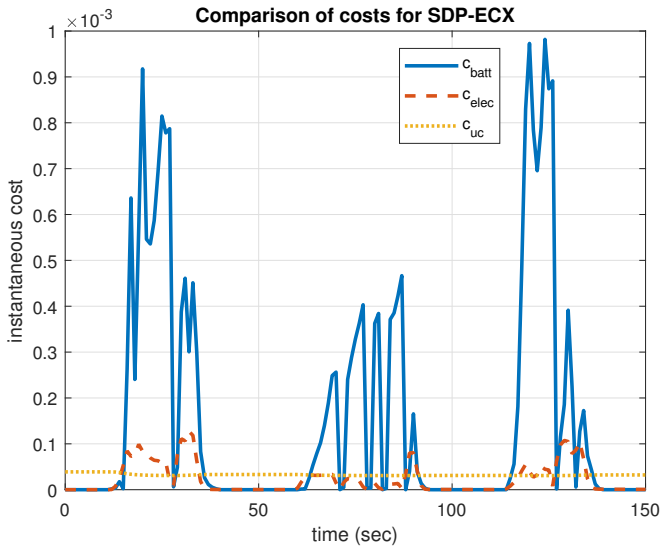

FIGURE 7.7. Comparison of components of instantaneous cost in SDP-ECX control.

So, it is expected that minimax augmentation will work to reduce the cost of battery damage at the expense of increasing the other cost terms. MASDP's q-parameter, then, would act as a "tuning knob" on the fuel consumption/battery aging trade-off curve.

Recall that the control-oriented HESS models used developed the SDP control strategy are simplified versions of the full models used for simulation; discrepancies between these simplified models and the full models can be sources of error that diminish control performance. For instance, the

control-oriented model uses a quasistatic battery model and 1st-order ultracapacitor model, while the simulation model uses a 2nd-order battery and 4th-order ultracapacitor to better approximate real energy storage components. As discussed in Section 2.3.1, the battery damage over a single time-step is only approximated; the true aging over the drive cycle cannot be known until the discharge cycle is complete.

Alternatively, the DP optimization process relies on discretization of the controller variables into grids of points, and the cost-to-go update function relies on interpolating from within this grid. Battery dynamics, battery aging, and ultracapacitor aging all are highly nonlinear processes, so interpolation will introduce measurable error into the DP optimization routine.

To wit, the nature of SDP control development, especially for aging-aware energy management, unavoidably includes model uncertainties. MASDP serves as an approach to robustify control against uncertainties, and analysis of the SDP results indicate that MASDP control would further increase battery lifespan versus SDP. Collectively, this points to MASDP control being an approach that should be applied to optimizing energy management.

7.4.2. MASDP for Aging-Aware Energy Management. Using the same vehicle model as the original SDP-ECX controller from Chapter 5, twelve total MASDP-ECX energy management strategies are developed, with q-parameter ranging from 0.01 to 0.12 in intervals of 0.01 and designed on the Manhattan Bus Cycle. Each controller is applied to the test vehicle and simulated on the Manhattan Bus Cycle following the procedure established in Section 5.4.

First, it is verified that the MASDP control follows the expectations laid out in the previous subsection. Figure 7.8(a) shows that increasing the amount of minimax control decreases the mean cost of battery damage, while Figure 7.8(b) and (c) shows in increase to the mean UC aging cost and mean energy cost the trade-off for increased battery lifespan. Each mean value is seen to converge as q is increased, indicating a limit to the affects of minimax augmentation. Notably, the drop in battery aging costs is greater than the increase in energy and UC aging costs for any given q value. the Figure 7.9 compares the time-history c_{batt} term for the SDP control and MASDP control at $q = 0.1$. Here, it can be seen that the MASDP control lowers the peak battery damage values as expected.

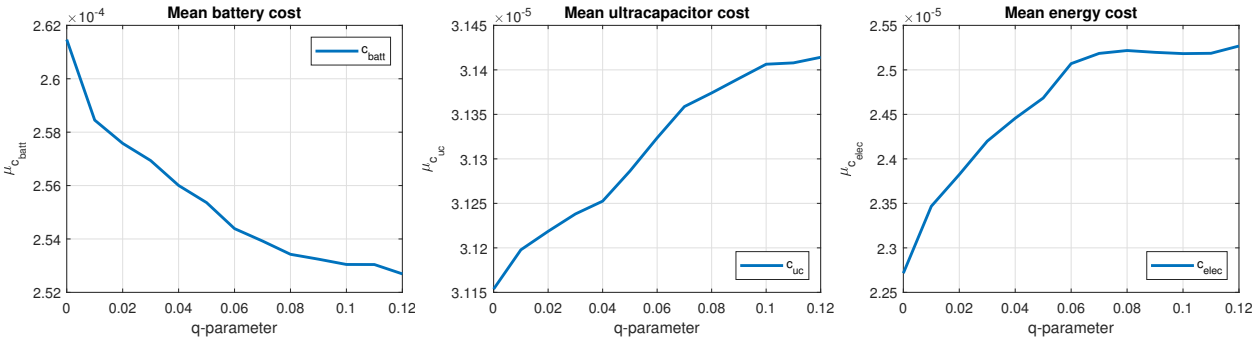

(a) (b) (c)

FIGURE 7.8. Effect of q-parameter tuning on (a) battery aging costs, (b) UC aging costs, and (c) energy costs for the ECX strategy using SDP and MASDP.

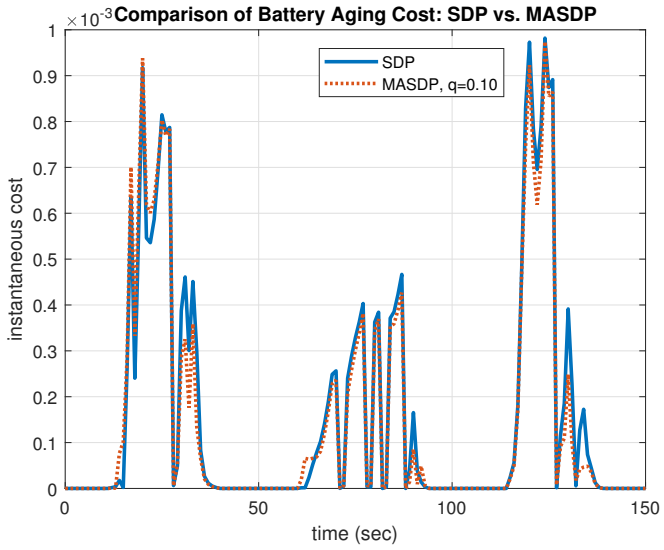

FIGURE 7.9. Comparison of battery instantaneous cost, SDP vs. MASDP.

Next, Figure 7.10 compares the resulting battery lifespan and economic benefit between the DDP, SDP, and MASDP results. The results of Figure 7.8 are reflected in Figure 7.10: In Figure 7.10(a), we see the battery lifespan grow while fuel economy decreases as the degree of minimax control is increased, correlating with the decrease in battery damage and increase in energy losses seen earlier. Likewise, Figure 7.10(b) shows the economic benefit increasing with q, corresponding to how Figure 7.8 showed the decrease in battery aging costs to exceed the increase in energy and UC aging costs. Additionally, the lifespan and economic benefits are both seen to converge as q is increased. Overall, MASDP's lifespan increase over the nominal battery lifespan is up to 9.8%

greater than that of SDP. MASDP also offers a 9.2% increase in economic benefit relative to the SDP controller.

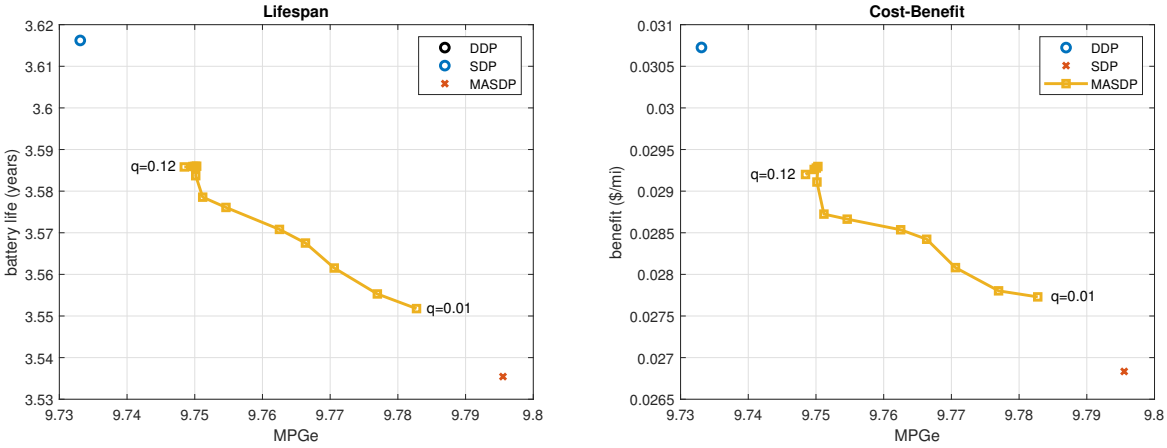

(a) (b)

FIGURE 7.10. Comparison of energy consumption with (a) battery lifespan and (b) economic benefit for DDP, SDP, and MASDP controllers.

Finally, the above experiments are repeated using the power law aging model rather than the cycle counting aging model—it is important to verify that the improvements from MASDP apply to all models of battery aging and are not a product of a specific modeling choice. DDP-ECX, SDP-ECX, and MASDP-ECX controllers are developed using the power law aging model. MASDP is designed for $q = 0.04$ to $q = 0.16$ at 0.04 intervals. Each controller is applied to the test vehicle, which now uses the power law aging model as well, and is simulated on the Manhattan Bus Cycle following the procedure established in Section 5.4.

Figure 7.11 shows the resulting lifespan and economic benefit from minimax augmentation. On the power-law aging model, MASDP's lifespan increase over the nominal battery lifespan is up to 10.2% greater than that of SDP. MASDP also offers a 7.0% increase in economic benefit relative to the SDP controller. In line with what was seen in cycle-counting, the benefit of MASDP increases with q up until approximately $q = 0.12$ before leveling off.

Overall, these results show that the newly developed MASDP method is a strong choice for aging-aware energy management. MASDP offers clear improvements to battery lifespan and economic benefit over SDP regardless of the type of aging model being considered.

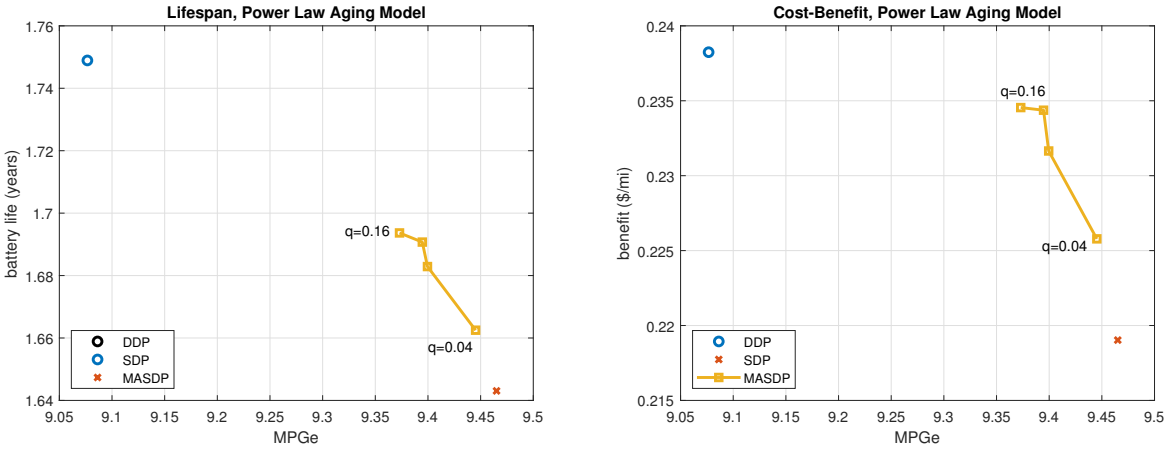

(a) (b)

FIGURE 7.11. Comparison of energy consumption with (a) battery lifespan and (b) economic benefit for DDP, SDP, and MASDP controllers using power law aging model.

7.5. Conclusion

This chapter proposes a new control concept for hybrid vehicle energy management. The proposes control strategy augments SDP with MDP was proposed in order leverage the robustness to uncertainty that comes from the minimax principle. The goal of the proposed approachs is to improve the robustness of SDP with regards to driving condition uncertainty. This controller could be used in place of or perhaps alongside drive-cycle identification algorithms, which are used to schedule different controllers to changing driving conditions.

Two applications of MASDP control were demonstrated. First, the MASDP controller was applied to a SHEB and simulated on six different heavy-duty drive cycles, one upon which the MASDP controller was trained and five that can be considered "uncertain" driving conditions. The MASDP tuning parameter q was varied from 0.03 to 0.12 in order to observe the impact of different degrees of minimax control. Simulation results showed that although performance on nominal operating conditions suffered compared to SDP, fuel economy on uncertain driving conditions improved by up to 3%.

The second application applied MASDP control to aging-aware energy management of an electric bus with hybrid energy storage. The results of an SDP controller were investigated, and from them it was inferred that minimax augmentation could act as a tuning knob to trade a increase in

battery lifespan for a decrease in fuel economy. Simulation results confirmed this inference, and it was shown on both the cycle-counting aging model and power-law aging model that the inclusion of minimax control improved the overall economic benefit of the HESS.

Although this research was carried out on single vehicle topologies (an SHEV for the first application and an EV with HESS for the second application), it is expected that it could perform similarly well on other vehicle types as well as for non-heavy duty vehicles like passenger cars. The limiting factor on how well this controller performs is how often its vehicle faces uncertain operating conditions or the degree of modeling error in the control development, which can occur for any vehicle type. Future research will apply the MASDP approach to these other APV topologies and will compare this method to other methods of handling uncertain driving conditions, such as adaptive ECMS and various forms of drive cycle identification. Other forms of uncertainty, such as variable passenger loads along a bus route—should be investigated. Additionally, the benefits of MASDP control on battery lifespan should be investigated for other APV topologies and should be considered jointly with forms of uncertainty.

CHAPTER 8

Conclusions

8.1. General Remarks

The aim of this project was to analyze the relationship between fuel economy and battery aging in HD-APVs, especially buses, and to propose new ways to the reduce trade-off between the two. A review of existing and ongoing work by other researchers identified gaps in the literature regarding on-board photovoltaics, optimal control of hybrid energy storage, and the robustness of aging-aware energy management. This research applied a systems-level approach, focusing on how the powertrain subsystems interact and what new subsystems can be added and controlled decrease battery lifespan while maintaining or increasing energy efficiency. Four studies were carried out with the aim of improving this trade-off.

The first study was to investigate supplementing an electric bus's battery with on-board photovoltaic modules. OBPV was considered to be particularly well-suited to EVs operating with large batteries for long hours, as PV power could the battery's charge throughput but not affect dynamic aging factors like large currents. An on-board photovoltaics model was created to analyze their impact on electric bus range and battery lifespan. Photovoltaic systems that cover the bus roof and bus sides were considered as the bus model was simulated on a suburban bus drive cycle on a bus route in Davis, CA, for a representative sample of yearly weather conditions.

For the particular application studied, roof-mounted panels were shown to increase vehicle driving range by 4.7% on average annually, while roof and side modules together increased driving range by 8.9%. However, variations in weather conditions meant that this additional range was not reliably available. For constant vehicle range, rooftop photovoltaic modules extended battery cycle life by up to 10% while modules on both the roof and sides extended battery cycle life by up to 19% by reducing the discharge depth of the battery. Additionally, the OBPV proved to be more cost effective than the control cases, increasing battery size. Although side-mounted

photovoltaics increased cycle life and range, they were less weight- and cost-effective compared to the roof-mounted panels.

For electric vehicles with smaller batteries or for hybrid vehicles operating in a charge depletion mode, large current spikes from acceleration and braking can be a major cause of battery wear. The second study looked at hybrid energy storage—pairing a lithium battery with an ultracapacitor—to reduce these spikes and improve battery aging. Existing literature had developed a plethora of methods to utilize the HESS for aging control, however these existing methods had not considered the impact of ultracapacitor aging. A new energy management strategy that jointly optimized for battery aging, UC aging, and energy losses was developed and tested for an array of HESS sizings.

Simulation results showed that the newly proposed energy management strategy offered the best improvement to the aging-energy consumption trade-off across all considered HESS sizes. At the largest UC size, this strategy offered a 16.4% increase to battery lifespan and required only a 2.8% decrease in MPGe. The existing method that controlled battery aging and energy losses but not ultracapacitor aging was highly effective at increasing battery lifespan but achieved these results at the expense of significant ultracapacitor aging, resulting in a worse overall cost-benefit. Without UC aging control and at small UC sizes, the UC could even age faster than the battery. UC aging control did not require any new state variables to implement and ensured the UC aged at a slow rate, roughly 13% to 15% of the rate of the battery, depending on UC size.

The prior two studies had used a cycle-counting method for measuring battery aging, and the aging-aware control introduced in Chapter 5 specifically used a form of cycle-counting adapted for control. However these studies as well as most other studies in the literature take for granted the accuracy of the controller's aging model, despite a wide variety of aging models available. The third study in this dissertation looked at the robustness of the aging-aware energy management to variations in the battery aging mechanism. Aging-aware controllers were designed using the strategy from the prior study and using two different aging models, a cycle-counting model and a power-law model. These controllers were then simulated on cases where the simulated aging model matched the model used in control and where the simulated aging model differed.

Simulation results first showed the method proposed in Chapter 5 performed well for both aging models when the controller model match the "true" model. However when testing for robustness, simulation results showed that an energy management system designed with the "incorrect" aging

model had degraded performance: controllers designed with the "wrong" aging model resulted in minimal benefit to the HESS, with controllers designed with the power-law aging model faring worse. A simple aging-rate adjustment was proposed for the controller design: multiplying the "cost" of battery damage by the ratio of measured aging to modeled aging. This correction factor improved the performance in the face of uncertainty for the two controllers using linear damage accumulation, such that they was nearly on par with energy management not facing uncertainty. On the other hand, the simple adjustment failed to improve the performance of the controller using the full power-law dynamics when subject to aging model uncertainty.

Continuing in the theme of robust control, the fourth study introduced a new energy management concept that incorporates elements of minimax dynamic programming to a stochastic dynamic programming strategy. An SDP controller optimizes for expected costs while the minimax element instead optimizes against potential worst-case (maximal) future costs. By augmenting SDP with MDP, the energy management can be made robust to uncertainties and modeling errors. This method is first demonstrated on a series hybrid electric bus model. Robustness to uncertain driving conditions is tested by simulating on a variety of heavy-duty vehicle drive cycles that differ from the drive cycle on which the EMS was trained. It was found that using minimax control could increase the vehicle fuel economy on multiple uncertain driving conditions by up to 3%, with a trade-off of decreased fuel economy when the driving conditions match the designed conditions.

The second application applied MASDP control to aging-aware energy management of an electric bus with hybrid energy storage. Based on results of the aging-aware SDP control developed in Chapter 5, it was inferred that minimax augmentation could act as a tuning knob to trade a increase in battery lifespan for a decrease in fuel economy. Simulation was then used test the minimax augmentation considering both the cycle-counting and power-law aging models, and it was shown that the inclusion of minimax control improved the overall economic benefit of the HESS by reducing battery aging to a greater degree than it increased energy consumption.

8.2. Future Work

The main objectives set out for this project have been accomplished: this work promotes a refined understanding of the trade-offs between fuel consumption and battery aging and demonstrates several approaches to ensure battery lifespan can be extended in the most economical way possible. However, there are several avenues of research that warrant further investigation.

All studies in this work rely on simulation to investigate vehicle performance and battery aging. The foremost need for future research is experimental validation of the results presented here from simulation.

In the case of on-board photovoltaics, results are only provided for a transit bus operating in Davis, CA. However, a framework has been provided to assess the viability of OBPV for any particular vehicle or location. Future work can apply this framework to develop general rules for what applications benefit from OBPV. Additionally, while existing literature has shown the fuel economy benefits of OBPV for hybrid-electric vehicles, their impact on HEV battery lifespan must still be investigated.

Regarding optimal aging-aware control of a HESS, future work for should consider optimization of the ultracapacitor sizing, given the proposed new methods of energy management. It was shown that a smaller HESS was more prone to ultracapacitor aging, meaning existing work on optimal UC sizing may need to be reevaluated when considering UC aging. Other energy management strategies should be considered and compared to the methods here, such as DDP formed into a rule base, model predictive control, or on-line applications of the Equivalent Consumption Minimization Strategy. Additionally, the approach of including UC aging control in the energy management strategy should be extended to HEV energy management for cases where an HEV makes use of a HESS.

The study on aging model robustness showed that battery aging control developed with the power law aging method was not robust to aging model variations. Future work should considered ways to improve the robustness of this method, including to other forms of uncertainty like variations on the model parameters. Other forms of robustification could be considered for aging control, such as a strategy that jointly controls both the throughput and cycle counting damage models could be developed, although this might create issues with the curse of dimensionality. The proposed strategies could be tested against a wider array of uncertainties. This might include

increased model aging variation such as a higher-fidelity aging model or variation in aging model parameters. Sensitivity of the controller to changes in component and energy prices (that is, the weights used to optimize the control) should also be studied in more depth.

Although the effect of minimax augmented control was only studied for single vehicle topologies (an SHEV for the first application and an EV with HESS for the second application), it is expected that it could perform similarly well on other powertrain topologies as well as for non-heavy duty vehicles like passenger cars. The limiting factor on how well this controller performs is how often its vehicle faces uncertain operating conditions or the degree of modeling error in the control development, which can occur for any vehicle size or type. Future research will apply the MASDP approach to these other APV topologies and will compare this method to other methods of handling uncertain driving conditions, such as adaptive ECMS and various forms of drive cycle identification. Robustification against other forms of uncertainty, such as variable passenger loads along a bus route, should be investigated as well. Finally, the benefits of MASDP control on battery lifespan should be investigated for other APV topologies and should be considered jointly with forms of uncertainty.

Bibliography

[1] A. A. Abdel-Rahman, "On the emissions from internal-combustion engines: a review," *Int. J. Energy Res.*, vol. 22, no. 6, pp. 483–513, May 1998. [Online]. Available: http://onlinelibrary.wiley.com/doi/10.1002/(SICI)1099-114X(199805)22:6⟨483::AID-ER377⟩3.0.CO;2-Z/abstract

[2] U. S. E. P. Agency, "EPA and DOT Finalize Greenhouse Gas and Fuel Efficiency Standards for Heavy-Duty Trucks," United States Environmental Protection Agency, Tech. Rep., Aug. 2016, publication Title: US EPA Type: Speeches, Testimony and Transcripts. [Online]. Available: https://archive.epa.gov/epa/newsreleases/epa-and-dot-finalize-greenhouse-gas-and-fuel-efficiency-standards-heavy-duty-trucks-1.html

[3] T.-K. Lee and Z. Filipi, "Impact of Model-Based Lithium-Ion Battery Control Strategy on Battery Sizing and Fuel Economy in Heavy-Duty HEVs," *SAE International Journal of Commercial Vehicles*, vol. 4, no. 1, pp. 198–209, Sep. 2011. [Online]. Available: http://papers.sae.org/2011-01-2253/

[4] S. J. Moura, J. L. Stein, and H. K. Fathy, "Battery-Health Conscious Power Management in Plug-In Hybrid Electric Vehicles via Electrochemical Modeling and Stochastic Control," *IEEE Transactions on Control Systems Technology*, vol. 21, no. 3, pp. 679–694, May 2013.

[5] G. Suri and S. Onori, "A control-oriented cycle-life model for hybrid electric vehicle lithium-ion batteries," *Energy*, vol. 96, pp. 644–653, Feb. 2016. [Online]. Available: http://www.sciencedirect.com/science/article/pii/S0360544215016382

[6] L. Guzzella and A. Sciarretta, *Vehicle Propulsion Systems*, 3rd ed. Berlin, Heidelberg: Springer Berlin Heidelberg, 2013. [Online]. Available: http://link.springer.com/10.1007/978-3-642-35913-2

[7] California Air Resource Board, "Technology Assessment: Heavy Duty-Hybrid Vehicles," California Air Resource Board, Tech. Rep., 2015. [Online]. Available: https://www.arb.ca.gov/msprog/tech/techreport/hybrid_tech_report.pdf

[8] ——, "Technology Assessment: Medium- and Heavy-Duty Electric Trucks and Buses," California Air Resource Board, Tech. Rep., 2015. [Online]. Available: https://www.arb.ca.gov/msprog/tech/techreport/bev_tech_report.pdf

[9] V. Ramadesigan, P. W. C. Northrop, S. De, S. Santhanagopalan, R. D. Braatz, and V. R. Subramanian, "Modeling and Simulation of Lithium-Ion Batteries from a Systems Engineering Perspective," *J. Electrochem. Soc.*, vol. 159, no. 3, pp. R31–R45, Jan. 2012. [Online]. Available: http://jes.ecsdl.org/content/159/3/R31

[10] S. Pelletier, O. Jabali, G. Laporte, and M. Veneroni, "Battery degradation and behaviour for electric vehicles: Review and numerical analyses of several models," *Transportation Research Part B: Methodological*, 2017. [Online]. Available: http://www.sciencedirect.com/science/article/pii/S0191261516303794

[11] M. Safari, M. Morcrette, A. Teyssot, and C. Delacourt, "Life-Prediction Methods for Lithium-Ion Batteries Derived from a Fatigue Approach I. Introduction: Capacity-Loss Prediction Based on Damage Accumulation," *J. Electrochem. Soc.*, vol. 157, no. 6, pp. A713–A720, Jun. 2010. [Online]. Available: http://jes.ecsdl.org/content/157/6/A713

[12] M. Yue, S. Jemei, R. Gouriveau, and N. Zerhouni, "Review on health-conscious energy management strategies for fuel cell hybrid electric vehicles: Degradation models and strategies," *International Journal of Hydrogen Energy*, vol. 44, no. 13, pp. 6844–6861, Mar. 2019. [Online]. Available: http://www.sciencedirect.com/science/article/pii/S0360319919303490

[13] J. C. Forman, S. Bashash, J. L. Stein, and H. K. Fathy, "Reduction of an Electrochemistry-Based Li-Ion Battery Model via Quasi-Linearization and Padé Approximation," *Journal of The Electrochemical Society*, vol. 158, no. 2, p. A93, 2011. [Online]. Available: https://iopscience.iop.org/article/10.1149/1.3519059

[14] M. Cheng, L. Feng, and B. Chen, "Nonlinear Model Predictive Control of a Power-Split Hybrid Electric Vehicle with Electrochemical Battery Model," in *Nonlinear Model Predictive Control of a Power-Split Hybrid Electric Vehicle with Electrochemical Battery Model*, Mar. 2017, pp. 2017–01–1252. [Online]. Available: https://www.sae.org/content/2017-01-1252/

[15] M. Petit, E. Prada, and V. Sauvant-Moynot, "Development of an empirical aging model for Li-ion batteries and application to assess the impact of Vehicle-to-Grid strategies on battery lifetime," *Applied Energy*, vol. 172, pp. 398–407, Jun. 2016. [Online]. Available: http://www.sciencedirect.com/science/article/pii/S0306261916304500

[16] J. D. K. Bishop, C. J. Axon, D. Bonilla, M. Tran, D. Banister, and M. D. McCulloch, "Evaluating the impact of V2G services on the degradation of batteries in PHEV and EV," *Applied Energy*, vol. 111, pp. 206–218, Nov. 2013. [Online]. Available: http://www.sciencedirect.com/science/article/pii/S0306261913004121

[17] A. Cordoba-Arenas, S. Onori, and G. Rizzoni, "A control-oriented lithium-ion battery pack model for plug-in hybrid electric vehicle cycle-life studies and system design with consideration of health management," *Journal of Power Sources*, vol. 279, pp. 791–808, Apr. 2015. [Online]. Available: http://www.sciencedirect.com/science/article/pii/S037877531402076X

[18] S. Onori, P. Spagnol, V. Marano, Y. Guezennec, and G. Rizzoni, "A new life estimation method for lithium-ion batteries in plug-in hybrid electric vehicles applications," *International Journal of Power Electronics*, vol. 4, no. 3, pp. 302–319, Jan. 2012. [Online]. Available: http://www.inderscienceonline.com/doi/abs/10.1504/IJPELEC.2012.046609

[19] A. Millner, "Modeling Lithium Ion battery degradation in electric vehicles," in *2010 IEEE Conference on Innovative Technologies for an Efficient and Reliable Electricity Supply*, Sep. 2010, pp. 349–356.

[20] C. Guenther, B. Schott, W. Hennings, P. Waldowski, and M. A. Danzer, "Model-based investigation of electric vehicle battery aging by means of vehicle-to-grid scenario simulations," *Journal of Power Sources*, vol. 239, pp. 604–610, Oct. 2013. [Online]. Available: http://www.sciencedirect.com/science/article/pii/S0378775313003066

[21] J. Wang, P. Liu, J. Hicks-Garner, E. Sherman, S. Soukiazian, M. Verbrugge, H. Tataria, J. Musser, and P. Finamore, "Cycle-life model for graphite-LiFePO4 cells," *J. of Power Sources*, vol. 196, no. 8, pp. 3942–3948, Apr. 2011. [Online]. Available: http://www.sciencedirect.com/science/article/pii/S0378775310021269

[22] R. Spotnitz, "Simulation of capacity fade in lithium-ion batteries," *Journal of Power Sources*, vol. 113, no. 1, pp. 72–80, Jan. 2003. [Online]. Available: http://www.sciencedirect.com/science/article/pii/S0378775302004901

[23] E. Sarasketa-Zabala, E. Martinez-Laserna, M. Berecibar, I. Gandiaga, L. M. Rodriguez-Martinez, and I. Villarreal, "Realistic lifetime prediction approach for Li-ion batteries," *Applied Energy*, vol. 162, pp. 839–852, Jan. 2016. [Online]. Available: http://www.sciencedirect.com/science/article/pii/S0306261915013513

[24] N. Omar, M. A. Monem, Y. Firouz, J. Salminen, J. Smekens, O. Hegazy, H. Gaulous, G. Mulder, P. Van den Bossche, T. Coosemans, and J. Van Mierlo, "Lithium iron phosphate based battery – Assessment of the aging parameters and development of cycle life model," *Applied Energy*, vol. 113, pp. 1575–1585, Jan. 2014. [Online]. Available: http://www.sciencedirect.com/science/article/pii/S0306261913007393

[25] X. Jin and C. Liu, "Physics-based control-oriented reduced-order degradation model for linimncoo2-graphite cell," *Electrochimica Acta*, vol. 312, pp. 188–201, 2019.

[26] M. Schimpe, M. E. v. Kuepach, M. Naumann, H. C. Hesse, K. Smith, and A. Jossen, "Comprehensive Modeling of Temperature-Dependent Degradation Mechanisms in Lithium Iron Phosphate Batteries," *Journal of The Electrochemical Society*, vol. 165, no. 2, p. A181, Jan. 2018, publisher: IOP Publishing. [Online]. Available: https://iopscience.iop.org/article/10.1149/2.1181714jes/meta

[27] N. DiOrio, A. Dobos, S. Janzou, A. Nelson, and B. Lundstrom, "Technoeconomic Modeling of Battery Energy Storage in SAM," National Renewable Energy Laboratory (NREL) NREL/TP-6A20–64641, Tech. Rep., Sep. 2015.

[28] V. Marano, S. Onori, Y. Guezennec, G. Rizzoni, and N. Madella, "Lithium-ion batteries life estimation for plug-in hybrid electric vehicles," in *2009 IEEE Vehicle Power and Propulsion Conference*, Sep. 2009, pp. 536–543.

[29] B. d. Jager, T. v. Keulen, and J. Kessels, *Optimal Control of Hybrid Vehicles*, ser. Advances in Industrial Control. Springer London, 2013. [Online]. Available: http://link.springer.com/chapter/10.1007/978-1-4471-5076-3_1

[30] S. F. Tie and C. W. Tan, "A review of energy sources and energy management system in electric vehicles," *Renewable and Sustainable Energy Reviews*, vol. 20, pp. 82–102, Apr. 2013. [Online]. Available: http://www.sciencedirect.com/science/article/pii/S1364032112006910

[31] M. F. M. Sabri, K. A. Danapalasingam, and M. F. Rahmat, "A review on hybrid electric vehicles architecture and energy management strategies," *Renewable and Sustainable Energy Reviews*, vol. 53, pp. 1433–1442, Jan. 2016. [Online]. Available: http://www.sciencedirect.com/science/article/pii/S1364032115010060

[32] C. Dextreit and I. V. Kolmanovsky, "Game Theory Controller for Hybrid Electric Vehicles," *IEEE Transactions on Control Systems Technology*, vol. 22, no. 2, pp. 652–663, Mar. 2014.

[33] S. S. Williamson, *Energy Management Strategies for Electric and Plug-in Hybrid Electric Vehicles*. Springer New York, 2013. [Online]. Available: http://link.springer.com/chapter/10.1007/978-1-4614-7711-2_1

[34] L. Johannesson, M. Asbogard, and B. Egardt, "Assessing the Potential of Predictive Control for Hybrid Vehicle Powertrains Using Stochastic Dynamic Programming," *IEEE Transactions on Intelligent Transportation Systems*, vol. 8, no. 1, pp. 71–83, Mar. 2007.

[35] I. Kolmanovsky, I. Siverguina, and B. Lygoe, "Optimization of powertrain operating policy for feasibility assessment and calibration: stochastic dynamic programming approach," in *Proceedings of the 2002 American Control Conference (IEEE Cat. No.CH37301)*, vol. 2, May 2002, pp. 1425–1430 vol.2.

[36] C. Dextreit, F. Assadian, I. V. Kolmanovsky, J. Mahtani, and K. Burnham, "Hybrid Electric Vehicle Energy Management Using Game Theory," in *SAE Technical Paper*. SAE International, Apr. 2008. [Online]. Available: http://papers.sae.org/2008-01-1317/

[37] S. D. Cairano, D. Bernardini, A. Bemporad, and I. V. Kolmanovsky, "Stochastic MPC With Learning for Driver-Predictive Vehicle Control and its Application to HEV Energy Management," *IEEE Transactions on Control Systems Technology*, vol. 22, no. 3, pp. 1018–1031, May 2014.

[38] H. Borhan, A. Vahidi, A. M. Phillips, M. L. Kuang, I. V. Kolmanovsky, and S. D. Cairano, "MPC-Based Energy Management of a Power-Split Hybrid Electric Vehicle," *IEEE Transactions on Control Systems Technology*, vol. 20, no. 3, pp. 593–603, May 2012.

[39] S. Onori, L. Serrao, and G. Rizzoni, *Hybrid Electric Vehicles Energy Management Strategies*. London, UK: Springer London, 2016. [Online]. Available: https://link.springer.com/book/10.1007/978-1-4471-6781-5

[40] G. Paganelli, T.-M. Guerra, S. Delprat, J.-J. Santin, M. Delhom, and E. Combes, "Simulation and assessment of power control strategies for a parallel hybrid car," *Proceedings of the Institution of Mechanical Engineers, Part D: Journal of Automobile Engineering*, vol. 214, no. 7, pp. 705–717, 2000.

[41] S. Onori, L. Serrao, and G. Rizzoni, "Adaptive Equivalent Consumption Minimization Strategy for Hybrid Electric Vehicles," in *ASME 2010 Dynamic Systems and Control Conference*. American Society of Mechanical Engineers Digital Collection, Jan. 2011, pp. 499–505. [Online]. Available: https://asmedigitalcollection.asme.org/DSCC/proceedings/DSCC2010/44175/499/345421

[42] P. Keil and A. Jossen, "Charging protocols for lithium-ion batteries and their impact on cycle life—An experimental study with different 18650 high-power cells," *Journal of Energy Storage*, vol. 6, pp. 125–141, May 2016. [Online]. Available: http://www.sciencedirect.com/science/article/pii/S2352152X16300147

[43] A. Cordoba-Arenas, S. Onori, Y. Guezennec, and G. Rizzoni, "Capacity and power fade cycle-life model for plug-in hybrid electric vehicle lithium-ion battery cells containing blended spinel and layered-oxide positive electrodes," *Journal of Power Sources*, vol. 278, pp. 473–483, Mar. 2015. [Online]. Available: http://www.sciencedirect.com/science/article/pii/S0378775314020758

[44] M. Geca, M. Wendeker, and L. Grabowski, "A City Bus Electrification Supported by the Photovoltaic Power Modules," in *SAE Technical Paper*. Birmingham, United Kingdom: SAE International, Oct. 2014. [Online]. Available: http://papers.sae.org/2014-01-2898/

[45] K. Kimura, Y. Kudo, and A. Sato, "Techno-Economic Analysis of Solar Hybrid Vehicles Part 1: Analysis of Solar Hybrid Vehicle Potential Considering Well-to-Wheel GHG Emissions," in *SAE Technical Paper*. SAE International, Apr. 2016. [Online]. Available: http://papers.sae.org/2016-01-1287/

[46] T. Hara, T. Shiga, K. Kimura, and A. Sato, "Techno-Economic Analysis of Solar Hybrid Vehicles Part 2: Comparative Analysis of Economic, Environmental, and Usability Benefits," in *SAE Technical Paper*. SAE International, Apr. 2016. [Online]. Available: http://papers.sae.org/2016-01-1286/

[47] M. Abdelhamid, "A Comprehensive Assessment Methodology Based on Life Cylce Analysis for On-Board Photovoltaic Solar Modeules in Vehicles," Ph.D. Dissertation, Clemson University, South Carolina, Dec. 2014. [Online]. Available: http://tigerprints.clemson.edu/all_dissertations/1458

[48] M. Giannouli and P. Yianoulis, "Study on the incorporation of photovoltaic systems as an auxiliary power source for hybrid and electric vehicles," *Solar Energy*, vol. 86, no. 1, pp. 441–451, Jan. 2012. [Online]. Available: http://www.sciencedirect.com/science/article/pii/S0038092X11003860

[49] G. Rizzo, "Automotive Applications of Solar Energy," *IFAC Proceedings Volumes*, vol. 43, no. 7, pp. 174–185, Jul. 2010. [Online]. Available: http://www.sciencedirect.com/science/article/pii/S1474667015368257

[50] G. Almonacid, F. J. Muñoz, J. de la Casa, and J. D. Aguilar, "Integration of PV systems on health emergency vehicles. The FIVE project," *Prog. Photovolt: Res. Appl.*, vol. 12, no. 8, pp. 609–621, Dec. 2004. [Online]. Available: http://onlinelibrary.wiley.com/doi/10.1002/pip.558/abstract

[51] A. S. Bahaj and P. A. B. James, "Economics of solar powered refrigeration transport applications," in *Conference Record of the Twenty-Ninth IEEE Photovoltaic Specialists Conference, 2002.* New Orleans, LA: IEEE, May 2002, pp. 1561–1564.

[52] L. Kronthaler, L. Maturi, D. Moser, and L. Alberti, "Vehicle-integrated Photovoltaic (ViPV) systems: Energy production, Diesel Equivalent, Payback Time; an assessment screening for trucks and busses," in *2014 Ninth International Conference on Ecological Vehicles and Renewable Energies (EVER)*, Mar. 2014, pp. 1–8.

[53] T. Kovaltchouk, B. Multon, H. B. Ahmed, J. Aubry, and P. Venet, "Enhanced Aging Model for Supercapacitors Taking Into Account Power Cycling: Application to the Sizing of an Energy Storage System in a Direct Wave Energy Converter," *IEEE Transactions on Industry Applications*, vol. 51, no. 3, pp. 2405–2414, May 2015.

[54] T. Kovaltchouk, H. B. Ahmed, B. Multon, J. Aubry, and P. Venet, "An aging-aware life cycle cost comparison between supercapacitors and Li-ion batteries to smooth Direct Wave Energy Converter production," in *2015 IEEE Eindhoven PowerTech*, Jun. 2015, pp. 1–6.

[55] A. Hammar, P. Venet, R. Lallemand, G. Coquery, and G. Rojat, "Study of Accelerated Aging of Supercapacitors for Transport Applications," *IEEE Transactions on Industrial Electronics*, vol. 57, no. 12, pp. 3972–3979, Dec. 2010.

[56] J. M. Miller and G. Sartorelli, "Battery and ultracapacitor combinations #x2014; Where should the converter go?" in *2010 IEEE Vehicle Power and Propulsion Conference*, Sep. 2010, pp. 1–7.

[57] J. J. Awerbuch and C. R. Sullivan, "Control of Ultracapacitor-Battery Hybrid Power Source for Vehicular Applications," in *2008 IEEE Energy 2030 Conference*, Nov. 2008, pp. 1–7.

[58] Z. Song, J. Li, X. Han, L. Xu, L. Lu, M. Ouyang, and H. Hofmann, "Multi-objective optimization of a semi-active battery/supercapacitor energy storage system for electric vehicles," *Applied Energy*, vol. 135, pp. 212–224, Dec. 2014. [Online]. Available: http://www.sciencedirect.com/science/article/pii/S0306261914008964

[59] J. Shen, S. Dusmez, and A. Khaligh, "Optimization of Sizing and Battery Cycle Life in Battery/Ultracapacitor Hybrid Energy Storage Systems for Electric Vehicle Applications," *IEEE Transactions on Industrial Informatics*, vol. 10, no. 4, pp. 2112–2121, Nov. 2014.

[60] F. Akar, Y. Tavlasoglu, and B. Vural, "An Energy Management Strategy for a Concept Battery/Ultracapacitor Electric Vehicle With Improved Battery Life," *IEEE Transactions on Transportation Electrification*, vol. 3, no. 1, pp. 191–200, Mar. 2017.

[61] R. Carter, A. Cruden, and P. J. Hall, "Optimizing for Efficiency or Battery Life in a Battery/Supercapacitor Electric Vehicle," *IEEE Transactions on Vehicular Technology*, vol. 61, no. 4, pp. 1526–1533, May 2012.

[62] C. Zhao, H. Yin, and C. Ma, "Quantitative Evaluation of LiFePO Battery Cycle Life Improvement Using Ultracapacitors," *IEEE Transactions on Power Electronics*, vol. 31, no. 6, pp. 3989–3993, Jun. 2016.

[63] Z. Song, J. Li, J. Hou, H. Hofmann, M. Ouyang, and J. Du, "The battery-supercapacitor hybrid energy storage system in electric vehicle applications: A case study," *Energy*, vol. 154, pp. 433–441, Jul. 2018. [Online]. Available: https://www.sciencedirect.com/science/article/pii/S0360544218307643

[64] B. Xu, J. Shi, S. Li, H. Li, and Z. Wang, "Energy consumption and battery aging minimization using a q-learning strategy for a battery/ultracapacitor electric vehicle," *Energy*, vol. 229, p. 120705, 2021.

[65] J. Du, X. Zhang, T. Wang, Z. Song, X. Yang, H. Wang, M. Ouyang, and X. Wu, "Battery degradation minimization oriented energy management strategy for plug-in hybrid electric bus with multi-energy storage system," *Energy*, vol. 165, pp. 153–163, Dec. 2018. [Online]. Available: https://www.sciencedirect.com/science/article/pii/S0360544218318486

[66] J. Hou and Z. Song, "A hierarchical energy management strategy for hybrid energy storage via vehicle-to-cloud connectivity," *Applied Energy*, vol. 257, p. 113900, Jan. 2020. [Online]. Available: https://www.sciencedirect.com/science/article/pii/S0306261919315879

[67] S. Zhang, X. Hu, S. Xie, Z. Song, L. Hu, and C. Hou, "Adaptively coordinated optimization of battery aging and energy management in plug-in hybrid electric buses," *Applied Energy*, vol. 256, p. 113891, Dec. 2019. [Online]. Available: http://www.sciencedirect.com/science/article/pii/S0306261919315788

[68] H. H. Eldeeb, A. T. Elsayed, C. R. Lashway, and O. Mohammed, "Hybrid Energy Storage Sizing and Power Splitting Optimization for Plug-In Electric Vehicles," *IEEE Transactions on Industry Applications*, vol. 55, no. 3, pp. 2252–2262, May 2019, conference Name: IEEE Transactions on Industry Applications.

[69] G. Mohan, F. Assadian, and S. Longo, "Comparative analysis of forward-facing models vs backwardfacing models in powertrain component sizing," in *IET Hybrid and Electric Vehicles Conference 2013 (HEVC 2013)*, Nov. 2013, pp. 1–6.

[70] X. Zeng, N. Yang, J. Wang, D. Song, N. Zhang, M. Shang, and J. Liu, "Predictive-model-based dynamic coordination control strategy for power-split hybrid electric bus," *Mechanical Systems and Signal Processing*, vol. 60–61, pp. 785–798, Aug. 2015. [Online]. Available: http://www.sciencedirect.com/science/article/pii/S0888327014005056

[71] F. Sangtarash, V. Esfahanian, H. Nehzati, S. Haddadi, M. A. Bavanpour, and B. Haghpanah, "Effect of Different Regenerative Braking Strategies on Braking Performance and Fuel Economy in a Hybrid Electric Bus Employing CRUISE Vehicle Simulation," *SAE International Journal of Fuels and Lubricants*, vol. 1, no. 1, pp. 828–837, Jun. 2008. [Online]. Available: http://papers.sae.org/2008-01-1561/

[72] B. H. Wang, Y. G. Luo, and J. W. Zhang, "Simulation of city bus performance based on actual urban driving cycle in China," *Int.J Automot. Technol.*, vol. 9, no. 4, pp. 501–507, Aug. 2008. [Online]. Available: https://link.springer.com/article/10.1007/s12239-008-0060-3

[73] T. Markel, A. Brooker, T. Hendricks, V. Johnson, K. Kelly, B. Kramer, M. O'Keefe, S. Sprik, and K. Wipke, "ADVISOR: a systems analysis tool for advanced vehicle modeling," *Journal of Power Sources*, vol. 110, no. 2, pp. 255–266, Aug. 2002. [Online]. Available: http://www.sciencedirect.com/science/article/pii/S0378775302001891

[74] Fauvel, Clement, Vikesh Napal, and Aymeric Rousseau, "Medium and heavy duty hybrid electric vehicle sizing to maximize fuel consumption displacement on real world drive cycles," in *EVS26 International Battery, Hybrid and Fuel Cell Electric Vehicle Symposium.* Los Angeles , California: Power (W), May 2012, pp. 0–22. [Online]. Available: https://www.autonomie.net/docs/5%20-%20Presentations/Heavy%20duty/CF%20-%20EVS26.pdf

[75] K. Ahn and P. Y. Papalambros, "Engine optimal operation lines for power-split hybrid electric vehicles," *Proceedings of the IMechE*, vol. 223, no. 9, pp. 1149–1162, Sep. 2009. [Online]. Available: http://journals.sagepub.com/doi/abs/10.1243/09544070JAUTO1124

[76] X. Lin, H. E. Perez, S. Mohan, J. B. Siegel, A. G. Stefanopoulou, Y. Ding, and M. P. Castanier, "A lumped-parameter electro-thermal model for cylindrical batteries," *Journal of Power Sources*, vol. 257, pp. 1–11, Jul. 2014. [Online]. Available: https://www.sciencedirect.com/science/article/pii/S0378775314001244

[77] R. F. Nelson, "Power requirements for batteries in hybrid electric vehicles," *J. Power Sources*, vol. 91, no. 1, pp. 2–26, Nov. 2000. [Online]. Available: http://www.sciencedirect.com/science/article/pii/S0378775300004833

[78] C. E. Laird and A. G. Alleyne, "A Hybrid Electro-Thermal Energy Storage System for High Ramp Rate Power Applications," in *DSCC2019*, Volume 2: Modeling and Control of Engine and Aftertreatment Systems; Modeling and Control of IC Engines and Aftertreatment Systems; Modeling and Validation; Motion Planning and Tracking Control; Multi-Agent and Networked Systems; Renewable and Smart Energy Systems; Thermal Energy Systems; Uncertain Systems and Robustness; Unmanned Ground and Aerial Vehicles; Vehicle

Dynamics and Stability; Vibrations: Modeling, Analysis, and Control, Oct. 2019, v002T23A001. [Online]. Available: https://doi.org/10.1115/DSCC2019-9089

[79] M. A. Zabara, C. B. Uzundal, and B. Ülgüt, "Performance modeling of unmanaged hybrid battery/supercapacitor energy storage systems," *Journal of Energy Storage*, vol. 43, p. 103185, Nov. 2021. [Online]. Available: https://www.sciencedirect.com/science/article/pii/S2352152X21008859

[80] Y. Wu, Z. Huang, H. Liao, B. Chen, X. Zhang, Y. Zhou, Y. Liu, H. Li, and J. Peng, "Adaptive power allocation using artificial potential field with compensator for hybrid energy storage systems in electric vehicles," *Applied Energy*, vol. 257, p. 113983, Jan. 2020. [Online]. Available: https://www.sciencedirect.com/science/article/pii/S0306261919316708

[81] R. Dougal, L. Gao, and S. Liu, "Ultracapacitor model with automatic order selection and capacity scaling for dynamic system simulation," *Journal of Power Sources*, vol. 126, no. 1-2, pp. 250–257, 2004.

[82] C. Zhou, K. Qian, M. Allan, and W. Zhou, "Modeling of the Cost of EV Battery Wear Due to V2g Application in Power Systems," *IEEE Trans. Energy Convers.*, vol. 26, no. 4, pp. 1041–1050, Dec. 2011.

[83] T. Endo, K. Mitsunaga, K. Takahashi, K. Kobayashi, and M. Matsuishi, "Damage evaluation of metals for random or varying loading—three aspects of rain flow method," in *Proceedings of the 1974 Symposium on Mechanical Behavior of Materials*, vol. 1. The Society of Material Science, Japan, 1974, pp. 371–380.

[84] S. D. Downing and D. Socie, "Simple rainflow counting algorithms," *International journal of fatigue*, vol. 4, no. 1, pp. 31–40, 1982.

[85] N. Hong, "A modified rainflow counting method," *International Journal of Fatigue*, vol. 13, no. 6, pp. 465–469, Nov. 1991. [Online]. Available: https://www.sciencedirect.com/science/article/pii/014211239190481D

[86] M. Musallam and C. M. Johnson, "An Efficient Implementation of the Rainflow Counting Algorithm for Life Consumption Estimation," *IEEE Transactions on Reliability*, vol. 61, no. 4, pp. 978–986, Dec. 2012, conference Name: IEEE Transactions on Reliability.

[87] J.-O. Lee and Y.-S. Kim, "Novel battery degradation cost formulation for optimal scheduling of battery energy storage systems," *International Journal of Electrical Power & Energy Systems*, vol. 137, p. 107795, May 2022. [Online]. Available: https://www.sciencedirect.com/science/article/pii/S0142061521010140

[88] Y. Shi, B. Xu, Y. Tan, and B. Zhang, "A Convex Cycle-based Degradation Model for Battery Energy Storage Planning and Operation," in *2018 Annual American Control Conference (ACC)*, Jun. 2018, pp. 4590–4596, iSSN: 2378-5861.

[89] S. Li, H. He, C. Su, and P. Zhao, "Data driven battery modeling and management method with aging phenomenon considered," *Applied Energy*, vol. 275, p. 115340, Oct. 2020. [Online]. Available: https://www.sciencedirect.com/science/article/pii/S0306261920308527

[90] B. Xu, A. Oudalov, A. Ulbig, G. Andersson, and D. S. Kirschen, "Modeling of Lithium-Ion Battery Degradation for Cell Life Assessment," *IEEE Transactions on Smart Grid*, vol. 9, no. 2, pp. 1131–1140, Mar. 2018, conference Name: IEEE Transactions on Smart Grid.

[91] ——, "Modeling of lithium-ion battery degradation for cell life assessment," *IEEE Transactions on Smart Grid*, vol. 9, no. 2, pp. 1131–1140, 2016.

[92] L. Serrao, S. Onori, A. Sciarretta, Y. Guezennec, and G. Rizzoni, "Optimal energy management of hybrid electric vehicles including battery aging," in *Proceedings of the 2011 American Control Conference*, Jun. 2011, pp. 2125–2130.

[93] L. Tang, G. Rizzoni, and S. Onori, "Optimal energy management of HEVs with consideration of battery aging," in *2014 IEEE Conference and Expo Transportation Electrification Asia-Pacific (ITEC Asia-Pacific)*, Aug. 2014, pp. 1–6.

[94] N. Omar, Y. Firouz, J. M. Timmermans, M. A. Monem, H. Gualous, T. Coosemans, P. V. d. Bossche, and J. V. Mierlo, "Lithium Iron Phosphate - Assessment of Calendar Life and Change of Battery Parameters," in *2014 IEEE Vehicle Power and Propulsion Conference (VPPC)*, Oct. 2014, pp. 1–5.

[95] P. Zhang, F. Yan, and C. Du, "A comprehensive analysis of energy management strategies for hybrid electric vehicles based on bibliometrics," *Renewable and Sustainable Energy Reviews*, vol. 48, pp. 88–104, Aug. 2015. [Online]. Available: http://www.sciencedirect.com/science/article/pii/S1364032115002464

[96] D. Bianchi, L. Rolando, L. Serrao, S. Onori, G. Rizzoni, N. Al-Khayat, T.-M. Hsieh, and P. Kang, "A rule-based strategy for a series/parallel hybrid electric vehicle: an approach based on dynamic programming," in *Dynamic Systems and Control Conference*, vol. 44175, 2010, pp. 507–514.

[97] J. Peng, H. He, and R. Xiong, "Rule based energy management strategy for a series–parallel plug-in hybrid electric bus optimized by dynamic programming," *Applied Energy*, vol. 185, pp. 1633–1643, 2017.

[98] E. D. Tate, J. W. Grizzle, and H. Peng, "Shortest path stochastic control for hybrid electric vehicles," *Int. J. Robust Nonlinear Control*, vol. 18, no. 14, pp. 1409–1429, Sep. 2008. [Online]. Available: http://onlinelibrary.wiley.com/doi/10.1002/rnc.1288/abstract

[99] C.-C. Lin, H. Peng, and J. W. Grizzle, "A stochastic control strategy for hybrid electric vehicles," in *Proceedings of the 2004 American Control Conference*, vol. 5, Jun. 2004, pp. 4710–4715 vol.5.

[100] A. M. Abdel Dayem, "Set-up and performance investigation of an innovative solar vehicle," *J. of Renewable and Sustainable Energy*, vol. 4, no. 3, pp. 033 109:1 – 033 109:18, May 2012. [Online]. Available: http://aip.scitation.org/doi/abs/10.1063/1.4717512

[101] J. Xue, "Assessment of agricultural electric vehicles based on photovoltaics in China," *J. Renew. Sustainable Energy*, vol. 5, no. 6, pp. 063 108:1 – 063 108:10, Nov. 2013. [Online]. Available: http://aip.scitation.org/doi/abs/10.1063/1.4831956

[102] M. B. Azwan, A. L. Norasikin, K. Sopian, S. Abd Rahim, K. Norman, K. Ramdhan, and D. Solah, "Assessment of electric vehicle and photovoltaic integration for oil palm mechanisation practise," *J. Cleaner Production*, vol. 140, Part 3, pp. 1365–1375, Jan. 2017. [Online]. Available: http://www.sciencedirect.com/science/article/pii/S0959652616316146

[103] O. Kanz, A. Reinders, J. May, and K. Ding, "Environmental impacts of integrated photovoltaic modules in light utility electric vehicles," *Energies*, vol. 13, no. 19, 2020. [Online]. Available: https://www.mdpi.com/1996-1073/13/19/5120

[104] C. C. Y. Ma and M. Iqbal, "Statistical comparison of solar radiation correlations Monthly average global and diffuse radiation on horizontal surfaces," *Solar Energy*, vol. 33, no. 2, pp. 143–148, Jan. 1984. [Online]. Available: http://www.sciencedirect.com/science/article/pii/0038092X84902317

[105] C. R. Tracy, K. A. Hammond, R. A. Lechleitner, W. J. Smith, D. B. Thompson, A. D. Whicker, and S. C. Williamson, "Estimating clear-day solar radiation: An evaluation of three models," *J. of Thermal Biology*, vol. 8, no. 3, pp. 247–251, Jul. 1983. [Online]. Available: http://www.sciencedirect.com/science/article/pii/0306456583900037

[106] S. Wilcox and W. Marion, "Users Manual for TMY3 Data Sets," May 2008.

[107] I. Arsie, M. Marotta, C. Pianese, G. Rizzo, and M. Sorrentino, "Optimal Design of a Hybrid Electric Car with Solar Cells," in *Proceedings of 1st AUTOCOM Workshop on Preventive and Active Safety Systems for Road Vehicles.* Istanbul, Turkey: AUTOCOM Workshop, Sep. 2005. [Online]. Available: http://www.dimec.unisa.it/leonardo_new/doc/HSV_AUTOCOM_05.pdf

[108] Proterra, "Catalyst 40-Foot Transit Vehicle." [Online]. Available: https://www.proterra.com/products/catalyst-40ft/

[109] K. Emery, "Measurement and Characterization of Solar Cells and Modules," in *Handbook of Photovoltaic Science and Engineering*, 2nd ed., A. Luque and S. Hegedus, Eds. John Wiley & Sons, Ltd, 2011, pp. 797–840, dOI: 10.1002/0470014008.ch16. [Online]. Available: http://onlinelibrary.wiley.com/doi/10.1002/0470014008.ch16/summary

[110] HighFlex Solar, Inc., "HF315-6-36b." [Online]. Available: http://www.highflexsolar.com/docs/HighFlexSolar_HF315-6-36b_Datasheet_v1.0.pdf

[111] I. Reda and A. Andreas, "Solar position algorithm for solar radiation applications," *Solar Energy*, vol. 76, no. 5, pp. 577–589, 2004. [Online]. Available: http://www.sciencedirect.com/science/article/pii/S0038092X0300450X

[112] P. G. Loutzenhiser, H. Manz, C. Felsmann, P. A. Strachan, T. Frank, and G. M. Maxwell, "Empirical validation of models to compute solar irradiance on inclined surfaces for building energy simulation," *Solar Energy*, vol. 81, no. 2, pp. 254–267, Feb. 2007. [Online]. Available: http://www.sciencedirect.com/science/article/pii/S0038092X06000879

[113] M. G. Villalva, J. R. Gazoli, and E. R. Filho, "Comprehensive Approach to Modeling and Simulation of Photovoltaic Arrays," *IEEE Trans. Power Electron.*, vol. 24, no. 5, pp. 1198–1208, May 2009.

[114] S. Shongwe and M. Hanif, "Comparative Analysis of Different Single-Diode PV Modeling Methods," *IEEE Journal of Photovoltaics*, vol. 5, no. 3, pp. 938–946, May 2015, conference Name: IEEE Journal of Photovoltaics.

[115] N. M. A. Alrahim Shannan, N. Z. Yahaya, and B. Singh, "Single-diode model and two-diode model of PV modules: A comparison," in *2013 IEEE International Conference on Control System, Computing and Engineering*, Nov. 2013, pp. 210–214.

[116] A. Jain and A. Kapoor, "Exact analytical solutions of the parameters of real solar cells using Lambert W-function," *Solar Energy Materials and Solar Cells*, vol. 81, no. 2, pp. 269–277, Feb. 2004. [Online]. Available: http://www.sciencedirect.com/science/article/pii/S0927024803002605

[117] T. Esram and P. L. Chapman, "Comparison of Photovoltaic Array Maximum Power Point Tracking Techniques," *IEEE Trans. Energy Convers.*, vol. 22, no. 2, pp. 439–449, Jun. 2007.

[118] A. Bidram, A. Davoudi, and R. S. Balog, "Control and Circuit Techniques to Mitigate Partial Shading Effects in Photovoltaic Arrays," *IEEE Journal of Photovoltaics*, vol. 2, no. 4, pp. 532–546, Oct. 2012.

[119] K. Emery, J. Burdick, Y. Caiyem, D. Dunlavy, H. Field, B. Kroposki, T. Moriarty, L. Ottoson, S. Rummel, T. Strand, and M. W. Wanlass, "Temperature dependence of photovoltaic cells, modules and systems," in *Conference Record of the Twenty Fifth IEEE Photovoltaic Specialists Conference - 1996*, May 1996, pp. 1275–1278.

[120] M. Muller, "Measuring and Modeling Nominal Operating Cell Temperature (NOCT)," Albuquerque, NM, Sep. 2010. [Online]. Available: http://energy.sandia.gov/wp-content/gallery/uploads/Muller_NREL_CellTemp.pdf

[121] Valence Technology, Inc., "Valence Module Range," publication Title: Valence Advanced Energy Storage Solutions. [Online]. Available: https://www.valence.com/wp-content/uploads/2016/11/Valence-Module-Range-113016.pdf

[122] ——, "Lithium Iron Magnesium Phosphate 26650 Power Cell," Dec. 2016, publication Title: Valence Advanced Energy Storage Solutions. [Online]. Available: https://www.valence.com/products/cells/26650-power-cells/

[123] ——, "Long Cycle Life Lithium Iron Magnesium Phosphate Battery," May 2014, publication Title: Valence Advanced Energy Storage Solutions. [Online]. Available: https://www.valence.com/why-valence/long-lifecycle/

[124] A. McCrone, U. Moslener, F. d'Estais, E. Usher, and C. Grüning, "Global Trends in Renewable Energy Investment 2016," FS-UNEP Collaborating Centre for Climate & Sustainable Energy Finance, Tech. Rep., Mar. 2016. [Online]. Available: http://fs-unep-centre.org/publications/global-trends-renewable-energy-investment-2016

[125] S. Kahn, M. J. Shiao, C. Honeyman, A. Perea, J. Jones, C. Smith, B. Gallagher, S. Moskowitz, J. Baca, S. Rumery, A. Holm, and K. O'Brien, "Solar Market Insight Report 2016 Q2," Solar Energy Industries Association, Tech. Rep., Jun. 2016. [Online]. Available: http://www.seia.org/research-resources/solar-market-insight-report-2016-q2

[126] NREL, "Dynamic Maps, GIS Data, and Analysis Tools - Solar Maps." [Online]. Available: http://www.nrel.gov/gis/solar.html

[127] M. Sengupta, Y. Xie, A. Lopez, A. Habte, G. Maclaurin, and J. Shelby, "The National Solar Radiation Data Base (NSRDB)," *Renewable and Sustainable Energy Reviews*, vol. 89, pp. 51–60, Jun. 2018. [Online]. Available: https://www.sciencedirect.com/science/article/pii/S136403211830087X

[128] California Air Resource Board, "Public Transit Bus Fleet Rule and Emission Standards for New Urban Buses," California Air Resource Board, Tech. Rep., 2002. [Online]. Available: https://www.arb.ca.gov/regact/bus02/bus02.htm

[129] City of Davis, CA, "Location and Topography." [Online]. Available: https://www.cityofdavis.org/about-davis/location-and-topography

[130] G. Papa, M. Santo Zarnik, and V. Vukašinović, "Electric-bus routes in hilly urban areas: Overview and challenges," *Renewable and Sustainable Energy Reviews*, vol. 165, p. 112555, Sep. 2022. [Online]. Available: https://www.sciencedirect.com/science/article/pii/S1364032122004543

[131] Pacific Gas & Electric Company, "Electric Rates." [Online]. Available: https://www.pge.com/tariffs/electric.shtml

[132] L. Zhang, X. Hu, Z. Wang, F. Sun, J. Deng, and D. G. Dorrell, "Multiobjective Optimal Sizing of Hybrid Energy Storage System for Electric Vehicles," *IEEE Transactions on Vehicular Technology*, vol. 67, no. 2, pp. 1027–1035, Feb. 2018, conference Name: IEEE Transactions on Vehicular Technology.

[133] Z. Song, X. Zhang, J. Li, H. Hofmann, M. Ouyang, and J. Du, "Component sizing optimization of plug-in hybrid electric vehicles with the hybrid energy storage system," *Energy*, vol. 144, pp. 393–403, Feb. 2018. [Online]. Available: https://www.sciencedirect.com/science/article/pii/S0360544217320285

[134] M. Wieczorek and M. Lewandowski, "A mathematical representation of an energy management strategy for hybrid energy storage system in electric vehicle and real time optimization using a genetic algorithm," *Applied Energy*, vol. 192, pp. 222–233, Apr. 2017. [Online]. Available: https://www.sciencedirect.com/science/article/pii/S0306261917301472

[135] Y. Wang, L. Wang, M. Li, and Z. Chen, "A review of key issues for control and management in battery and ultra-capacitor hybrid energy storage systems," *eTransportation*, vol. 4, p. 100064, 2020.

[136] P. Verma, A. K. Singh *et al.*, "Development of a nonlinear aging model for ultracapacitors," in *2019 IEEE 1st International Conference on Energy, Systems and Information Processing (ICESIP)*. IEEE, 2019, pp. 1–6.

[137] O. Bohlen, J. Kowal, and D. U. Sauer, "Ageing behaviour of electrochemical double layer capacitors: Part ii. lifetime simulation model for dynamic applications," *Journal of Power Sources*, vol. 173, no. 1, pp. 626–632, 2007.

[138] M. Teuber, M. Strautmann, J. Drillkens, and D. Sauer, "Lifetime and performance assessment of commercial electric double-layer capacitors based on cover layer formation," *ACS applied materials & interfaces*, vol. 11, no. 20, pp. 18 313–18 322, 2019.

[139] D. H. Lee, U. S. Kim, C. B. Shin, B. H. Lee, B. W. Kim, and Y.-H. Kim, "Modelling of the thermal behaviour of an ultracapacitor for a 42-v automotive electrical system," *Journal of Power Sources*, vol. 175, no. 1, pp. 664–668, 2008.

[140] T. J. Barlow, S. Latham, I. S. Mccrae, and P. G. Boulter, "A reference book of driving cycles for use in the measurement of road vehicle emissions," *TRL Published Project Report*, 2009. [Online]. Available: https://trid.trb.org/view/909274

[141] M. Hughes-Cromwick, "2019 Public Transportation Fact Book," *World Transit Research*, Jan. 2019. [Online]. Available: https://www.worldtransitresearch.info/research/7521

[142] T. Zhu, R. G. A. Wills, R. Lot, X. Kong, and X. Yan, "Optimal sizing and sensitivity analysis of a battery-supercapacitor energy storage system for electric vehicles," *Energy*, vol. 221, p. 119851, Apr. 2021. [Online]. Available: https://www.sciencedirect.com/science/article/pii/S0360544221001006

[143] US Energy Information Administration, "July 2021 monthly energy review," U.S. Energy Information Administration, Washington, DC (United States), Tech. Rep., 2021.

[144] C. Ropeter, H. Wenzl, H.-P. Beck, E. Wehrmann, J. Twidell, and D. Sauer, "The impact of microcycles on batteries in different applications," in *Proceedings of the 18th Electric Vehicle Symposium (EVS18), Berlin*, vol. 20. Citeseer, 2001.

[145] H. Min, C. Lai, Y. Yu, T. Zhu, and C. Zhang, "Comparison Study of Two Semi-Active Hybrid Energy Storage Systems for Hybrid Electric Vehicle Applications and Their Experimental Validation," *Energies*, vol. 10, no. 3, p. 279, Mar. 2017, number: 3 Publisher: Multidisciplinary Digital Publishing Institute. [Online]. Available: https://www.mdpi.com/1996-1073/10/3/279

[146] K. Mongird, V. V. Viswanathan, P. J. Balducci, M. J. E. Alam, V. Fotedar, V. S. Koritarov, and B. Hadjerioua, "Energy storage technology and cost characterization report," Pacific Northwest National Lab.(PNNL), Richland, WA (United States), Tech. Rep., 2019.

[147] K. R. Mallon, F. Assadian, and B. Fu, "Analysis of On-Board Photovoltaics for a Battery Electric Bus and Their Impact on Battery Lifespan," *Energies*, vol. 10, no. 7, p. 943, Jul. 2017, number: 7 Publisher: Multidisciplinary Digital Publishing Institute. [Online]. Available: https://www.mdpi.com/1996-1073/10/7/943

[148] A. Alyakhni, L. Boulon, J.-M. Vinassa, and O. Briat, "A comprehensive review on energy management strategies for electric vehicles considering degradation using aging models," *IEEE Access*, 2021.

[149] F. Assadian, K. R. Mallon, and B. Fu, "The Impact of Vehicle-Integrated Photovoltaics on Heavy-Duty Electric Vehicle Battery Cost and Lifespan," in *SAE Technical Paper*. SAE International, Apr. 2016. [Online]. Available: http://papers.sae.org/2016-01-1289/

[150] M. Schimpe, J. V. Barreras, B. Wu, and G. J. Offer, "Battery Degradation-Aware Current Derating: An Effective Method to Prolong Lifetime and Ease Thermal Management," *Journal of The Electrochemical Society*, vol. 168, no. 6, p. 060506, Jun. 2021, publisher: The Electrochemical Society. [Online]. Available: https://doi.org/10.1149/1945-7111/ac0553

[151] C.-H. Chung, S. Jangra, Q. Lai, and X. Lin, "Optimization of Electric Vehicle Charging for Battery Maintenance and Degradation Management," *IEEE Transactions on Transportation Electrification*, vol. 6, no. 3, pp. 958–969, Sep. 2020, conference Name: IEEE Transactions on Transportation Electrification.

[152] M. Woody, M. Arbabzadeh, G. M. Lewis, G. A. Keoleian, and A. Stefanopoulou, "Strategies to limit degradation and maximize Li-ion battery service lifetime - Critical review and guidance for stakeholders," *Journal of Energy Storage*, vol. 28, p. 101231, Apr. 2020. [Online]. Available: https://www.sciencedirect.com/science/article/pii/S2352152X19314227

[153] D. F. Opila, X. Wang, R. McGee, R. Brent Gillespie, J. A. Cook, and J. Grizzle, "Real-world robustness for hybrid vehicle optimal energy management strategies incorporating drivability metrics," *Journal of Dynamic Systems, Measurement, and Control*, vol. 136, no. 6, 2014.

[154] F. Soriano, M. Moreno-Eguilaz, and J. Álvarez Flórez, "Drive Cycle Identification and Energy Demand Estimation for Refuse-Collecting Vehicles," *IEEE Transactions on Vehicular Technology*, vol. 64, no. 11, pp. 4965–4973, Nov. 2015.

[155] R. Langari and J.-S. Won, "Integrated drive cycle analysis for fuzzy logic based energy management in hybrid vehicles," in *The 12th IEEE International Conference on Fuzzy Systems, 2003. FUZZ '03*, vol. 1, May 2003, pp. 290–295 vol.1.

[156] S.-i. Jeon, S.-t. Jo, Y.-i. Park, and J.-m. Lee, "Multi-mode driving control of a parallel hybrid electric vehicle using driving pattern recognition," *J. Dyn. Sys., Meas., Control*, vol. 124, no. 1, pp. 141–149, 2002.

[157] Y. L. Murphey, J. Park, L. Kiliaris, M. L. Kuang, M. A. Masrur, A. M. Phillips, and Q. Wang, "Intelligent Hybrid Vehicle Power Control #x2014;Part II: Online Intelligent Energy Management," *IEEE Transactions on Vehicular Technology*, vol. 62, no. 1, pp. 69–79, Jan. 2013.

[158] C. Musardo, G. Rizzoni, Y. Guezennec, and B. Staccia, "A-ecms: An adaptive algorithm for hybrid electric vehicle energy management," *European Journal of Control*, vol. 11, no. 4-5, pp. 509–524, 2005.

[159] B. Gu and G. Rizzoni, "An adaptive algorithm for hybrid electric vehicle energy management based on driving pattern recognition," in *ASME International Mechanical Engineering Congress and Exposition*, vol. 47683, 2006, pp. 249–258.

[160] A. Sciarretta, M. Back, and L. Guzzella, "Optimal control of parallel hybrid electric vehicles," *IEEE Transactions on control systems technology*, vol. 12, no. 3, pp. 352–363, 2004.

[161] H. Chen, J. Kessels, and S. Weiland, "Adaptive ecms: a causal set-theoretic method for equivalence factor estimation," *IFAC-PapersOnLine*, vol. 48, no. 15, pp. 78–85, 2015.

[162] M. Khodabakhshian, L. Feng, and J. Wikander, "Improving fuel economy and robustness of an improved ecms method," in *2013 10th IEEE International Conference on Control and Automation (ICCA)*. IEEE, 2013, pp. 598–603.

[163] P. O. Scokaert and D. Q. Mayne, "Min-max feedback model predictive control for constrained linear systems," *IEEE Transactions on Automatic control*, vol. 43, no. 8, pp. 1136–1142, 1998.

[164] P.-y. Nie, L.-h. Chen, and M. Fukushima, "Dynamic programming approach to discrete time dynamic feedback Stackelberg games with independent and dependent followers," *European Journal*

of Operational Research, vol. 169, no. 1, pp. 310–328, Feb. 2006. [Online]. Available: http://www.sciencedirect.com/science/article/pii/S0377221704004497

[165] C. Keramydas, G. Papadopoulos, L. Ntziachristos, T.-S. Lo, K.-L. Ng, H.-L. A. Wong, and C. K.-L. Wong, "Real-world measurement of hybrid buses' fuel consumption and pollutant emissions in a metropolitan urban road network," *Energies*, vol. 11, no. 10, p. 2569, 2018.

[166] J. Partridge, C. Lin, and R. Bucknall, "Fuel economy of a current hybrid london bus and fuel cell bus application evaluation," in *2016 51st International Universities Power Engineering Conference (UPEC)*. ISEC-SGIT, 2016.

[167] D. Lowell, "Comparison of modern cng, diesel and diesel hybrid-electric transit buses: Efficiency & environmental performance," *MJ Bradley & Associates, LLC. Report*, 2013.